ANALYSIS OF CLAY DEFORMATION BY RATE PROCESS THEORY

Thesis for the Degree of Ph. D.

MICHIGAN STATE UNIVERSITY

Richard W. Christensen

1964

This is to certify that the

thesis entitled

ANALYSIS OF CLAY DEFORMATION BY

RATE PROCESS THEORY

presented by

RICHARD W. CHRISTENSEN

has been accepted towards fulfillment
of the requirements for

PH. D. degree in Civil Engineering

Major professor

Date Feb. 20, 1964

O-169

ABSTRACT

ANALYSIS OF CLAY DEFORMATION BY
RATE PROCESS THEORY

by Richard W. Christensen

The deformational characteristics of clays are analyzed from the point-of-view of the particle structure, utilizing rates process theory. The deformations at the particle level are treated as the breaking and reforming of interparticle bonds as a rate process. Theoretical considerations concerning the nature of the particle structure, and the physical aspects of deformation processes are presented. A schematic model is used to represent the behavior of the particle structure under load.

Creep and relaxation data obtained from specimens prepared in the laboratory and undisturbed specimens are presented. The experimental results agree well with the behavior predicted by the model.

The variation of the model parameters in cyclic creep loading is shown to be related to particle level phenomena taking place during deformation. The calculated values of α, a rate theory parameter associated with the geometry of the flowing unit, are found to be consistent with known geometrical properties of the particle structure. The activation energy, ΔF, is calculated from the rate theory parameter β and also from temperature-creep-rate data; the two methods give nearly the same value of ΔF.

ANALYSIS OF CLAY DEFORMATION BY RATE PROCESS THEORY

By

Richard W. Christensen

A THESIS

Submitted to
Michigan State University
in partial fulfillment of the requirements
for the degree of

DOCTOR OF PHILOSOPHY

Department of Civil Engineering

1964

ACKNOWLEDGMENTS

The writer is indebted to his major professor, Dr. T. H. Wu, Professor of Civil Engineering, for his aid and encouragement throughout the writer's doctoral studies, and for his many helpful suggestions during the preparation of the thesis. Thanks are also due the other members of the writer's doctoral committee: Dr. O. B. Andersland, Associate Professor of Civil Engineering, Dr. T. T. Triffet, Professor of Applied Mechanics, Dr. L. E. Malvern, Professor of Applied Mechanics, and Dr. A. E. Erickson, Professor of Soil Science, for their guidance throughout the doctoral program. The writer is grateful to A. K. Loh and F. K. Holliday for their assistance in the laboratory.

Thanks go to Consumers Power Company, Jackson, Michigan, and to the National Science Foundation for the financial assistance that made the writer's doctoral studies possible.

TABLE OF CONTENTS

LIST OF TABLES

LIST OF FIGURES

NOTATION

$\mathring{A}$ = angstroms

A_c = actual contact area between two plane surfaces

$D = (\sigma_1 - \sigma_3)$ = principal stress difference or "deviator" stress

D^* = dimensionless stress relaxation function

e = void ratio

F = maximum shearing force in friction

F_f = flow force on interparticle bonds

ΔF = activation energy

h = Planck's constant

k = Boltzmann's constant

k_1, k_2 = spring "constants" of the structural model

P = normal force

R = universal gas constant

t = time

T = absolute temperature

U = axial deformation

U^* = dimensionless creep function

V_s = volume of solids in a clay mass

x = distance measured along the plane of flow

α = rate theory parameter associated with the geometry of the flowing unit

β = rate theory parameter associated with the activation energy of flow

γ = shear strain

γ_{oct} = octahedral shear strain

$\dot{\gamma}$ = shear strain rate

$\epsilon_1, \epsilon_2, \epsilon_3$ = principal strains

η = number of non-flowing bonds per unit area in the plane of flow

λ = distance between equilibrium points in the plane of flow

λ_1 = distance between points of flow in the direction perpendicular to the plane of flow

μ = total number of interparticle bonds per unit area in the plane of flow

μ_f = coefficient of friction

ν = number of flowing interparticle bonds per unit area in the plane of flow

$\sigma_1, \sigma_2, \sigma_3$ = principal stresses

σ_{yp} = yield strength in comparison

τ = shear stress

τ_{oct} = octahedral shear stress

τ_{yp} = yield stress in shear

ϕ = shear force on an interparticle bond

ϕ_y = yield strength of an interparticle bond in shear

Ψ = distribution of bond yield strengths

CHAPTER I

INTRODUCTION

The stress-deformation-time behavior of clays is not well understood. The principal reason for the lack of knowledge is that clays are extremely complex in their physical makeup. They consist of solid material (the individual clay particles), water, and sometimes air; and the manner in which these components are combined in nature is highly variable.

The individual particles, by themselves, comprise a class of substances with a wide range of physical properties (Grim, 1953). Furthermore, the geometry of the particle structure has a profound influence on clay properties and, depending upon the environment at the time of formation, the particle geometry can be quite different. A clear picture of the particle geometry in various types of clays was only recently obtained through the use of the electron microscope (Rosenquist, 1959).

The presence of water in the voids of the particle network further complicates clay behavior. It has long been recognized that the water nearest the clay particles is strongly attracted by the surfaces forces of the particles (see, for instance, Houwink, 1937) and has been arbitrarily designated as the adsorbed water layer. However, the nature

of the adsorbed water and its influence on clay properties is still not resolved (Lambe, 1960). Furthermore, the electrolyic content of the pore water influences the inter-particle force fields and, consequently, affects the particle geometry, water properties, and shearing strength of the clay (Moum and Rosenquist, 1960).

If air is present in the clay pores in addition to water, the situation is even more complicated. However, this investigation deals only with saturated clays.

Recently much interest has been focused on the properties of the clay-water system; i.e., the interaction of the solid and fluid phases in a clay mass. As a result, considerable knowledge has been gained in this area within the past few years. These recent developments are utilized herein in attempting to formulate a working hypothesis for particle behavior during deformation.

The approach to be adopted in this study is to treat the flow between individual clay particles as a rate process. Using the equation of flow from the rate theory, a model is devised to simulate the behavior of the particle structure under external loads. The rate process approach to material deformations is due to Eyring (Glasstone, Laidler, and Eyring, 1941) and has been extensively used in studying the mechanical properties of polymers (Tobolsky and Andrews, 1944), textiles (Eyring and Halsey, 1948), and colloidal suspensions (Tobolsky, Powell, and Eyring, 1943). Murayama

and Shibata (1958) recently applied the methods of rate theory to the flow properties of a Japanese Alluvial clay.

Results of triaxial shear tests for creep and stress relaxation loadings on two glacial lake clays are presented. The experimental results are compared with the behavior predicted by the model and the values of the model parameters calculated for each test.

Good agreement is found between the behavior predicted by the model and the experimental results. The values for the model parameters calculated by comparison of the theoretical and experimental curves are interpreted in terms of the particle structure.

It is hoped that this study will help to clarify the role of the particle structure in deformation of clays.

CHAPTER II

THEORETICAL CONSIDERATIONS

2.1 Nature of the Clay-Water System

It is well known that individual clay particles are thin, plate-like structures of a size less than 2 microns. Because of their size and geometry, these particles possess a very high surface area-to-mass ratio and are strongly influenced by surface forces.

In a clay-water system, the water in close proximity to the particle is attracted to the particle surface and forms what is called the adsorbed water film. The properties of the adsorbed water and its effect on the mechanical properties of clay masses are still uncertain.

It was thought for some time that the adsorbed water layers were rather thick--up to 0.1 microns according to Terzaghi and Peck (1948)--and quite viscous. The conclusion was drawn from this concept that the viscous nature of clays resulted from the presence of the viscous water layers surrounding each particle. Recent research indicates, however, that the thickness of water affected by the clay particles is no more than about 25 angstroms (see, for instance, Rosenquist, 1959).

It is generally agreed that the water immediately next to the clay particle is different from ordinary water. On

the basis of heat of swelling and vapor pressure-temperature data, Rosenquist (1959) calculated that a 10-angstrom layer of crystalline (ice-like) water surrounded the particles in the particular clay tested. Furthermore, Anderson and Low (1958) found that the specific volume of water near clay surfaces is greater than normal water. This data was cited by Low (1960) as evidence that the adsorbed water has a structure that is more ordered than that of normal water. Martin (1959), on the other hand, presented data that indicates that the water next to the particles is more disordered than normal water. The question of the structure of the water near the particle surfaces must, therefore, be considered unresolved.

Low (1960) found that the activation energy of the flow of water through Na-bentonite increases with time after wetting and concluded that the adsorbed water is more viscous than normal water. Rosenquist (1959) also found from deuteron-diffusion measurements that the adsorbed water on clay particles is more viscous than normal water. However, Michaels (1959) pointed out some of the shortcomings in assessing the properties of the adsorbed water from such indirect evidence. Michaels also suggested that the adsorbed water may be not only different from normal water but anisotropic; i.e., "the resistance offered by a water molecule being slid along the surface may be considerably less than that offered by a water molecule being elevated from or lowered toward the surface."

Leonards and Girault (1961) showed that the phenomenon of secondary compression in the consolidation test cannot be attributed to adsorbed water films alone. They found that clays in which the water had been replaced by carbon tetrachloride, a non-polar fluid, still exhibit secondary compression. Similarly, Norton (1952) described a simple experiment in which dry, powdered clay when placed in a elastic membrane and subjected to a vacuum behaves plastically in the same manner as a moist clay. These findings suggest that the adsorbed water on clay particles may be of relatively minor importance in the deformational properties of clays.

2.2 Clay Structure

A comprehensive description of clay structure was first presented by Tan (1953). The individual particles are assumed to form edge-to-face contacts with one another, resulting in a continuous solid skeleton in a "card-house" arrangement. Tan's concept was later verified by Rosenquist (1959) by means of electron microscopy. Figure 2.1 is a schematic drawing of a clay particle network according to Tan and is in remarkable agreement with Rosenquist's findings for undisturbed marine clays. Remolded clay structures are believed to be similar except that the network may consist of small "packets" of parallel particles rather than individual particles (Lambe, 1960; Mitchell, 1956).

Rosenquist (1959) also established that the individual particles are actually in mutual contact by quick freezing

Figure 2.1. Schematic picture of clay (After Tan)

undisturbed clay specimens in liquid air and sublimating off the ice. Little or no shrinkage was observed upon removal of the frozen pore water and the dried specimen had considerable strength, indicating the presence of a continuous particle network.

Several mechanisms of bonding between clay particles have been suggested: (1) Coulomb attractive forces, (2) van-der-Waals-London forces, (3) cation bonding, (4) hydrogen bonding, (5) ionic bonding, and (6) covalent bonding.

Direct methods for determining the relative magnitudes of the various bonding types is lacking but the Coulombic and van-der-Waals-London forces are generally thought to be the most predominant (see, for instance, Van Olphen, 1951; Rosenquist, 1959; Tan, 1959; and Lambe, 1953). In particular, Iler (1955) presented strong evidence for the existence of the Coulombic attraction between negatively charged flat

particle surfaces with positively charged edges by showing electron micrographs of negatively charged silica particles attracted to the edges of hectorite particles. It is likely that all the bond types mentioned are present in clays to some degree, but no reliable method for distinguishing their relative contribution to the interparticle bond is presently available.

According to the evidence currently available, the nature of clay particle structure may be summarized as follows:

1. The individual particles in a clay mass form a continuous solid skeleton in which edge-to-face contacts predominate.
2. At the contact points between particles, bonds are formed as a result of microscopic force fields in the clay-water system. These forces consist mainly of Coulomb attractive and repulsive forces and van-der-Waals-London forces. The combined effect of the microscopic force fields determines the strength of the interparticle bonds. These force fields are influenced by many factors; e.g., the size, shape and mineral composition of the particles, the electrolytes in the pore fluid, adsorbed cations, geometry of the structural network, void ratio, and perhaps others.

3. The adsorbed water films on the particle surfaces play a minor role in determining deformational behavior--it may affect the viscous flow of clays under stress but is probably not the prime cause of viscous flow.

2.3 Physical Aspects of Deformation

Since deformations in clays involve the interaction of discrete solid particles, a useful analogy can be drawn from the phenomenon of sliding friction between solid surfaces. According to modern concepts, friction is envisioned as being the shearing resistance developed by the interlocking asperities of two surfaces brought together under the action of a normal force (Bowden and Tabor, 1954). Even in the case of highly polished surfaces, actual contact occurs over a very small area so that the local stresses at the contact points are sufficient to produce yielding. Therefore, the total normal force

$$P = \sigma_{yp} A_c$$

where σ_{yp} is the yield stress in compression and A_c is the actual area of contact. The maximum shearing force that can be applied before failure occurs is

$$F = \tau_{yp} A_c$$

where τ_{yp} is the yield stress in shear. Since the coefficient of friction μ_f is defined as $\mu_f = \frac{F}{P}$, it can be seen that $\mu_f = \frac{\tau_{yp}}{\sigma_{yp}}$.

Burwell and Rabinowicz (1953) have shown that μ_f is not a constant, but depends upon the speed of sliding. For a given normal stress, they found that sliding occurs for a wide range of shearing forces--the coefficient of friction increases with the speed of sliding up to the point of failure. Horn and Deere (1962) found that the coefficient of friction of phlogopite mica also increases with the speed of sliding. It is probable that this relationship also applies to clay particles since clay particles have crystal structures similar to those of the micas.

Burwell and Rabinowicz described the frictional deformation process as the successive breaking of bonds formed by the interlocking asperities and subsequent formation of new bonds as the two surfaces move relative to one another producing new contacts. A similar process may be applicable to the phenomenon of sliding between clay particles. This application does not require that the clay particles are in direct contact, although this appears to be the case.

The deformational resistance of the clay structure rests in the bonds formed between particles at the points of contact. The strength of these bonds may vary widely in any given clay so that when external stresses are applied, some of these bonds will fail in shear while others remain intact. The particle movements which follow breakage of the bonds will tend to bring the displaced particles

into contact at other points as the deformation proceeds. The bonds which are broken may also be expected to reform in other positions due to attractive forces which exist between particles at close range. The resistance of clays to deformation is thus seen to depend upon the strength of the interparticle bonds and the number of these bonds per unit volume--a situation which is quite similar to the development of sliding resistance between solid surfaces.

In solids, the yield strength in shear, τ_{yp}, is usually assumed to be constant. However, in clays, the strength of reformed bonds may differ from the strength of the original bonds if the particle geometry is substantially altered during shear.

It was noted that the contact area in the case of sliding friction between solids is directly proportional to the normal force. In clays, on the other hand, the number of bonds per unit volume is primarily dependent upon the preconsolidation pressure and particle geometry. The consolidation process forces some of the water from the pore spaces, thus bringing the particles closer together and creating more interparticle contacts. Even after unloading, most of the bonds formed during consolidation remain intact because of the close range attractive forces. The particle geometry has considerable effect on the number of bonds in that more interparticle contacts are possible in a random arrangement than one in which the particles are aligned parallel to one another.

The number of bonds may, also, be considerably affected by shear stresses since the resulting shear strains tend to disrupt the particle structure.

The ability of clays to retain interparticle bonds upon unloading provides an explanation for the experimentally observed fact that preconsolidated clays possess a cohesion intercept on the Mohr-Coulomb diagram while normally consolidated clays do not (Rosenquist, 1959) Under the present hypothesis, therefore, the necessity of explaining friction and cohesion as two intrinsically different components of shearing resistance is eliminated since they are only different macroscopic manifestations of the same microscopic process.

The conclusion may be drawn from this brief discussion that deformation in clays under externally applied loads involves a continuous process of breaking and reforming interparticle bonds. Processes of this type are well suited to theoretical treatment by the theory of absolute reaction rates (Glasstone, Laidler, and Eyring, 1941). In the section which follows, this theory is adapted to clay particle structures.

2.4 Deformation of Clays as a Rate Process

The deformation of clays under applied stresses is assumed to be the result of the breaking and reforming of interparticle bonds which arise at the contact points between particles as the result of the microscopic force fields that

exist in the particle structure. The use of the term contact points is not intended to imply that the mineral surfaces of the particles are necessarily in actual contact, although such may be the case. A contact point, as the term is applied here, merely refers to the point at which a bond is formed between particles. Actual contact between the mineral surfaces is not required. Since the interparticle bond is the net result of the force fields of the "contact," the nature of the "contact" need not be specified here.

The interparticle bond is assumed to present an energy barrier to relative motion between particles. This energy barrier will be represented by the symmetrical potential surface shown in Figure 2.2a in which λ is the distance between the adjacent minimum positions A and B. In order to break the bond between particle surfaces, an amount of energy at least equal to the activation energy, ΔF, must be supplied to surmount the potential barrier. The energy required to raise the bond to its activated (loosened) state may result from thermal oscillation of the atoms and molecules making up the bond, applied stresses, or both. Even if no external stresses are acting, the bond is presumed to pass through the activated state with a frequency of

$$k' = \frac{kT}{h} e^{-\Delta F/RT} \quad \text{times per second}$$

where k is Boltzmann's constant, h is Planck's constant, T is the absolute temperature, and R is the universal gas

constant in accordance with the theory of absolute reaction rates (Glasstone, Laidler, and Eyring, 1941). In this case there is no net movement, however, since the frequency is the same in both directions.

It was noted earlier that clays possess a wide range of bond strengths due to the heterogeneous nature of the material. Therefore, in dealing with the breaking and reforming of bonds as a rate process, a broad spectrum of activation energies may be anticipated instead of a single value. In the development which follows, the value of ΔF is taken to represent the average of all bonds under consideration.

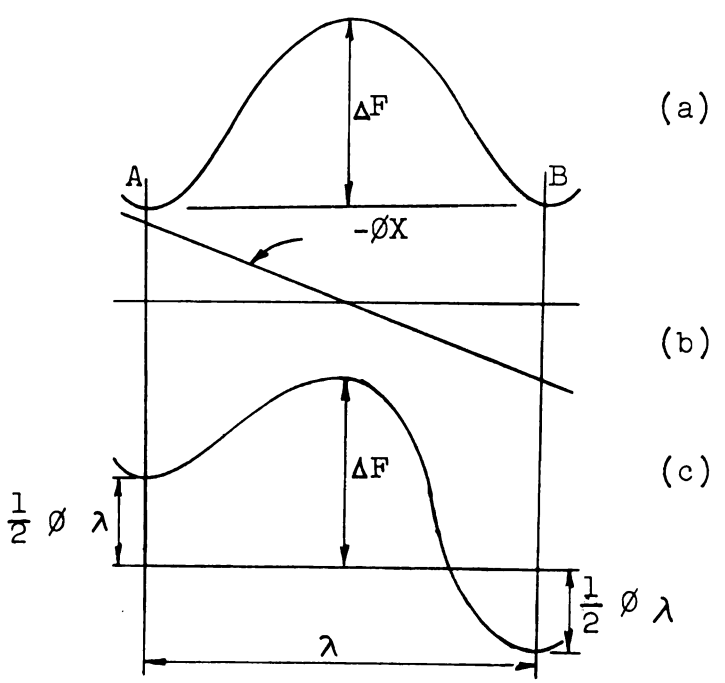

Figure 2.2. Potential surface for interparticle bond: (a) without external stresses, (b) energy gradient due to external stress, (c) with external stresses applied.

Consider now a certain plane in the material over which a shear stress τ acts. Let the average shear force exerted on a bond along the plane be ϕ. The effect of this force is to add to the potential surface, a potential gradient $-\phi x$, where x is the distance measured in the direction of the stress (Figure 2.2b). The new potential surface takes the form of Figure 2.2c. The force ϕ will do work $\phi \frac{\lambda}{2}$ in moving from A to B in the forward direction. If the movement is backward, or against the stress, the work done is $-\phi \frac{\lambda}{2}$. According to rate process theory (see, for instance, Tobolsky, Powell, and Eyring, 1943), the net rate of place change in the forward direction is, then,

$$k' \; e^{[\phi \lambda / 2kT} - e^{-\phi \lambda / 2kT]} = 2 k' \sinh \frac{\phi \lambda}{2kT} \text{ times per second} \qquad (2.1)$$

If the distance moved in each jump is λ and the average distance between points of flow in a direction perpendicular to the plane of flow is λ_1, the rate of shear strain is given by

$$\dot{\gamma} = 2 \frac{\lambda}{\lambda_1} \frac{kT}{h} e^{-\Delta F/RT} \sinh \frac{\phi \lambda}{2kT} \qquad (2.2)$$

Since the average force localized on the individual bonds is ϕ, thus $\tau = \phi \nu$, where ν is the number of bonds per unit area over the plane of shear.

The equation for shear deformation of the clay particle structure then becomes

$$\dot{\gamma} = 2 \frac{\lambda}{\lambda_1} \frac{kT}{h} e^{-\Delta F/RT} \sinh \frac{\tau \lambda}{2\nu kT} \qquad (2.3)$$

which is the general equation for non-newtonian viscous flow (Eyring and Halsey, 1943).

Having established the flow relationship of Equation 2.3, the total deformational behavior of clays is now considered.

2.5 A Model for Clay Structure

The flow relationship of Equation 2.3 is, by itself, inadequate to fully describe shear deformation in clays. The major characteristics of clay deformation in addition to viscous flow that must be taken into account in the theory are as follows.

Creep tests on clays show that an instantaneous deformation takes place immediately after the load is applied. This deformation is largely recoverable and has been attributed to bending in the clay plates and the rotation of the flat particle surfaces toward one another against the action of Coulomb repulsive forces (Tan, 1959).

Secondly, at stresses below the failure stress, the creep curves tend asymptotically toward some final deformation (Lo, 1961; Casagrande and Wilson, 1950). If the flow process comes to a halt, then the stress must be carried by intact bonds which do not flow. Hence, it may be assumed that a yield value exists, below which no movement occurs. Alternatively it may be said that when the force on a bond

is very small compared to ΔF the flow rate is not measurable. An explanation for the existence of a threshold stress is found in the hyperbolic character of the flow equation derived from rate theory (Eq. 2.3).

Equation 2.3 is of the form

$$\dot{\gamma} = A \sinh B \phi$$

where

$$A = 2 \frac{\lambda}{\lambda_1} \frac{kT}{h} e^{-\Delta F/RT} \quad \text{and} \quad B = \frac{\lambda}{2kT}$$

Now if $B >> A$ and B remains constant the flow curves will each have an apparent yield limit below which the flow rate is too small to be measured. This yield limit increases for decreasing values of A as shown in Figure 2.3.

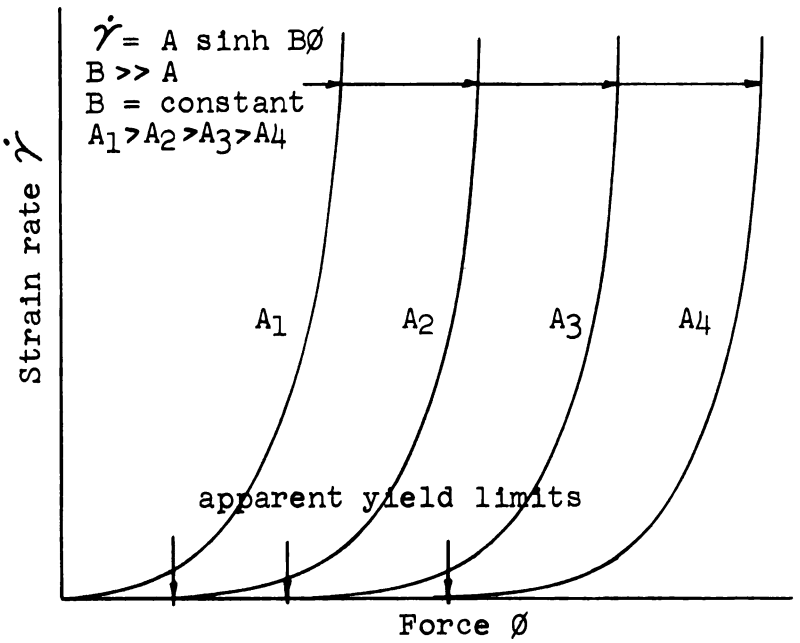

Figure 2.3. Flow curves for non-newtonian viscous flow showing apparent yield limits for the case $\dot{\gamma}$=A sinh BØ; B >> A.

Such flow curves have been observed on the macroscopic scale in creep tests on clays (Houwink, 1937; Geuze and Tan, 1953). Since A is inversely proportional to the exponential of the activation energy ΔF, the apparent yield limit ϕ_y increases with ΔF. If the force on a bond is below the apparent yield limit, the rate of flow is extremely small and may not be detected by laboratory measurements. If the rate of flow below the apparent yield point is taken as zero, the flow curve takes the form shown in Figure 2.4.

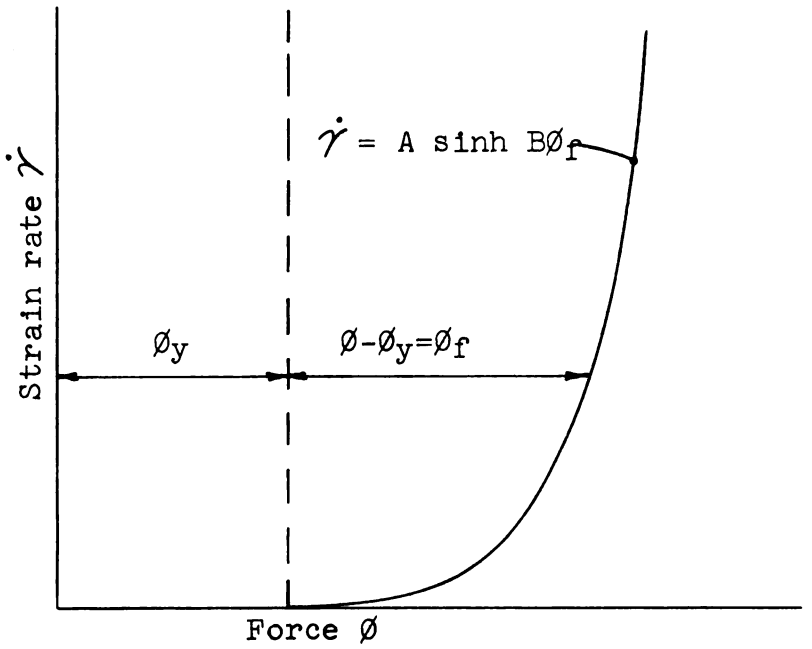

Figure 2.4. Flow curve for interparticle bond having yield strength ϕ_y.

According to this flow curve, the bond possesses a yield strength ϕ_y beyond which flow proceeds according to the relationship

$$\dot{\gamma} = A \sinh B \phi_f$$

where $\phi_f = \phi - \phi_y$ is the force on the bond in excess of the yield strength. No flow occurs at stresses below ϕ_y.

In a clay mass, a spectrum of yield strengths may be anticipated due to the wide range of activation energies. The solid curve in Figure 2.5a shows a hypothetical distribution of bonds with respect to yield strength for an unstressed particle structure. The area under the curve is equal to the total number of stress-carrying bonds μ per unit area in the plane of flow. Stress-carrying bonds are all those that will be stressed when external loads are applied. Thus $\mu = \nu + \eta$ in which ν is the number of bonds which flow and η is the number of bonds which do not flow.

Consider now the effect of external stresses on the particle structure. Under a given sequence of loading, the bond forces may be divided into the following categories.

ϕ_y = total yield strength of the bond

$\Delta\phi_{yn}$ = additional force that a bond can carry in the n^{th} increment before flowing or

$\Delta\phi_{yn}$ = yield strength of a bond for the n^{th} increment

$\Delta\phi_n$ = initial force exerted on a bond due to the n^{th} increment

$\Delta\phi_{fn}$ = flow force on a bond due to the n^{th} increment

ϕ_{gn} = non-flow force on a bond during the n^{th} increment

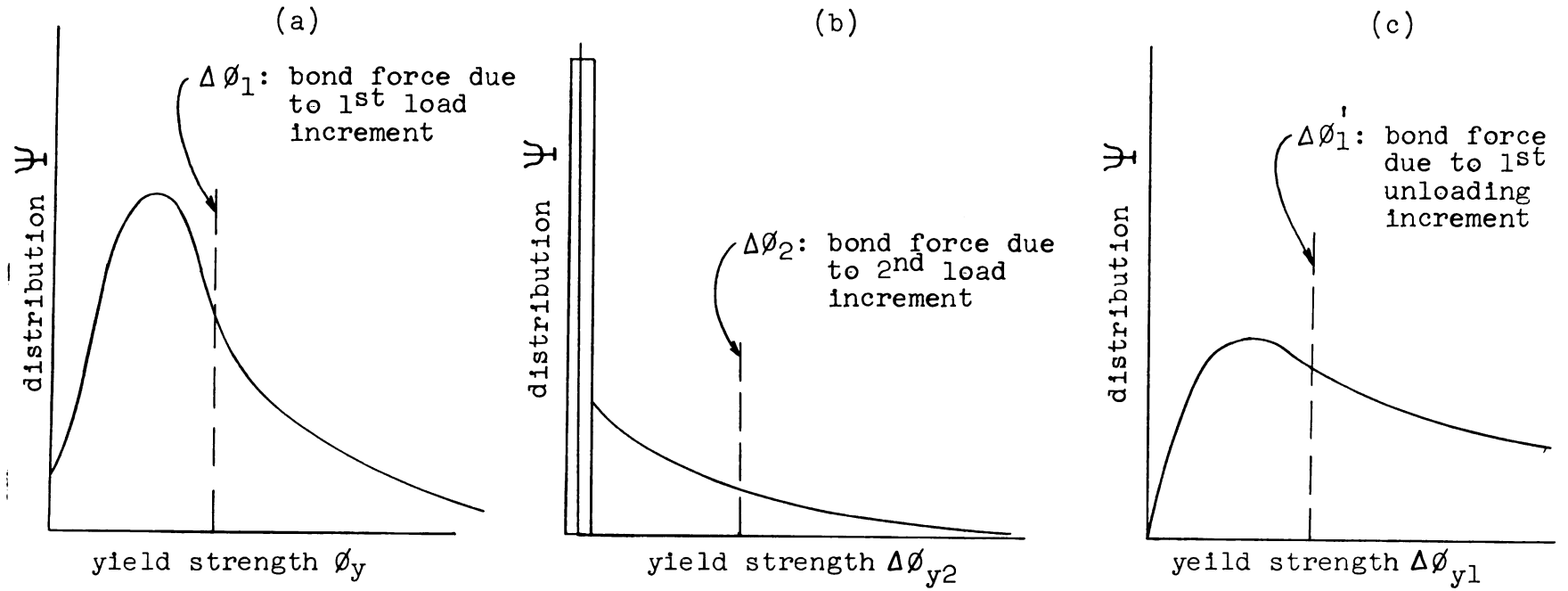

Figure 2.5 Hypothetical distribution of bond yield strengths with respect to: (a) unstressed particle structure, (b) second load increment, (c) first unloading increment.

Additional designations are defined where needed.

If a system of stresses is applied to the mass, the bond whose flow curve is given in Figure 2.4 is subjected to a force, say $\Delta\phi$. If $\Delta\phi$ is smaller than the yield stress ϕ_y, the bond reacts elastically and does not flow. However, if $\Delta\phi$ is larger than ϕ_y, the bond flows, immediately after the stresses are applied, under the force

$$(\Delta\phi_f)_o = \Delta\phi - \phi_y$$

Unless all the bonds are stressed beyond their yield point, the force $\Delta\phi_f$ is gradually transferred to the stronger bonds as flow proceeds. Thus, $\Delta\phi_f$ steadily decreases to zero and the bond ceases to flow. At this point, the flowing bond carries a force ϕ_y.

As a first approximation, it may be assumed that all the bonds initially carry an equal share of the applied stress. At the instant the first stress increment is applied, each bond then carries a force $\Delta\phi_1$. As Figure 2.5a shows, the force $\Delta\phi_1$ exceeds the yield strength of some of the bonds; these bonds flow until the flow force $\Delta\phi_{f1}$ on each flowing bond is diminished to zero by transfer to stronger bonds. The initial total force per unit area of particles tending to cause flow is

$$(F_{f1})_o = \sum_{o}^{\nu_o} (\Delta\phi_{f1})_o = \sum_{o}^{\nu_o} (\Delta\phi_1 - \Delta\phi_{y1})$$

where ν_o is the number of initially flowing bonds per unit area.

After deformations have ceased, the total flow force F_{f1} has been transferred to the initially non-flowing bonds so that they then carry the force

$$(\phi_{g1})_\infty = \Delta\phi_1 + \frac{(F_{f1})_o}{\eta_\infty}$$

where η_∞ is the number of bonds that did not flow during the first load increment.

At the end of deformation, the bonds which flowed are stressed to their yield strength, while those which did not flow have a yield strength

$$\Delta\phi_{y2} = \Delta\phi_{y1} - (\phi_{g1})_\infty$$

with respect to additional stress. The distribution of bonds with respect to $\Delta\phi_{y2}$ before application of a second load increment is as shown in Figure 2.5b. It will be noted that the number of bonds with any remaining yield strength is considerably reduced by the first load increment. The same processes take place during the second and all succeeding increments until all yield strength has been exhausted and failure occurs.

The application of the n^{th} load increment causes all the stressed bonds to be subjected to a force increment $\Delta\phi_n$. The initial flow force on any bond in the n^{th} increment is

$$(\Delta\phi_{fn})_o = \begin{cases} \Delta\phi_n, \text{ if } \Delta\phi_{yn} = 0 \\ \Delta\phi_n - \Delta\phi_{yn}, \text{ if } \Delta\phi_n > \Delta\phi_{yn} > 0 \\ 0, \text{ if } \Delta\phi_{yn} > \Delta\phi_n \end{cases}$$

while the initial non-flow force on any bond in the n^{th} increment is

$$(\phi_{gn}) = \begin{cases} \phi_y, \text{ if } \Delta\phi_n > \Delta\phi_{yn} \\ \phi_{g(n-1)} = \Delta\phi_n, \text{ if } \Delta\phi_{yn} > \Delta\phi_n \end{cases}$$

At the end of the n^{th} increment, the force carried by a given bond is

$$(\phi_{gn})_\infty = \begin{cases} \phi_y \text{ if } \Delta\phi_n > \Delta\phi_{yn} \\ \phi_{g(n-1)} + \Delta\phi_n + \dfrac{(F_{fn})_o}{\eta_\infty}, \text{ if } \Delta\phi_{yn} > \Delta\phi_n \end{cases}$$

If the clay mass is unloaded after the n^{th} increment--provided failure has not occurred--the yield strength of a bond in the first unloading increment is

$$\Delta\phi'_{y1} = \phi_y + (\phi_{gn})_\infty$$

Therefore, the initial bond distribution with respect to unloading takes the form of Figure 2.5c. This curve is elongated in the horizontal direction compared to that in Figure 2.5a due to the addition of the term $(\phi_{gn})_\infty$ to the yield strength of each bond. For unloading the flow process proceeds in the same manner as described for loading. However, it may be noted that the initial unloading force $\Delta\phi'_1$ produces fewer flowing bonds than the first loading force $\Delta\phi_1$. Therefore, the flow in the particle structure is considerably less during unloading. Inherent in this behavior is the experimentally observed fact that recovery is incomplete.

The deformational properties of the particle structure just described may be illustrated schematically by the model shown in Figure 2.6.

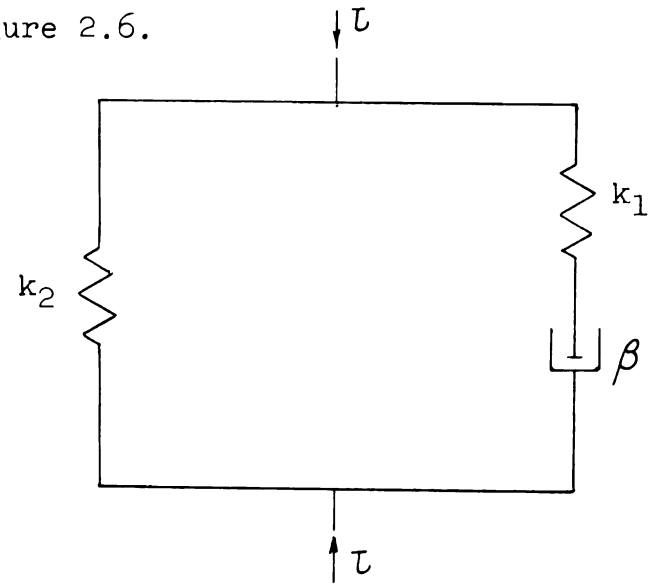

Figure 2.6. Schematic model for clay particle structure.

The spring k_2 represents the effect of bond stresses below the yield point--the stress on the non-flowing bonds plus the stress on the flowing bonds at or below the yield point. In this stress range the bonds are assumed to behave elastically. The right-hand side of the model represents the effects of the bond stresses which cause flow. The flow in the dashpot then represents the rate process.

Thus, when a shear stress τ is applied, elastic deformations occur in accordance with the combined resistance of $k_1 + k_2$ which indicates the elastic response of the particle structure as a unit. As the deformation proceeds, the stresses tending to cause flow are transferred to stronger bonds until all flow stops. The average flow properties of

all the flowing bonds under a given stress increment are represented by the dashpot β and, at any time, the stress in the right-hand side of the model is the stress producing flow.

It is readily seen that the model possesses the major deformational characteristics observed in clays. For example, if a constant load is applied, the springs k_1 and k_2 deform elastically, followed by viscous flow in the dashpot β until all the load is finally carried by the spring k_2 and the deformation ceases; it will be noted that this behavior agrees with that reported earlier for clays.

The shear stress in the left-hand side of the model is

$$\tau - \tau_1 = k_2 \gamma \tag{2.4}$$

where τ_1 is the shear stress in the viscous element and γ is the total shear strain. In the right-hand side, the shear stress is

$$\tau_1 = k_1 (\gamma - \gamma_1), \tag{2.5}$$

and according to Equation 2.3,

$$\dot{\gamma}_1 = \beta \sinh \alpha \tau_1 \tag{2.6}$$

where

$$\beta = 2 \frac{\lambda}{\lambda_1} \frac{kT}{h} e^{-\Delta F/RT} \quad \text{and} \quad \alpha = \frac{\lambda}{2 \nu kT} .$$

From Equation 2.4

$$\dot{\gamma} = \frac{1}{k_2} (\dot{\tau} - \dot{\tau}_1) \tag{2.7}$$

Combining Equations 2.5, 2.6, and 2.7,

$$\frac{k_1+k_2}{k_1k_2}\,\dot{\tau}_1 = \frac{1}{k_2}\,\dot{\tau} - \beta \sinh \alpha \tau_1$$

But for creep loading, $\dot{\tau} = 0$, so

$$\frac{k_1+k_2}{k_1k_2}\,\dot{\tau}_1 = -\beta \sinh \alpha \tau_1$$

or

$$\frac{d(\alpha \tau_1)}{d(\alpha\beta \frac{k_1k_2}{k_1+k_2}\, t)} = -\sinh \alpha \tau_1 \qquad (2.8)$$

Upon integrating Equation 2.8,

$$\tau_1 = -\frac{1}{\alpha} \ln \tanh\left[\frac{1}{2}\,\alpha\beta\,\frac{k_1k_2}{k_1+k_2}\,(t - C)\right] \qquad (2.9)$$

At the instant the load is applied,

$$t = 0 \quad \text{and} \quad \tau_1 = \frac{k_1}{k_1+k_2}\,\tau$$

so that

$$C = -\frac{2(k_1+k_2)}{\alpha\beta\, k_1k_2} \tanh^{-1} \exp\left(-\frac{\alpha k_1 \tau}{k_1+k_2}\right)$$

from which

$$\tau_1 = -\frac{1}{\alpha} \ln \tanh\left[\frac{1}{2}\,\alpha\beta\,\frac{k_1k_2}{k_1+k_2}\,t + \tanh^{-1} \exp\left(-\frac{\alpha k_1 \tau}{k_1+k_2}\right)\right] \qquad (2.10)$$

From Equation 2.4,

$$\gamma = \frac{1}{k_2}\,(\tau - \tau_1)$$

The creep equation thus becomes

$$\gamma = \frac{1}{k_2}\tau + \frac{1}{\alpha k_2} \ln \tanh \left[\frac{1}{2}\alpha\beta \frac{k_1 k_2}{k_1+k_2} t + \tanh^{-1} \exp\left(-\frac{\alpha k_1 \tau}{k_1+k_2}\right)\right] \quad (2.11)$$

In a similar manner, the differential equation for stress relaxation is found to be

$$\frac{d(\alpha\tau_1)}{d(\alpha\beta k_1 t)} = -\sinh \alpha\tau_1 \quad (2.12)$$

Integrating and applying the boundary condition,

$$\text{at } t = 0, \ \tau_1 = \tau_0 - \tau_\infty$$

the stress relaxation equation becomes

$$\tau = \tau_\infty - \frac{1}{\alpha} \ln \tanh \left[\frac{1}{2}\alpha\beta k_1 t + \tanh^{-1} \exp\left(-\alpha\left[\tau_0 - \tau_\infty\right]\right)\right] \quad (2.13)$$

Equations 2.11 and 2.13 describe the stress-strain-time behavior predicted by the model for creep loading and stress relaxation, respectively. The validity of the structural hypothesis developed in this chapter will depend upon the agreement between the experimental and theoretical behavior. The experimental program of this study is now presented.

CHAPTER III

EXPERIMENTAL PROGRAM

3.1 Objectives

The first purpose of the experimental program is to determine whether or not the proposed model reproduces adequately the actual deformational behavior of clays. Secondly, if the theoretical and experimental behavior show reasonable agreement, the experimental results may be used to evaluate the model parameters which would provide some insight into the particle nature of the deformation.

In order to achieve these objectives, creep and stress relaxation tests were performed on a number of specially prepared clay samples using a triaxial loading apparatus.

3.2 Clays Used

The majority of tests reported in this study were performed on specimens of a glacial lake clay obtained from a site approximately 15 miles south of Sault Ste. Marie, Michigan. The raw clay was obtained from a pit at a depth of about 15 inches. A series of diagnostic tests, including x-ray diffraction studies (Christensen, 1963) shows that this clay contains approximately 50% illite, 20% vermiculite, 20% chlorite, and some kaolinite and feldspars.

A few creep tests were also performed on an undisturbed glacial lake clay from Marine City, Michigan. Although identification tests have not been performed on this clay, it is presumed to be primarily an illite clay. The index properties for both the Sault Ste. Marie and Marine City clays are listed in Table 3.1.

TABLE 3.1. Index Properties of Clays Tested

Clay	L.L.	P.L.	P.I.	Clay Fraction
Sault Ste. Marie	60.5%	23.6%	36.2%	0.60
Marine City	41.4%	21.7%	19.7%	0.73

3.3 Sample Preparation

The Sault Ste. Marie clay was air dried in the laboratory prior to preparation of the test specimens. The various methods of sample preparation are described below.

a. Laboratory Consolidated Samples. The air dried clay was soaked in distilled water and remolded at a water content near the liquid limit. The remolded clay was placed in a 6 inch diameter lucite cylinder and left to stand for three weeks. An initial consolidation pressure of .003 kg/cm^2 was then placed on the clay. After at least 90% consolidation was reached, the pressure was doubled and maintained until 90% consolidation was again achieved. This procedure was repeated until the clay was consolidated under

a pressure of 0.36 kg/cm^2. The load was then removed and the clay allowed to rebound. Several weeks later, the clay was extruded from the cylinder and cut into six sections, each approximately 2 inches square in cross-section and 3.5 inches in height. These sections were then waxed, wrapped in aluminum foil, waxed again and stored in a moist room until required for testing. Immediately before testing, the waxed sections were trimmed into triaxial specimens 1.40 inches in diameter and 2.8 to 3.0 inches in length.

b. Remolded-Compacted Samples. The air dried clay was placed in a muller and reduced to a size less than 2 mm in diameter (No. 10 U. S. Standard Sieve). Distilled water was added until a water content of approximately 40% was achieved. The clay was then placed in an earthen crock, covered with a rubberized cloth and stored in a moist room to ensure an even water content distribution. After about two weeks, the clay was removed from the moist room and placed in a static compaction ring, 11.25 inches in diameter and 6.5 inches in height. The clay was placed in the compaction ring by hand, with a kneading action to remove as much of the air as possible. A pressure of 1 kg/cm^2 was applied to the clay by the loading ram of a hydraulic testing machine. The pressure was maintained for one hour, after which the load was released and the compacted cake removed from the ring. The cake was sliced into 21 sections, each approximately 2 inches square in cross-section and 4 inches

in height. The sections were then waxed, wrapped in aluminum foil, waxed again and stored in a moist room for at least two weeks prior to testing to allow equalization of moisture distribution and to minimize thixotropic effects. Immediately before testing, the sections were removed from the moist room and trimmed to a diameter of 1.40 inches and a height of 3.0 inches for triaxial testing.

c. Dry Clay Sample. The air dried clay was pulverized with mortar and pestle until it would pass a No. 100 (U. S. Standard) sieve. The pulverized clay was placed in a drying oven at 105°C and left for twenty-four hours. After removal from the drying oven, the clay was formed into a cylindrical specimen and placed inside a rubber membrane fitted to a cylindrical specimen mold. The clay powder was compacted with a rod to densify the mass. After filling the mold, the sample was fitted at the top with a lucite loading cap and sealed. A vacuum was then applied to the sample through the pore pressure line in the pedestal base. All water had previously been removed from this line so that no moisture could reach the dry sample. With the dry sample being supported by the vacuum, the sample mold was removed, the detachable cylinder and cap of the triaxial cell secured in place, and the chamber filled with water. Prior to applying the chamber pressure, the sample dimensions were taken. The weight of dry clay in the sample was determined by weighing the supply of dried clay before and after forming the sample.

d. Undisturbed Marine City Sample: The undisturbed Marine City clay was obtained by means of thin-walled piston samplers with an inner diameter of 3 inches. Triaxial specimens were trimmed from the tube samples to the same dimensions as the remolded-compacted samples. Data pertaining to each of the individual test samples may be found in Table 3.2.

3.4 Triaxial Tests

All test specimens were subjected to a hydrostatic consolidation pressure of 2.0 kg/cm^2 which remained until at least 90% consolidation was reached. Except for the dry clay, a back pressure of 1.5 kg/cm^2 was applied after consolidation by raising the chamber pressure and pore pressure simultaneously in increments of 0.1 kg/cm^2. The back pressure was maintained for at least twelve hours before testing.

a. Creep Tests. The creep loads were applied by means of a yoke resting on the loading piston. The yoke was fitted with a hanger from which the weights, required to produce a certain stress, could be suspended. These weights were placed on the hanger with great care to avoid subjecting the sample to shock loading.

A dial gage, of sensitivity 0.001 inches or 0.0001 inches, was attached to a mount on the triaxial cell with the stem resting on the loading yoke so that the vertical (axial) deformation of the specimen could be measured.

Throughout the test, the chamber pressure was maintained constant by means of a constant pressure cell.

From the instant the creep load was applied, the axial deformation and pore pressure were recorded at thirty seconds, one minute, two minutes, five minutes, and so on with the time interval between readings being approximately doubled after each reading. These data, along with the constant volume conditions permit the calculation of the effective principal stresses and principal strains.

Each creep load was maintained until the deformation had practically ceased and the pore pressure had reached equilibrium. The length of time required to achieve this condition varied from about one hour to more than one week depending on the stress level and the stress history of the specimen.

The loading program was varied considerably for different test specimens. Some specimens received only one large creep load, while others were loaded in small increments. Still others were cyclically loaded; i. e., the load was increased in small increments and then unloaded in similar increments until all the axial stress had been removed. The results of the cyclic loading tests are particularly interesting because they permit a comparison of the behavior of the material in loading and unloading.

b. Relaxation Tests: The specimens were subjected to a constant rate of deformation by means of a constant speed

drive mechanism. At a predetermined deformation, the drive mechanism was disengaged and the deformation maintained constant.

From the instant the deformation was stopped, the axial stress, pore pressure and time were recorded at time intervals which were approximately doubled after each reading. The axial stress was measured by means of a proving ring in the earlier tests and later by means of a load cell. The load cell, the design of which is described by Schmertmann (1960), was employed in order to minimize creep in the specimen during stress relaxation. Since the relaxation of stress in the proving ring produces substantial deformation in the specimen, it was thought that the measured decay of axial stress might not represent true stress relaxation. After checking the proving ring results with those from the load cell which deforms very little with relaxation of stress, it was found that the creep induced by the proving ring had little or no effect on the measured stresses.

The room temperature was recorded during all tests by means of a continuously recording temperature gage. During the winter months, when most of the tests were performed, the temperature control was very good--variations greater than 2°C were rare. During the summer months, however, the room temperature varied as much as 10°C during the testing of a single specimen. The temperature effects were most pronounced on the stress relaxation tests--in several cases,

rendering the data useless. The effect on the creep tests, although less severe, could also be seen in changes in slope in the deformation-time curves. Where temperature fluctuations became appreciable, this fact is noted in the data which is presented in the Appendix.

A complete listing of the specimens tested and the type of test performed on each is provided in Table 3.2. The results obtained from the experimental program are now presented and analyzed in terms of the theory developed in Chapter II.

TABLE 3.2. Summary of Triaxial Tests

Sample Number	Clay Type	Preparation	Test	Initial Void Ratio	Final Void Ratio
C-C-1	Sault	Compacted	Undrained Creep-Incremental-Cyclic	1.152	.785
C-C-7	Sault	Compacted	Undrained Creep-Single Load	1.183	.804
F-C-1	Sault	Consolidated	Undrained Creep-Incremental	1.337	.868
F-C-2	Sault	Consolidated	Undrained Creep-Incremental-Cyclic	1.287	.801
F-C-8	Sault	Consolidated	Undrained Creep-Incremental-Cyclic	1.339	.851
F-C-9	Sault	Consolidated	Undrained Creep-Single Load	1.462	.860
DP-C-1	Sault	Dry	Undrained Creep-Single Load	1.642	1.132
D-C-9	Marine City	Undisturbed	Undrained Creep-Incremental	.662	.662
F-R-5	Sault	Consolidated	Undrained Stress Relaxation	1.318	.803
F-R-6	Sault	Consolidated	"	1.308	.872
F-R-8	Sault	Consolidated	"	1.350	.844

CHAPTER IV

EXPERIMENTAL RESULTS

4.1 Presentation of Data and Evaluation of Model Parameters

In this chapter, the experimental results of this investigation are analyzed in terms of the structural model described in Chapter II. The first problem to be considered is that of devising a consistent method of data representation which will enable the model parameters to be determined quickly and consistently. In the following discussion, such a method is presented.

Consider the theoretical creep equation derived for the structural model in Chapter II,

$$\gamma = \frac{\tau}{k_2} + \frac{1}{k_2 \alpha} \ln \tanh \left[\frac{1}{2} \alpha \beta \frac{k_1 k_2}{k_1 + k_2} t + \tanh^{-1} \exp \left(-\alpha \tau \frac{k_1}{k_1 + k_2} \right) \right] \qquad (2.11)$$

In a three-dimensional stress system, the shear stresses and strains on the octahedral plane give a good representation of the shear distortion in the specimen. The octahedral shear stress is given by

$$\tau_{oct} = \frac{1}{3} \sqrt{(\sigma_1 - \sigma_2)^2 + (\sigma_2 - \sigma_3)^2 + (\sigma_3 - \sigma_1)^2}$$

and the octahedral shear strain is

$$\gamma_{oct} = \frac{2}{3}\sqrt{(\epsilon_1 - \epsilon_2)^2 + (\epsilon_2 - \epsilon_3)^2 + (\epsilon_3 - \epsilon_1)^2}$$

In the triaxial test, the principal stress difference $(\sigma_1 - \sigma_3)$ and the major principal (axial) strain ϵ_1 are conveniently measured. Under constant volume conditions, the stress and strain conditions imposed on the specimen are

$$\sigma_1 \; ; \; \sigma_2 = \sigma_3$$

and

$$\epsilon_1 \; ; \; \epsilon_2 = \epsilon_3 \; ; \; \epsilon_1 + \epsilon_2 + \epsilon_3 = 0$$

assuming that the strains are uniform.

With these conditions imposed, the octahedral shear stress is given by

$$\tau_{oct} = \frac{\sqrt{2}}{3}(\sigma_1 - \sigma_3) = \frac{\sqrt{2}}{3} D$$

in which D is the principal stress difference or the "deviator" stress as it is frequently called in the nomenclature of soil mechanics. The octahedral shear strain is

$$\gamma_{oct} = \sqrt{2}\,\epsilon_1$$

in terms of the axial strain ϵ_1

Equation 2.11 can now be rewritten in terms of the measured quantities D and ϵ_1 as

$$\epsilon_1 = \frac{D}{3k_2} + \frac{1}{\sqrt{2}\alpha k_2} \ln \tanh \left[\frac{1}{2} \alpha \beta \frac{k_1 k_2}{k_1 + k_2} t + \tanh^{-1} \exp - \left(\frac{\sqrt{2}}{3} \alpha D \frac{k_1}{k_1 + k_2} \right) \right] \qquad (4.1)$$

Immediately after application of the load (t = 0), the instantaneous strain is

$$(\epsilon_1)_o = \frac{D}{3(k_1 + k_2)} ,$$

while the ultimate strain under a given load (at $t = \infty$) is

$$(\epsilon_1)_\infty = \frac{D}{3 k_2}$$

These relations can be combined with Equation 4.1 to obtain a dimensionless creep function of the form

$$U^* = 1 + \frac{1}{A} \ln \tanh \left[Z(t) + \tanh^{-1} \exp (-A) \right] \quad (4.2)$$

where $U^* = \frac{\epsilon_1 - (\epsilon_1)_o}{(\epsilon_1)_\infty - (\epsilon_1)_o} = \frac{U - U_o}{U_\infty - U_o}$, U = axial deformation,

$$A = \frac{\sqrt{2}}{3} \alpha D \frac{k_1}{k_1+k_2} ; \quad Z(t) = \frac{1}{2} \alpha \beta \frac{k_1 k_2}{k_1+k_2} t .$$

The dimensionless creep function U* is seen to be dependent upon the parameter A and the time function Z(t) and varies between the limits of zero and one. By varying the parameter A, and plotting U* versus log Z(t), the family of curves shown in Figure 4.1 is obtained.

To determine the parameters α and β, the experimental data is plotted as $\frac{U - U_o}{U_\infty - U_o} = U^*$ versus log t. The sheet containing these points is then placed over the theoretical curves and adjusted horizontally until the points coincide with one of the theoretical curves, as nearly as possible. The choice of the best theoretical curve to fit the data

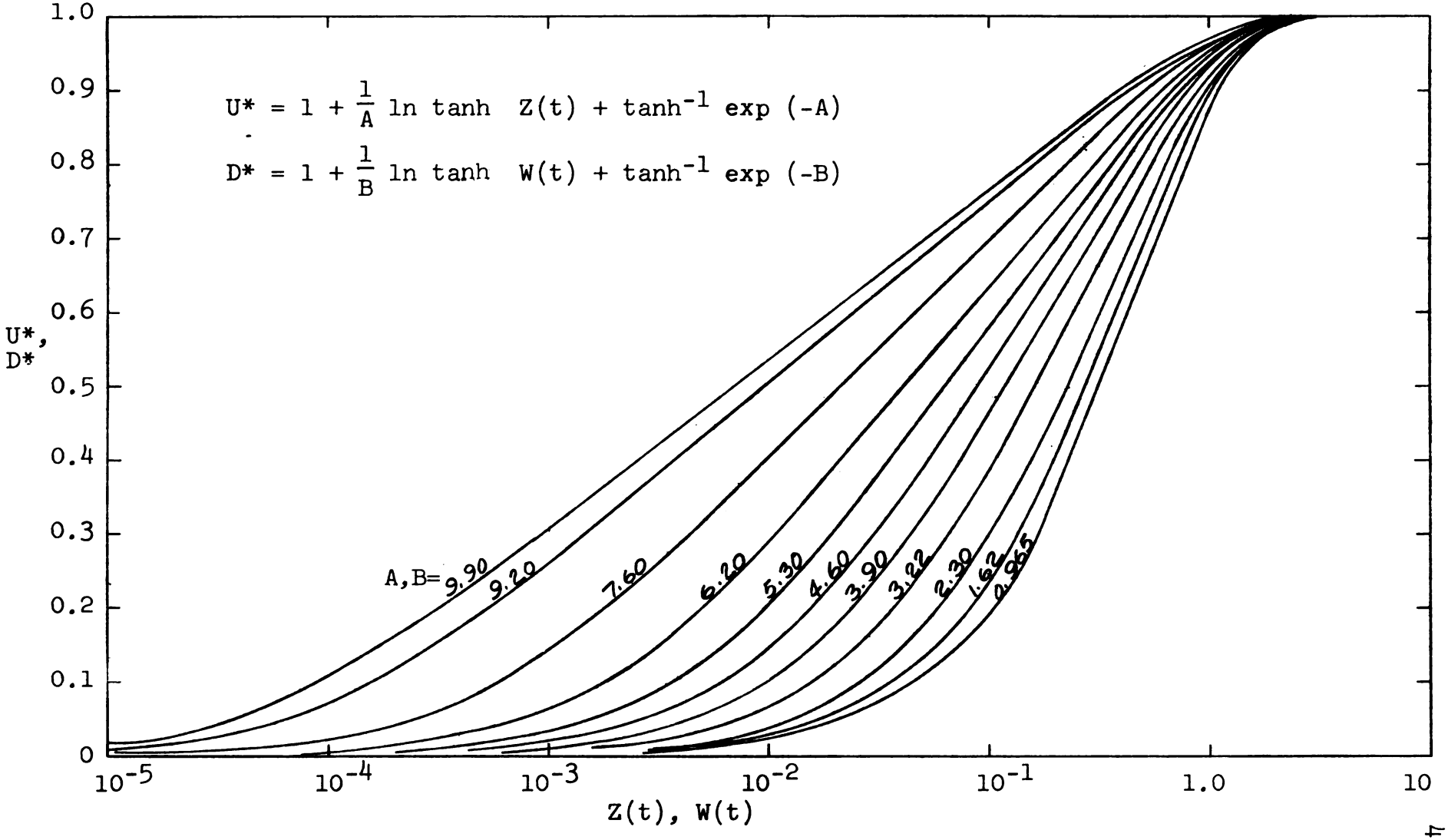

Figure 4.1. Dimensionless creep and stress relaxation curves for structural model.

determines the value of the parameter A for that test. With k_1 and k_2 known from separate considerations, the parameter α may be calculated from the relation

$$\alpha = \frac{3}{\sqrt{2}} \frac{A}{D} \frac{k_1 + k_2}{k_1} \tag{4.3}$$

The parameter β is found by noting the value of time t, on the experimental curve, which coincides with some arbitrary value of Z(t) on the theoretical curve sheet, since,

$$\beta = \frac{2Z(t)(k_1+k_2)}{k_1 k_2 \alpha t} \tag{4.4}$$

With k_1 and k_2 calculated from the instantaneous and ultimate creep strains and α and β evaluated by the curve fitting technique, all of the model parameters are determined.

In the relaxation test,

$$\tau = \tau_\infty - \frac{1}{\alpha} \ln \tanh \left[\frac{1}{2} \alpha\beta k_1 t + \tanh^{-1} \exp \left(-\alpha(\tau_o - \tau_\infty) \right) \right] \tag{2.13}$$

or, in terms of the principal stress difference, D,

$$D = D_\infty - \frac{3}{\alpha\sqrt{2}} \ln \tanh \left[\frac{1}{2} \alpha\beta k_1 t + \tanh^{-1} \exp \left(-\frac{\sqrt{2}}{3} \alpha (D_o - D_\infty) \right) \right] \tag{4.5}$$

In the same manner as described for the case of creep loading, a dimensionless stress relaxation function is obtained in the form

$$D^* = 1 + \frac{1}{B} \ln \tanh \left[W(t) + \tanh^{-1} \exp (-B \quad) \right] \qquad (4.6)$$

where $B = \frac{\sqrt{2}}{3} \alpha (D_o - D_\infty)$, $W(t) = \frac{1}{2} \alpha \beta \; k_1 t$,

$$D^* = \frac{D_o - D}{D_o - D_\infty}$$

The dimensionless stress relaxation function D* depends upon the parameter B and the time function W(t) and varies between zero and one. D* is seen to be of the same form as U* and so the same theoretical curves can be utilized for both creep and stress relaxation. The determination of α and β for the relaxation test is carried out in the manner as described for the creep test, where, now

$$\alpha = \frac{3B}{\sqrt{2} \quad (D_o - \quad D_\infty)} \qquad (4.7)$$

and

$$\beta = \frac{2W(t)}{\alpha \, k_1 t} \qquad (4.8)$$

It was found during the course of the experimental investigations, that the ultimate values of strain and deviator stress for creep and relaxation respectively were rarely reached within reasonable testing times. The time intervals required were normally greater than one week and in some cases more than a month. During that time the test samples were often subjected to accidental shocks or vibrations on the loading frame and/or temperature fluctuations. Efforts to eliminate these environmental factors were unsuccessful, so a method was sought by which these ultimate values could be determined by the shape of the curves within

shorter time intervals. For the case of creep, such a method was developed by considering the variation of strain rate with strain.

Consider again the theoretical creep equation in the form

$$\epsilon = F + G \ln \tanh \left[Ht + J \right] \tag{4.9}$$

where $F = \frac{D}{3k_2}$, $G = \sqrt{\frac{1}{2 \alpha k_2}}$, $H = \frac{1}{2} \alpha \beta \frac{k_1 k_2}{k_1 + k_2}$,

$$J = \tanh^{-1} \exp - \left(\sqrt{\frac{2}{3}} \alpha D \frac{k_1}{k_1 + k_2} \right)$$

The variation of strain rate with strain is given by

$$\frac{d\dot{\epsilon}}{d\epsilon} = \frac{d\dot{\epsilon}}{dt} \cdot \frac{dt}{d\epsilon} = \frac{\ddot{\epsilon}}{\dot{\epsilon}}$$

Taking the first two derivatives of equation (4.4) yields

$$\dot{\epsilon} = 2GH \operatorname{csch} 2 (Ht + J)$$

and

$$\ddot{\epsilon} = \frac{-4GH^2 \operatorname{csch} 2 (Ht + J)}{\tanh 2 (HT + J)}$$

from which

$$\frac{d\dot{\epsilon}}{d\epsilon} = \frac{d\dot{U}}{dU} = - 2H \coth 2 (Ht + J) \tag{4.10}$$

For $(Ht + J) > 1$, $\frac{d\dot{U}}{dU} \approx -2H \approx$ a constant. Hence, a simple arithmetic plot of $\dot{U}$ versus U should produce a curve which, after sufficient time has elapsed, will have a constant slope of -2H. Extrapolating the straight portion of this curve to $\dot{U} = 0$ will then yield the required value of U_∞ , the ultimate strain. This technique proved to be a very convenient means of determining U_∞ and also provided a valuable

check on the value of $\alpha\beta$ obtained from the curve fitting technique.

An analogous procedure can be applied to the stress relaxation data. In this case the required expressions are

$$D = D_\infty - L \ln \tanh \left[Mt + N \right] \tag{4.11}$$

and $$\frac{d\dot{D}}{dD} = + 2M \coth (Mt + N) \tag{4.12}$$

where $L = \frac{3}{\sqrt{2}\,\alpha}$, $M = \frac{1}{2}\alpha\beta\, k_1$,
$N = \tanh^{-1} \exp - \sqrt{\frac{2}{3}} (D_o - D)$

for $(Mt + N) > 1$, $\frac{d\dot{D}}{dD} \approx +2M$. The ultimate deviator stress, D_∞, is obtained by extrapolating the curve $\dot{D}$ versus D to $\dot{D} = 0$ and the value of $\alpha\beta$ can be compared to that obtained by the separate determination of α and β described earlier.

The complete procedure used in analyzing the experimental data for determination of the model parameters is now summarized.

Creep

1. Plot observed deformation-time readings as U versus t. The initial portion of the U-t curve is plotted on an exaggerated time scale and extrapolated to t = 0 to find U_o. Calculate $k_1 + k_2 = \frac{D}{3\epsilon_o}$.
2. From U-t curve, calculate the deformation rate $\dot{U}$ at several points along the curve and plot $\dot{U}$ versus U. Extrapolate the $\dot{U}$-U curve to $\dot{U} = 0$ and find U_∞. Calculate $k_2 = \frac{D}{3\epsilon_\infty}$ and $k_1 = (k_1 + k_2) - k_2$.

From the final straight portion of the $\dot{U}$-U curve evaluate $2H = -\frac{d\dot{U}}{dU}_{\infty}$ and calculate $\alpha\beta = 2H \frac{k_1 + k_2}{k_1 k_2}$.

3. Plot deformation-time data as $\frac{U-U_o}{U_\infty - U_o} = U^*$ versus log t and find the theoretical curve which best fits the data points. Calculate α and β from Equations 4.3 and 4.4. Compare $\alpha\beta$ with the value found in 2.

Stress Relaxation

1. From deviator stress-time data, plot D versus t.
2. From D-t curve, calculate $\dot{D}$ at several points along the curve and plot $\dot{D}$ versus D. Extrapolate the final straight portion of the $\dot{D}$-D curve to $\dot{D} = 0$ and find D_∞. Calculate $\alpha\beta = 2M \frac{1}{k_1} = +\left(\frac{d\dot{D}}{dD}\right)_\infty \frac{1}{k_1}$.
3. Plot $\frac{D_o - D}{D_o - D_\infty} = D^*$ versus log t and find the theoretical curve which best fits the data points. Calculate α and β from Equations 4.7 and 4.8 and compare $\alpha\beta$ with the value obtained in 2.

Figures 4.2, 4.3, 4.4, and 4.5 illustrate the determination of the model parameters for typical creep and stress relaxation tests. Supplementary data are given in the Appendix.

4.2 Validity of the Structural Model

The stress-strain-time behavior predicted by the structural model is represented by the dimensionless creep and relaxation functions U* and D* as shown in Figure 4.1,

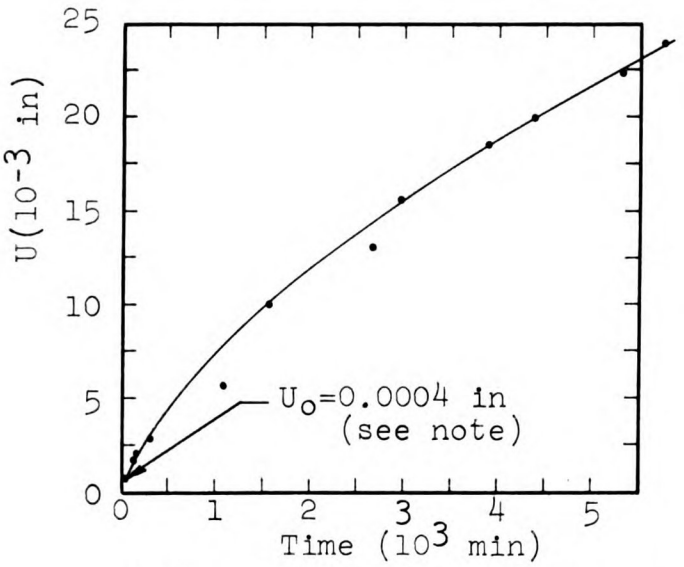

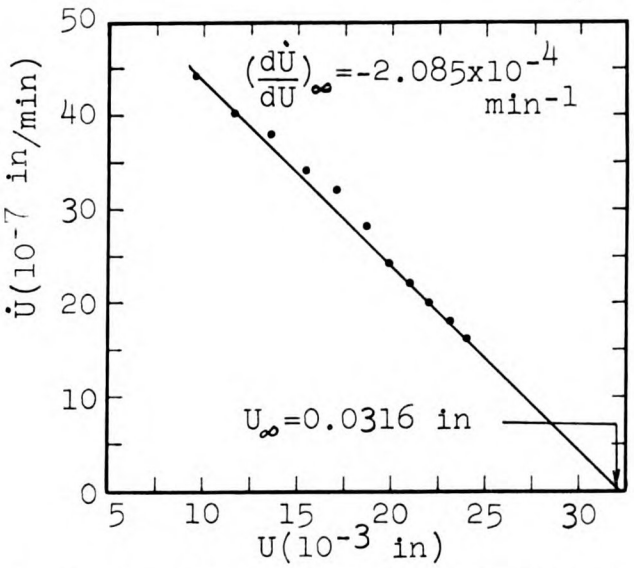

Note: U_o determined from separate U-t plot with exaggerated time scale (not shown).

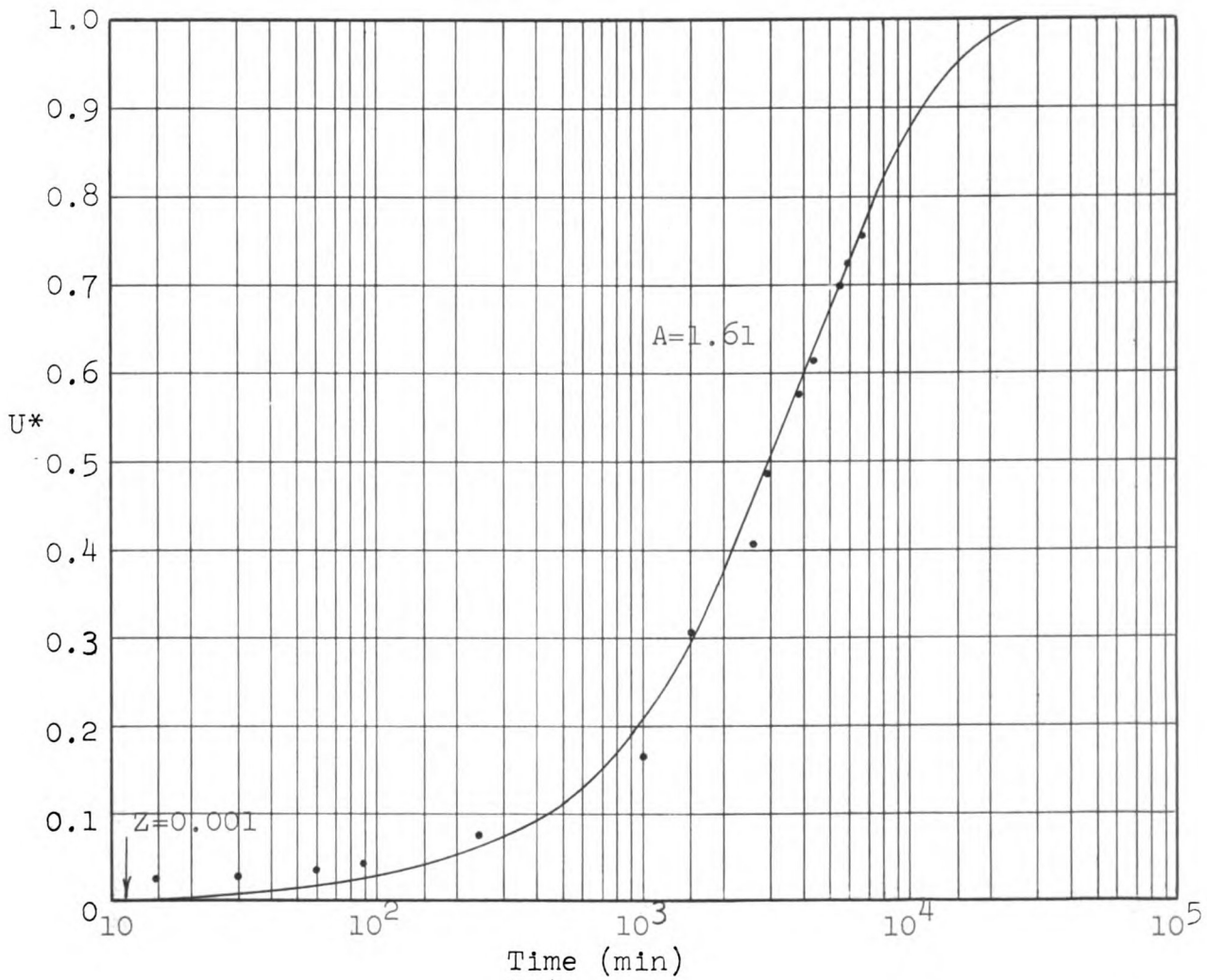

Figure 4.2. Typical creep curves (Test No. C-C-1-5).

Test Data

Test No. C-C-1-5
Initial sample length, l_o = 2.82 in
Initial deviator stress increment = 0.261 kg/cm^2
Final deviator stress increment = 0.250 kg/cm^2

U_o = 0.0004 in
U_∞ = 0.0316 in
$(\frac{d\dot{U}}{dU})_\infty = -2.085 \times 10^{-4} min^{-1}$
A = 1.61
Z (10.1 min) = 0.001

Calculations

$k_1+k_2 = \frac{D}{3\epsilon_o}$; $\epsilon_o = \frac{U_o}{l_o}$; $k_1+k_2 = \frac{D}{3U_o} \times l_o = \frac{0.261}{3(0.0004)}(2.82)$; $k_1+k_2 = 613\ kg/cm^2$

$k_2 = \frac{D}{3\epsilon_\infty}$; $\epsilon_\infty = \frac{U}{l_o}$; $k_2 = \frac{D}{3U_\infty} \times l_o = \frac{0.250}{3(0.0316)}(2.82)$ $\quad k_2 = 7.44\ kg/cm^2$

$k_1 = (k_1+k_2) - k_2 = 613-7$ $\quad k_1 = 606\ kg/cm^2$

$\frac{k_1}{k_1+k_2} = \frac{606}{613}$ $\quad \frac{k_1}{k_1+k_2} = 0.988$

$\alpha\beta = 2H \frac{k_1+k_2}{k_1 k_2}$; $2H = -(\frac{d\dot{U}}{dU})_\infty$; $\alpha\beta = 2.085\ (\frac{613}{606 \times 7.44})$; $\quad \alpha\beta\ (\text{method 2}) = 28.4 \times 10^{-6}\ cm^2/kg\ min$

$\alpha = \frac{3}{\sqrt{2}} \frac{A}{D} \frac{k_1+k_2}{k_1} = (\frac{3}{\sqrt{2}})(\frac{1.61}{0.250})(\frac{613}{606})$; $\quad \alpha = 13.84\ cm^2/kg$

$\beta = \frac{2Z(t)(k_1+k_2)}{k_1 k_2 \alpha t} \quad \frac{2(0.001)(613)}{(7.44)(606)(13.84)(10.1)}$; $\quad \beta = 19.48 \times 10^{-7} min^{-1}$

$\alpha\beta = (13.84)(19.48 \times 10^{-7})$; $\quad \alpha\beta\ (\text{method 1}) = 26.9 \times 10^{-6}\ cm^2/kg\ min$

Figure 4.3. Calculation of model parameters from creep test.

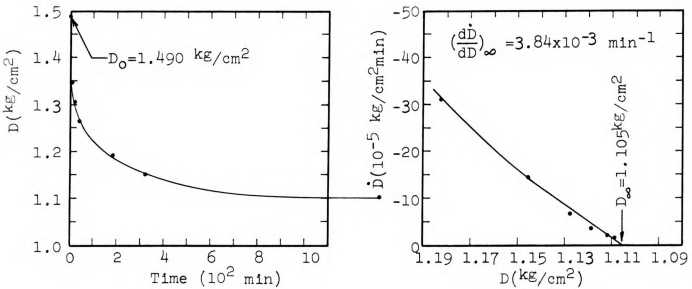

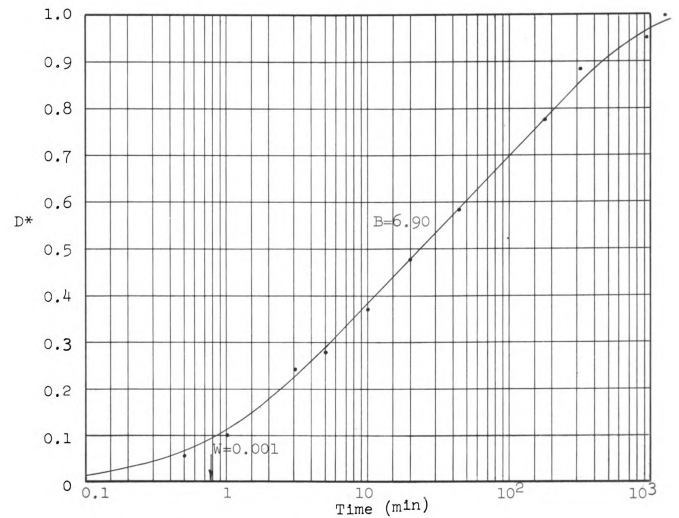

Figure 4.4. Typical stress relaxation curves (Test No. F-R-5-1).

Test Data

Test No. F-R-5-1
$D_o = 1.490\ kg/cm^2$
$D_\infty = 1.1075\ kg/cm^2$
$B = 6.90$
$W(0.78)min) = 0.001$

$$\left(\frac{\dot{dD}}{dD}\right)_\infty = 3.83\times10^{-3}\ min^{-1}$$

Calculations

$$\alpha\beta = 2M\frac{1}{k_1} = \left(\frac{\dot{dD}}{dD}\right)_\infty\left(\frac{1}{k}\right)$$

assume $k_1 = 167\ kg/cm^2$ from creep tests on comparable specimens,

$$\alpha\beta = (3.84\times10^{-3})\left(\frac{1}{167}\right);$$

$$\underline{\alpha\beta\ (\text{method 2}) = 22.9\times10^{-6}\ cm^2/kg\ min}$$

$$\alpha = \frac{3B}{\sqrt{2}\,(D_o - D_\infty)} = \frac{3(6.90)}{\sqrt{2}\,(1.490-1.1075)};$$

$$\underline{\alpha = 38.2\ cm^2/kg}$$

$$\beta = \frac{2W(t)}{\alpha k_1 t} = \frac{2(0.001)}{(38.2)(167)(0.78)};$$

$$\underline{\beta = 4.02\times10^{-7}\ min^{-1}}$$

$$\alpha\beta = (38.2)(4.03\times10^{-7})$$

$$\underline{\alpha\beta\ (\text{method 1}) = 15.40\times10^{-6}\ cm^2/kg\ min}$$

Figure 4.5. Calculation of model parameters from stress relaxation test.

and the ability of the model to predict the behavior of clays depends upon the agreement of the experimental data points with these theoretical curves.

The data collected from each test performed in connection with this study are presented in the Appendix. From inspection of these data, it can be seen that the agreement between theory and experiment is quite good in most cases. It would appear from the experimental evidence that the structural model used herein to describe the deformational properties of clays is a close approximation to the real behavior. The evidence is, of course, indirect since only the large-scale behavior of the clays can be observed and compared with the theory. However, this is the plight of most microscopic theories of material behavior, and their validity can only be tested by such comparisons.

For some increments of creep loading, tne deformations were very small, and the dial readings from these tests were somewhat approximate since it was necessary to interpolate between the smallest dial divisions. Therefore, each set of test data contains a note as to the accuracy of the data points obtainable from the dial readings, assuming that readings can be accurately interpolated to one-half of the smallest division. In those tests for which the scatter of the experimental data seems to be excessive at first glance, much of this scatter can be attributed to the limitations of the dial readings.

In some of the creep tests, particularly the first stages of unloading and reloading, reliable readings could not be obtained at all because the deformations were too small or took place too rapidly to be recorded with reasonable accuracy. Consequently, no creep curves are shown for these tests.

The question may be raised whether or not the actual creep and relaxation curves tend asymptotically to some ultimate value as predicted by the theoretical curves, since the final portion of the curves is missing in most cases. As mentioned in the previous section, the experimental data often became erratic in this region due to uncontrollable environmental factors. Consequently, it cannot be stated with absolute certainty that all the experimental curves approach an ultimate value. There is considerable evidence in support of this assumption, however.

In several tests, the ultimate strain appears to have been achieved (see for instance, Figure A.33). Moreover, the ultimate strain was frequently as difficult to record for unloading increments as for loading and it is quite obvious that recovery strains cannot continue indefinitely. In order to establish this point conclusively, however, it would be necessary to perform creep and relaxation tests in an environment free from temperature fluctuations and external disturbances. Such facilities were unavailable to the writer, so this point remains unproven.

In some of the creep tests--for example test number C-C-1-7 in Figure A.7--the data points for the earlier part

of the tests do not fit the theoretical curve that describes the latter part of the test. Although these points are very sensitive to the value chosen for U_o, this factor alone cannot account for the magnitude of the deviation in every case. It appears that, in some cases, the sample behaved differently during the earlier stages of creep.

4.3 Interpretation of Results

As is expected, the parameters are not constant for a single test specimen, but vary with the stress level. A close examination of the variation of the parameters reveals significant information about the behavior of the clay particle structure under load. Certain combinations of these parameters have particular physical significance and are compiled in Table 4.1 for all tests.

The cyclic creep test illustrate, especially well, the changes take place in the particle network during deformation. Table 4.2 summarizes the trends observed in the quantities $\frac{k_1}{k_1+k_2}$, α and β during two loading cycles. The variations in the model parameters are now considered in detail.

4.3.1 The Spring "Constants"

The absolute values of the spring constants k_1 and k_2 have little physical significance because there is no way of knowing how the resistance of these elements is developed in terms of the particle structure. The quantity $\frac{k_1}{k_1+k_2}$ is of interest, however, since it represents the portion of the

TABLE 4.1 Summary of Results

Sample	Load Increment	Load Cycle	$D_{initial}$ (kg/cm^2)	D_{final} (kg/cm^2)	ΔD (kg/cm^2)	k_1 (kg/cm^2)	k_2 (kg/cm^2)	$\frac{k_1}{k_1+k_2}$	α (cm^2/kg)	β (10^{-7}min^{-1})	$\alpha\beta$ Method 1 (10^{-6}cm^2/kg min)	$\alpha\beta$ Method 2 (10^{-6}cm^2/kg min)	Figure
C-C-1	1	1	0.000	0.500	+0.500	7660	154	0.983	21.5	1.895	4.08	6.12	A.1
"	2	"	0.500	0.765	+0.265	559	65.3	0.895	28.8	1.503	4.33	8.04	A.2
"	3	"	0.765	0.999	+0.234	1093	19.15	0.982	21.3	3.85	8.20	9.30	A.3
"	4	"	0.999	1.240	+0.241	482	10.3	0.979	20.8	13.24	27.6	29.8	A.4
"	5	"	1.240	1.490	+0.250	606	7.43	0.988	13.84	19.48	26.9	28.4	A.5
"	6	"	1.490	1.708	+0.218	283	5.70	0.982	22.5	15.95	35.8	33.9	A.6
"	7	"	1.708	1.890	+0.182	248	1.08	0.995	50.9	41.6	212	160.0	A.7
"	8	"	1.890	1.523	-0.367	259	431	0.375	----	-----	-----	-----	---
"	9	"	1.523	1.112	-0.411	406	368	0.525	90.6	3.69	33.4	-----	A.8
"	10	"	1.112	0.700	-0.412	320	164	0.661	48.4	11.91	57.7	68.1	A.9
"	11	"	0.700	0.457	-0.243	307	75.7	0.803	62.8	5.23	32.9	39.7	A.10
"	12	"	0.457	0.219	-0.240	335	42.3	0.888	45.6	4.85	22.1	33.5	A.11
"	13	1	0.219	0.000	-0.219	319	24.1	0.930	43.7	2.43	10.61	16.1	A.12
"	14	2	0.000	0.316	+0.316	94.3	330	0.222	----	----	-----	----	----
"	15	"	0.316	0.727	+0.411	196	127	0.607	33.5	7.00	23.5	26.6	A.13
"	16	"	0.727	1.142	+0.415	334	106	0.760	31.0	6.66	20.7	20.6	A.14
"	17	"	1.142	1.552	+0.410	235	65.3	0.783	35.0	2.80	9.81	13.6	A.15
"	18	"	1.552	1.140	-0.412	431	0.00	0.000	----	----	-----	----	----
"	19	"	1.140	0.726	-0.414	134	299	0.309	125.6	5.20	65.3	----	A.16
"	20	"	0.726	0.315	-0.411	179	136	0.568	48.0	5.13	24.6	37.0	A.17
C-C-1	21	2	0.315	0.000	-0.315	334	36.1	0.903	37.0	0.622	2.30	4.02	A.18

TABLE 4.1 (Continued)

Sample	Load Increment	Load Cycle	$D_{initial}$ (kg/cm^2)	D_{final} (kg/cm^2)	ΔD (kg/cm^2)	k_1 (kg/cm^2)	k_2 (kg/cm^2)	$\frac{k_1}{k_1+k_2}$	α (cm^2/kg)	β (10^{-7} min^{-1})	$\alpha\beta$ Method 1 (10^{-6} cm^2/kg min)	$\alpha\beta$ Method 2 (10^{-6} cm^2/kg min)	Figure
C-C-7	1	1	0.000	0.987	+0.987	516	23.2	0.957	13.96	61.5	85.9	30.1	A.19
F-C-1	3	"	0.749	0.994	+0.245	238	14.6	0.941	35.9	4.48	16.10	21.4	A.20
F-C-2	2	"	0.250	0.500	+0.250	211	75.3	0.737	37.1	3.24	12.02	16.1	A.21
"	3	1	0.500	0.747	+0.247	193	30.6	0.903	50.3	8.88	44.7	50.4	A.22
"	7	2	0.000	0.250	+0.250	125	108	0.537	98.3	16.85	165.8	215	A.23
"	8	"	0.250	0.499	+0.249	75.3	61.3	0.551	95.9	11.28	108.1	91.2	A.24
"	9	"	0.498	0.746	+0.248	137	41.4	0.768	69.0	4.55	31.4	58.0	A.25
"	12	2	0.249	0.000	-0.249	68.0	38.5	0.638	83.0	5.15	42.7	67.2	A.26
"	14	3	0.249	0.498	+0.249	137	66.3	0.673	40.6	9.18	37.3	45.2	A.27
"	15	"	0.498	0.746	+0.248	168	77.7	0.713	63.4	12.53	79.5	106.5	A.28
"	16	"	0.746	0.990	+0.244	88.7	7.90	0.918	50.1	18.31	91.9	122.4	A.29
"	19	"	0.492	0.247	-0.245	186	47.0	0.799	80.8	5.49	44.4	39.9	A.30
"	20	3	0.247	0.000	-0.247	160	15.9	0.907	93.8	0.286	2.68	18.3	A.31
F-C-2	33	4	0.952	1.152	+0.200	104	3.40	0.970	35.2	150	528	615	A.32
F-C-8	1	1	0.000	0.499	+0.499	267	88.3	0.751	26.0	14.45	37.6	45.2	A.33
"	2	1	0.499	0.755	+0.256	277	18.9	0.928	47.3	1.926	9.12	17.01	A.34
"	7	2	0.517	0.770	+0.253	187	36.7	0.800	41.0	3.86	15.83	24.5	A.35
F-C-8	8	2	0.770	1.025	+0.255	240	21.6	0.917	41.7	5.63	23.5	25.3	A.36
F-C-9	1	1	0.000	1.103	+1.103	46.7	8.47	0.848	22.7	5.98	13.59	26.0	A.37

TABLE 4.1 (Continued)

Sample	Load Increment	Load Cycle	$D_{initial}$ (kg/cm^2)	D_{final} (kg/cm^2)	ΔD (kg/cm^2)	k_1 (kg/cm^2)	k_2 (kg/cm^2)	$\frac{k_1}{k_1+k_2}$	α (cm^2/kg)	β (10^{-7} min^{-1})	$\alpha\beta$ Method 1 (10^{-6} cm^2/kg min)	$\alpha\beta$ Method 2 (10^{-6} cm^2/kg min)	Figure
D-C-9	2	1	0.27	0.47	+0.20	884	116	0.883	91.0	0.274	2.50	4.27	A.38
"	3	"	0.47	0.67	+0.20	101.5	31.8	0.763	44.8	0.874	3.92	3.56	A.39
"	4	"	0.67	0.87	+0.20	----------	See Section 4.3.6	----------					**
D-C-9	5	1	0.87	1.07	+0.20	66.0	14.0	0.825	41.4	0.349	1.445	6.51	A.40
DP-C-1	1	1	0.00	0.0838	+0.0838	26.9	0.595	0.978	87.4	13.09	114.3	115.8	A.41
F-R-5	1	--	1.490	1.1075	-0.382	----	-----	-----	38.2	4.03*	15.40*	22.9*	A.42
F-R-6	1	--	1.477	1.135	-0.342	----	-----	-----	38.5	3.66*	14.10*	17.09*	A.43
F-R-8	1	--	1.070	0.522	-0.548	----	-----	-----	22.5	2.22*	5.00*	7.36*	A.44
F-R-8	2	--	1.548	0.893	-0.655	----	-----	-----	24.6	3.90*	9.60*	14.68*	A.45

*Assuming k_1 = 167 kg/cm^2 from creep tests on similar specimens.

**See Figures 4.10 and 4.11.

TABLE 4.2. Variation of Model Parameters during Cyclic Creep Loading

Parameter	Physical Significance	Measured Trend			
		Cycle 1 Loading	Cycle 1 Unloading	Cycle 2 Loading	Cycle 2 Unloading
$\frac{k_1}{k_1 + k_2}$	Equals fraction of applied stress acting to cause flow of interparticle bonds	increase (slight)	increase	increase	increase
α	Inversely proportional to number of flowing bonds per unit area in plane of flow	increase (last load increment only)	decrease	decrease	decrease
β	Inversely proportional to exponential of activation energy; inversely proportional to distance between points of flow perpendicular to direction of stress	increase	decrease	decrease	decrease

total shear stress that initially tends to produce flow. Figure 4.6 shows the variation of $\frac{k_1}{k_1 + k_2}$ with deviator stress level over two complete cycles of loading and unloading. The data from the compacted specimen C-C-1 is chosen for this illustration because of the completeness of the data, but the other specimens show similar trends. Figure 4.6a shows that, throughout first loading on specimen C-C-1, nearly all of the applied stress causes flow at the bonds. According to this trend, the initial bond strength distribution curve must be skewed toward the direction of lower yield strengths, which agrees with the curve shown in Figure 2.5a.

The unloading branch of cycle 1 shows that less than half of the first unloading increment produces flow. For subsequent unloading increments in the first cycle, $\frac{k_1}{k_1 + k_2}$ steadily increases until, for the last increment, nearly all of the stress causes flow. It was also noted that the creep response becomes progressively slower with unloading. These observations indicate that the distribution of yield strengths is more uniform for unloading than for loading in the first cycle. Reference to Figure 2.5c shows that such behavior is predicted by the theory.

Theoretically, if no changes in the properties of the particle structure take place, the distribution of bond yield strengths for reloading should be the same as for first loading. However, according to Figure 4.6c, the behavior of $\frac{k_1}{k_1 + k_2}$ during reloading is intermediate between the cases

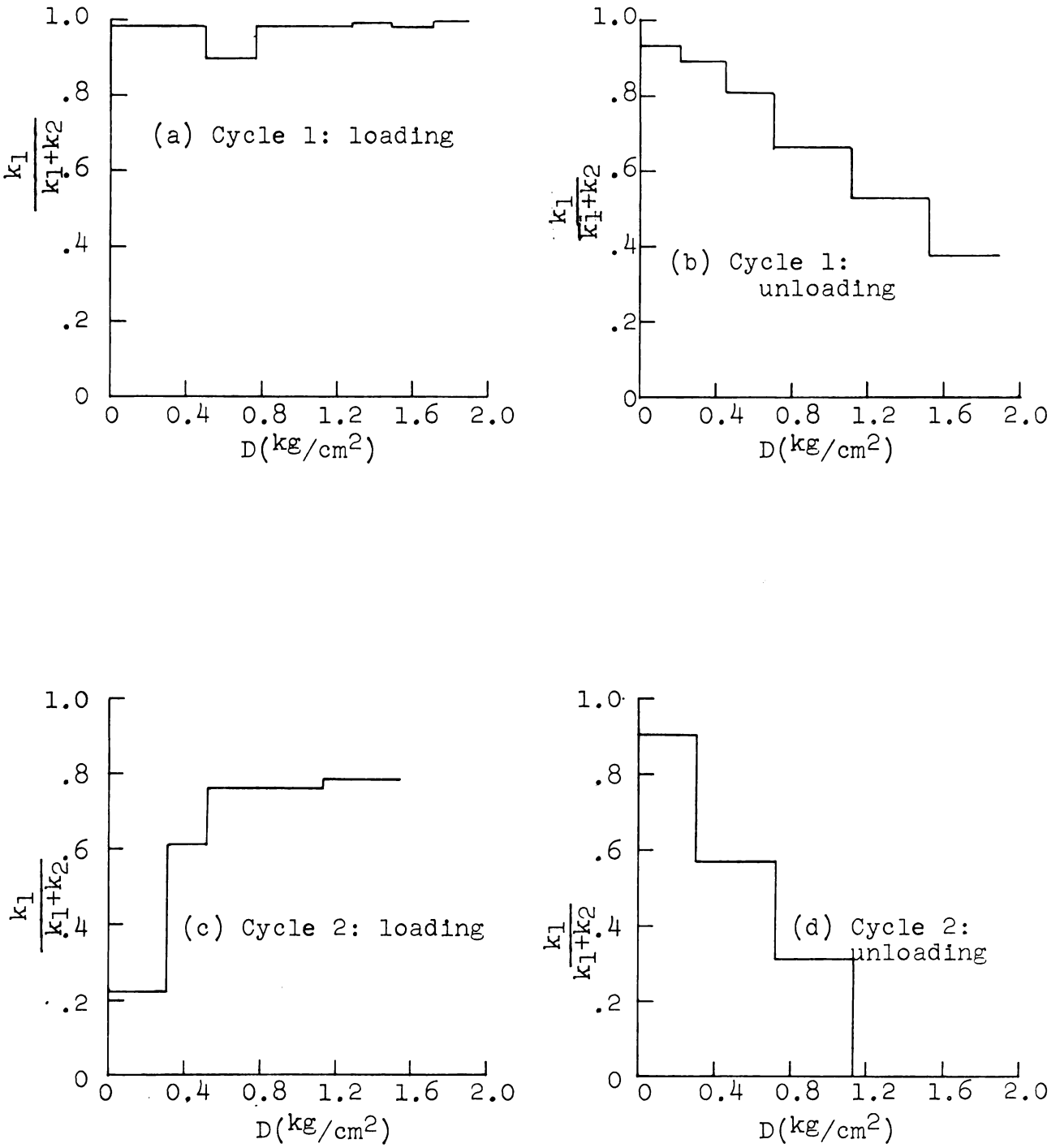

Figure 4.6. Variation in the ratio $\frac{k_1}{k_1+k_2}$ with deviator stress, D, in cyclic creep loading of specimen C-C-1.

of loading and unloading in the first cycle, which means that the yield strength distribution curve for reloading must be flatter than for first loading.

A possible explanation for the change in the distribution of yield strengths after a loading cycle is that some of the particles, in the process of flow, become aligned along potential failure planes; thus reducing the number of bonds in the planes of flow and weakening resistance to deformation along these planes. Wu, Douglas, and Goughnour (1962) observed such particle alignment by means of diffraction studies on thin sections taken from the failure planes of triaxial specimens. Hvorslev (1960) also detected preferred particle orientation by drying triaxial specimens and noting the development of shrinkage cracks.

Furthermore, it is quite likely that some bonds with greater yield strengths could be created as a result of particle interference during the flow process. Lambe (1960), explained that interference can occur when particles become wedged together during deformation. Additional energy is then required to lift the particles over one another so that flow can continue. This would result in a shift in the distribution of yield strengths toward greater strength and tend to flatten the curve.

The increase in $\frac{k_1}{k_1 + k_2}$ for the second unloading is basically the same as that for the first unloading. From the consideration of the variation in $\frac{k_1}{k_1 + k_2}$ over two cycles

of loading, it is possible to sketch, qualitatively, the distribution of bond yield strengths at the beginning of each phase of loading. Figure 4.7 shows distribution curves for the beginning of each loading and unloading which are based on the observed phenomena.

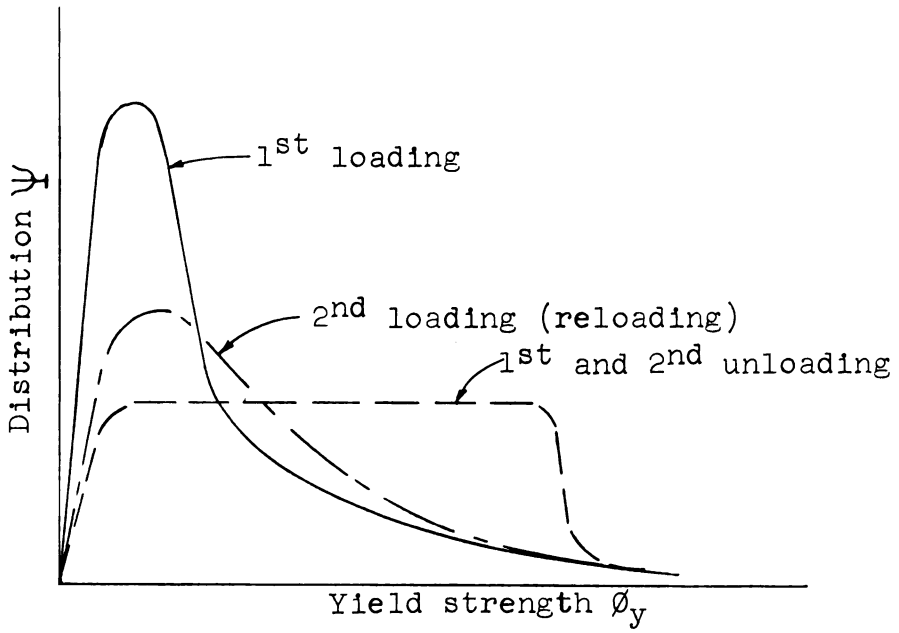

Figure 4.7. Distribution of bond yield strengths with respect to the various phases of cyclic creep loading--constructed from observed trends of $\frac{k_1}{k_1+k_2}$.

4.3.2 The Parameter α

According to Equation 2.7,

$$\alpha = \frac{\lambda}{2\sqrt{kT}}$$

where λ is the distance between equilibrium points on the potential surface in the direction of flow and $\sqrt{}$ is the

number of flowing interparticle bonds per unit area in the plane of flow.

It may be assumed for simplicity that λ , which is a property of the close range interparticle forces and, perhaps, the lattice structure near the particle surface does not change appreciably. Then the factor which controls the value of α , for constant temperature, is ν . Therefore, the variation of α for a given sequence of loading gives some indication of the shape of the yield strength distribution curve and provides a check on the trends observed in $\frac{k_1}{k_1 + k_2}$.

Figure 4.8 shows that α changes but little during the first loading of specimen C-C-1 until the last increment of deviator stress. Since the fraction of the stress carried initially by the flowing bonds ($\frac{k_1}{k_1 + k_2}$) is near unity for all increments, large changes in ν are not expected. Under the last load increment the value of α is approximately doubled, indicating a sudden reduction in the number of flowing bonds in the plane of flow. The axial strain produced by the last increment is more than twice the total strain prior to that increment. Consequently, it is reasonable to assume that the structural changes in the sample during the last increment are substantially greater than for any preceding increment.

It was noted earlier that large strains can produce preferred particle orientation along potential failure planes.

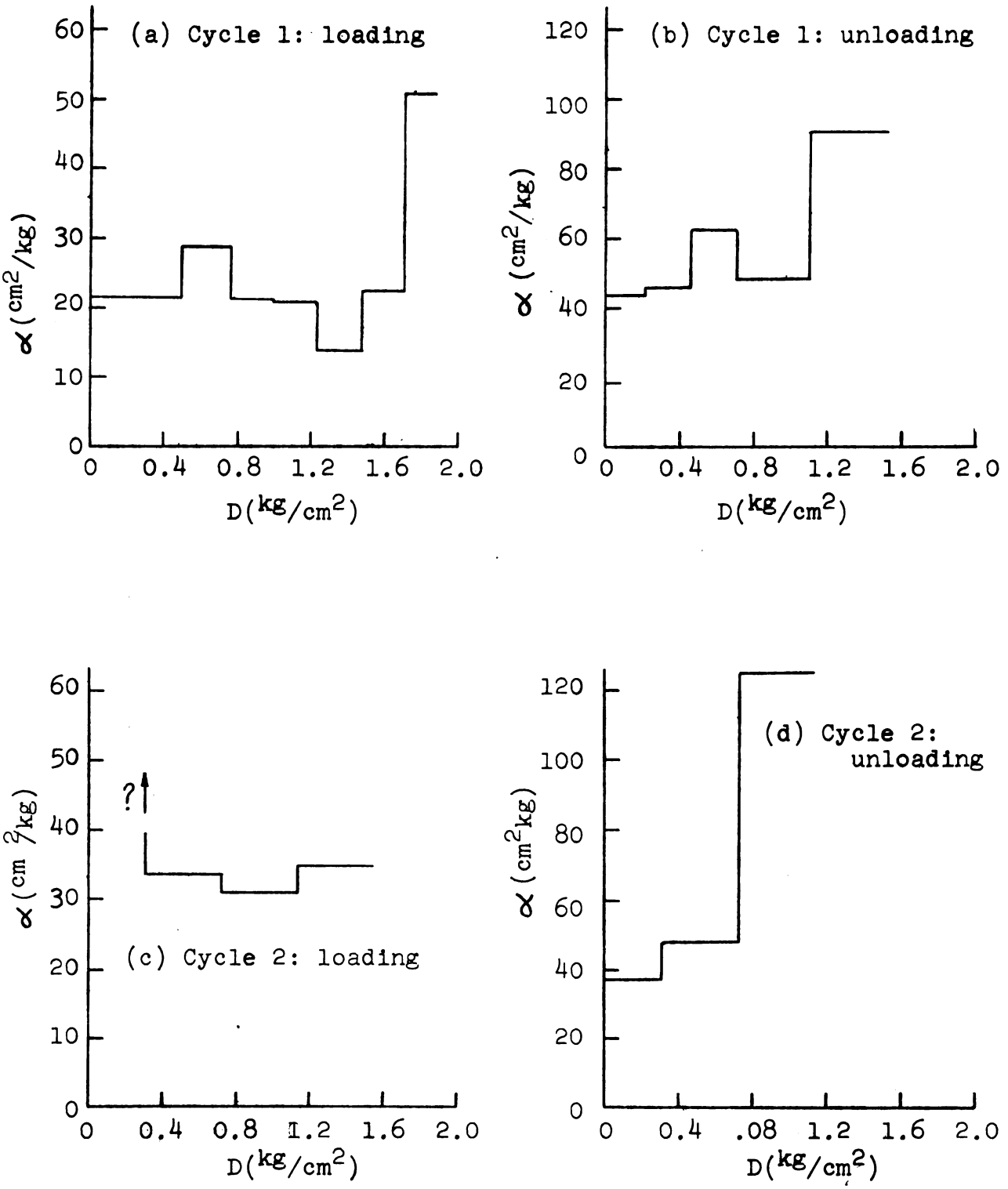

Figure 4.8. Variation of the flow parameter, α, with deviator stress, D, in cyclic creep loading of specimen C-C-1.

As the flat particle surfaces become parallel to one another, fewer interparticle bonds can develop per unit area and, consequently, some of the bonds that are broken cannot reform. If particle reorientation takes place during the last load increment--which seems reasonable in view of the large strains observed--then the increase in α can be attributed to a reduction in the number of bonds in the plane of flow.

During the unloading phase of the first cycle, α decreases so ν must be increasing which agrees with the trends observed in $\frac{k_1}{k_1 + k_2}$. The second loading cycle shows that ν increases with progressive loading and unloading which also corroborates the evidence from $\frac{k_1}{k_1 + k_2}$. In general, the variation in α substantiates the yield strength distribution curves shown in Figure 4.7.

It may be noted in Table 4.1 that the consolidated specimens, which have larger final void ratios than the compacted specimens, give larger values of α, indicating that less bonds flow when the void ratio is larger. The dry creep specimen DP-C-1, which has the highest void ratio of all specimens tested, also gives the largest α value for comparable stages of loading. The implication of this trend is that the number of bonds per unit volume is inversely proportional to the void ratio which verifies the theoretical prediction of Section 2.2.

The calculated values of α provide an excellent opportunity to check the reliability of the hypotheses which

led to the structural model. Recalling that

$$\alpha = \frac{\lambda}{2 \nu kT}$$

and taking $\alpha = 30$ as a representative value, then

$$\frac{\lambda}{\nu} = 2\alpha kT = 2\ (30)\ (1.407 \times 10^{-22})\ (298)$$

$$\frac{\lambda}{\nu} = 2.52 \times 10^{-18}\ \text{cm}^3$$

In specimen C-C-1, the solid weight is 97.5 grams and the specific gravity of the solids, G_s, is 2.70. Therefore the solid volume

$$V_s = \frac{97.5}{2.70} = 36.1\ \text{cm}^3$$

An average illite particle is approximately 0.5 microns in diameter and 100 angstroms in thickness (Scott, 1963), giving an average volume of approximately 2×10^{-15} cm^3. Since the Sault Ste. Marie clay has a clay fraction of 0.60, the total number of clay particles is then,

$$\frac{(36.1)\ (0.60)}{2 \times 10^{-15}} = 1.09 \times 10^{16}\ \text{particles.}$$

The total volume of specimen C-C-1 after consolidation is 63.65 cm^3, so the number of particles per unit volume becomes,

$$\frac{1.09 \times 10^{16}}{63.65} = 1.70 \times 10^{14}\ \text{particles/cm}^3$$

If it is assumed that each particle forms six contacts as suggested by Rosenquist (1960), then the number of bonds per unit area in the plane of flow, μ, is approximately

$$\mu = (6)(1.70 \times 10^{14})(\tfrac{1}{3})(0.5 \times 10^{-4})(0.707)$$

$$\mu = 1.20 \times 10^{10} \text{ bonds/ cm}^2$$

where μ is equal to the number of bonds per unit volume times the distance between points of flow perpendicular to the direction of flow and the particles are assumed to be inclined to the plane of flow at an average angle of 45 degrees. Assuming that 75 per cent of the bonds flow,

$$\lambda = (2.52 \times 10^{-18})(1.20 \times 10^{10})(0.75)$$

$$\lambda = 2.27 \times 10^{-8} \text{ cm} = 2.27 \text{ angstroms}$$

where $\nu = 0.75\,\mu$. It is of interest to note that the distance between adjacent silica tetrahedra in an illite particle is 2.55 anstroms (Grim, 1953). In view of the calculated value of $\lambda = 2.27$ angstroms, it seems reasonable that the interparticle bonds are associated with the lattice structure of the particles.

4.3.3 The Parameter β

The concept that the particle structure possesses a spectrum of yield strengths in its interparticle bonds suggests that as stresses are applied to the structure in increments, the activation energy of flow should increase as stronger bonds are brought into the flow process. From Equation 2.7,

$$\beta = 2\frac{\lambda}{\lambda_1}\quad\frac{kT}{h}\, e^{-\Delta F/RT}$$

so that β should decrease, exponentially, as ΔF increases if λ_1 is constant. Although λ_1 may not be constant, the activiation energy is assumed to dominate changes in β because of the exponential effect of ΔF.

Figure 4.9 shows the variation of β in specimen C-C-1 over two loading cycles. For all except the first loading, β generally follows the expected trend--decreasing as the load is increased for reloading (Figure 4.9c) and decreasing again as the load is removed (Figures 4.9b and 4.9d). Thus, the average yield strength of the bonds that flow increases as loading progresses as a predicted by the yield strength distribution curves in Figure 4.7.

However, for the first loading β increases which is contrary to the expected behavior. This would seem to indicate that the bonds that reform in the flow process are weaker than the original bonds. Such a phenomenon is plausible in light of the evidence of structural changes detected earlier by the consideration of $\frac{k_1}{k_1 + k_2}$ and α .

For example, consider an interparticle bond between two particles meeting at a large angle and forming an edge-to-face contact. The attractive forces between these two particles are large due to the opposite charges of the edge and face, while the repulsive forces are small since the flat surfaces of the two particles are far apart. This type of contact, predominant in a random particle structure, forms a strong bond. On the other hand, two particles

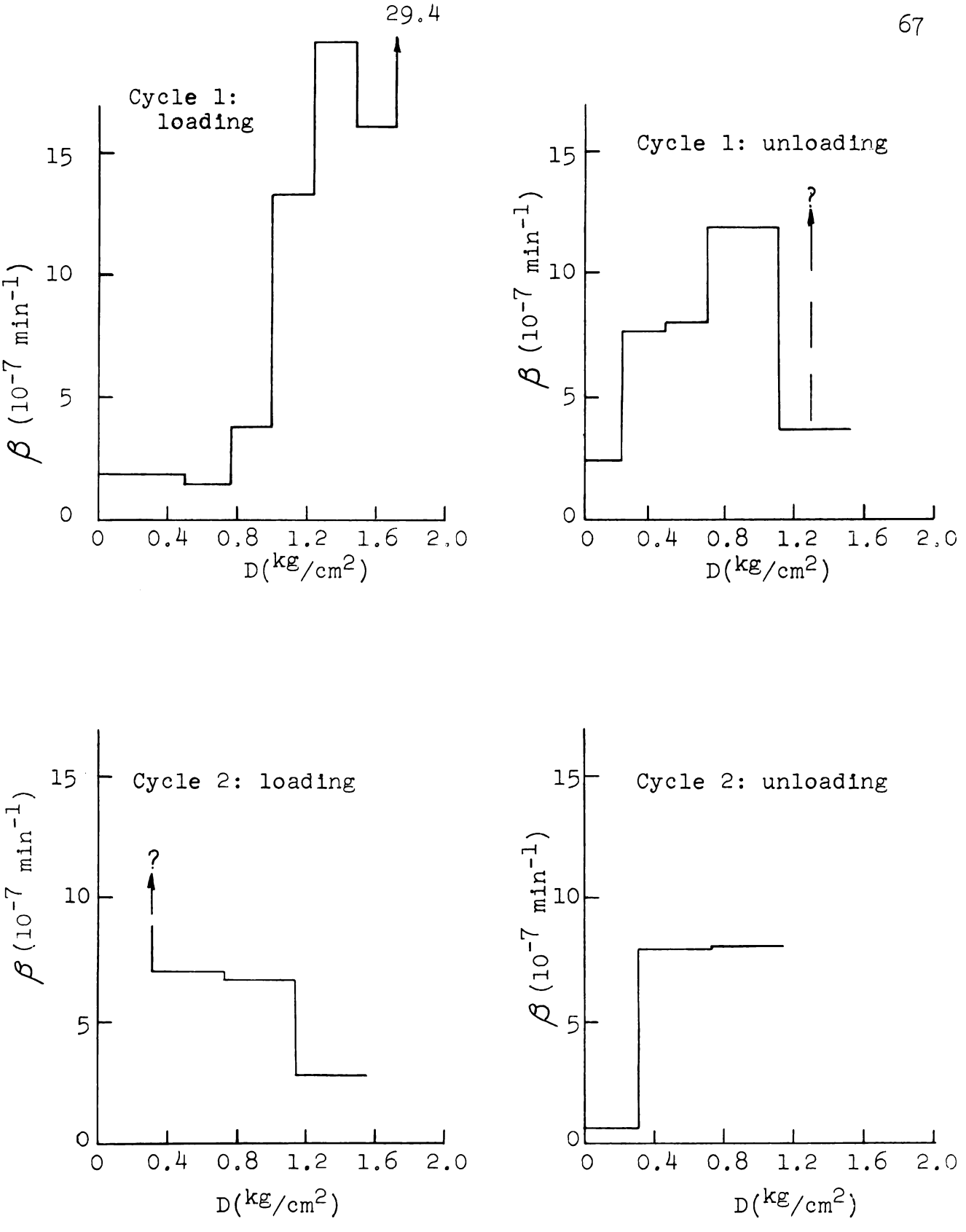

Figure 4.9. Variation in rate parameter β with deviator stress, D, in cyclic creep loading of specimen C-C-1.

meeting at a low angle form a much weaker bond because of the repulsion developed between the flat surfaces as they approach one another.

As the particles become aligned in the planes of flow, the angles between particles forming bonds becomes progressively smaller and thus the bonds may become weaker as described above. ΔF, therefore, decreases and β increases with strain. Experimental evidence for such particle alignment during the first loading has already been cited. The strains produced by subsequent loadings were much smaller so structural changes probably had little effect on ΔF after the first loading.

As seen from Table 4.1, nearly all of the calculated values for β fall within the range $5 - 15 \times 10^{-7}$ min.$^{-1}$ Using $\beta = 10^{-6}$ as a representative value, $\lambda = 2.27$ Å and letting $\lambda_1 = \frac{1}{3} \times 0.5 \times 10^{-4} \times .707 = 1.178 \times 10^{-5}$ cm. as before, the activation energy, ΔF, may now be determined.

Noting that

$$\Delta F = RT \ln \left[2 \frac{\lambda}{\lambda_1} \frac{kT}{h} \left(\frac{1}{\beta}\right) \right]$$

and substituting the values from above, the activation energy is

$$\Delta F = (.001987)(298) \ln \left[2 \frac{(2.27 \times 10^{-8})(1.407 \times 10^{-22})(298)}{(1.178 \times 10^{-5})(10^{-6})(1.125 \times 10^{-34})} \right]$$

$$\Delta F = 24.8 \text{ k cal mole}^{-1}$$

This value represents the mean strength of the interparticle

bonds broken during the shearing process. Since the bond strengths are comprised of a complicated interaction of attractive and repulsive forces between the clay particles, the contribution of the individual bonding and anti-bonding force systems is impossible to assess with the knowledge of the clay-water system presently available.

4.4.4 Creep Test on Dry Clay

It was stated, in connection with the discussion of the clay-water system in Chapter II, that the role of the adsorbed water films in determining the deformational characteristics of clays is of minor importance. This view is based, in part, on an experiment performed by Norton (1952) in which it was shown that a dry clay, when placed in an elastic membrane and the air withdrawn, behaves exactly like a wet plastic clay. It was believed that the conditions of this experiment could be duplicated in the triaxial cell, thus producing a dry clay specimen that could be tested under creep loading.

A specimen of oven-dry powdered clay was obtained using the same technique used in preparing triaxial specimens of dry sand. The details of this technique are described in Chapter III. No moisture was permitted to enter the sample during testing.

Because of the fluffy nature of the dry, powdered clay, compaction in the sample mold was difficult and the resulting specimen has a rather high final void ratio ($e = 1.132$) and,

consequently, is quite weak. It was, however, possible to perform one loading increment on the specimen using a small deviator stress. The results of this test are shown in Figure A.42. It can be seen that the curves for the dry clay take the same form as the saturated clays for creep loading. The calculated values of α and β for the dry clay are also consistent with those obtained for the saturated clays.

The findings of this test indicate that the behavior of the clay particle structure is not affected to any important degree by the presence of adsorbed water films. Norton (1952) suggests that the role of water in causing plasticity in clays consists of forming an air-water boundary around the surface of the wet clay mass, producing surface tension which acts to press the particles together. The plasticity of a wet clay mass is, thus, believed to be a property of the clay particles and not of the water.

4.3.5 Relaxation Tests

It has been demonstrated that the structural model for clays developed in Chapter II provides a good representation of creep behavior. The results of the stress relaxation tests provide an opportunity to check the generality of the model with another type of loading. The agreement between the theoretical and experimental relaxation curves is quite good. The calculated values of β also agree with those obtained in the creep tests (see Table 4.1). It will be

noted in Table 4.1 that the value of k_1 is estimated from creep tests performed on a similar specimen in order to calculate β. This is necessary because the relaxation tests provided no independent means of evaluating the spring "constants."

The values obtained for α in specimen F-R-8 are somewhat smaller than the corresponding values in creep loading on similar specimens. Since the results are obtained from different samples, this discrepancy may simply be due to the unavoidable variation between samples; even though the method of preparation is identical. The other relaxation tests yielded values of α which agree with those obtained in creep loading on similar specimens. In general, the agreement between the results of the relaxation tests and the creep tests seems to support the validity of the structural model.

4.3.6 Temperature Effects

The room temperature was measured by means of a continuously recording temperature gage during the progress of the loading tests. During the winter months, when most of the tests were performed, the room temperature was very well controlled--a maximum temperature variation of about 2°C was average for most tests. During the summer, however, the temperature varied as much as 10°C during a single test. These fluctuations were, for the most part, erratic and of short duration and often produced unreliable results in the

tests. In one instance, however, the room temperature was maintained at a abnormally high level for four days, during which time creep test D-9-4 was in progress.

The creep curve from this test is of interest because it provides an opportunity to calculate a value for the activation energy based on temperature variations. Figure 4.10 shows the creep curve from test no. D-9-4 along with the room temperatures recorded during the test.

Referring to Equation 4.8, it is seen that, for large values of time,

$$\frac{d\dot{U}}{dU} \approx -2H = -\alpha\beta \frac{k_1 k_2}{k_1+k_2} = -\left(\frac{k_1 k_2}{k_1+k_2}\right)\left(\frac{\lambda^2}{\lambda_1 \nu h}\right) c^{-F/RT} \qquad (4.11)$$

Taking logarithms of both sides,

$$\ln\left(\frac{d\dot{U}}{dU}\right) = -\ln S - \frac{\Delta F}{RT} \qquad (4.12)$$

where

$$S = \left(\frac{k_1 k_2}{k_1+k_2}\right)\left(\frac{\lambda^2}{\lambda_1 \nu h}\right)$$

Differentiating with respect to temperature,

$$\frac{d}{dT} \ln\left(\frac{d\dot{U}}{dU}\right) = \frac{\Delta F}{RT^2} \qquad (4.13)$$

Upon integrating Equation 4.13 between the limits T_1 to T_2, the activation energy becomes

$$\Delta F = R\left(\frac{T_1 T_2}{T_1 - T_2}\right) \ln\left[\frac{\left(\frac{d\dot{U}}{dU}\right)_2}{\left(\frac{d\dot{U}}{dU}\right)_1}\right] \qquad (4.14)$$

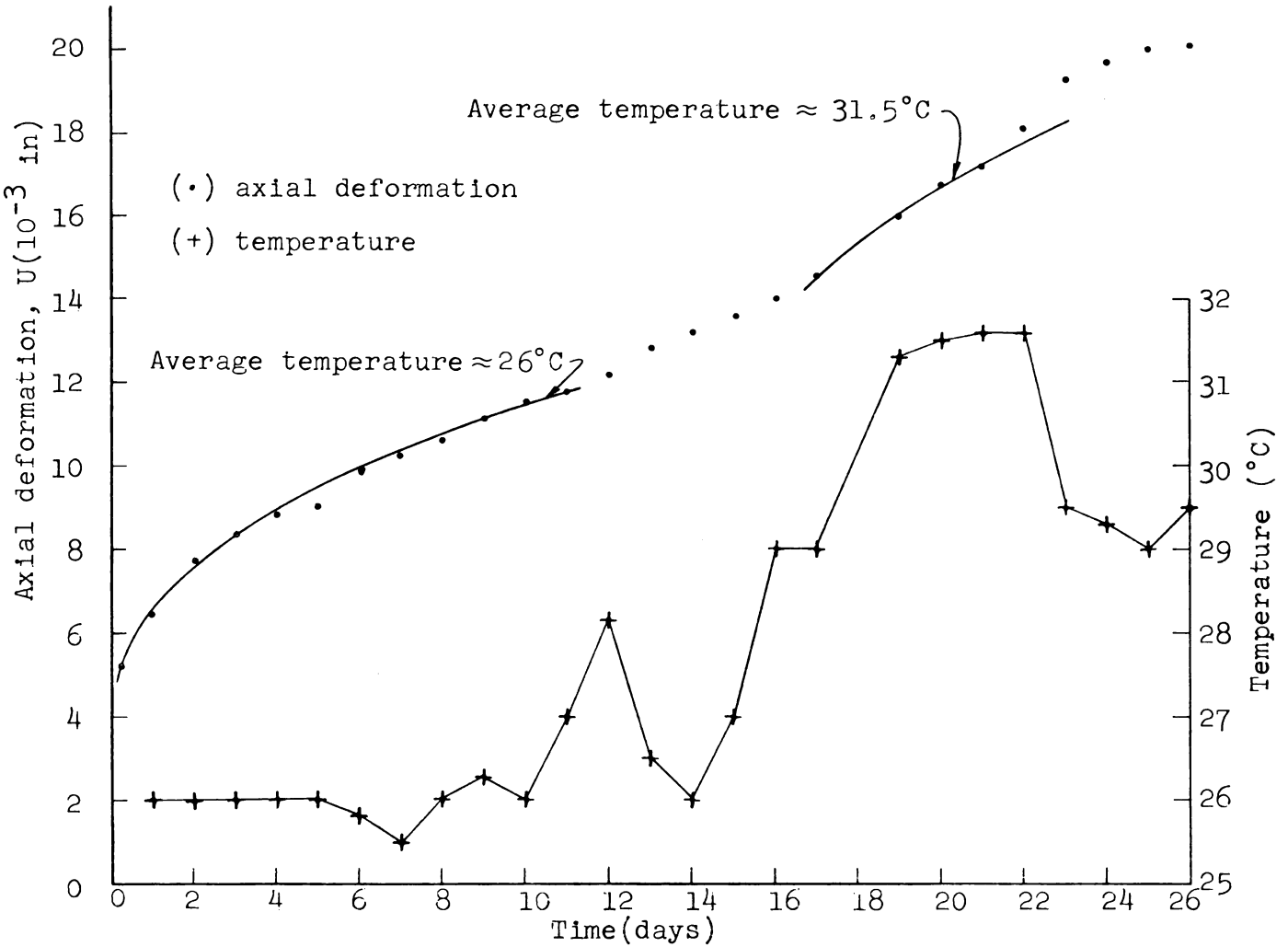

Figure 4.10. Deformation-and temperature-time curves for creep test D-C-9-4, D=0.67-0.87 kg/cm^2.

It may be seen from Equation 4.14 that the calculation of the activiation energy, ΔF, by this method requires the evaluation of $\frac{\dot{dU}}{dU}$ from the creep curve for the temperatures T_1 and T_2. In Figure 4.11, $\frac{\dot{dU}}{dU}$ is determined for the temperatures $T_1 = 26°C$ and $T_2 = 31.5°C$. The segments of the creep curve used in this determination are shown in Figure 4.10.

Substituting the appropriate values into Equation 4.14, the activation energy, ΔF, becomes

$$\Delta F = (.001987)\left(\frac{299 \times 304.5}{5.5}\right) \ln \left(\frac{1.35 \times 10^{-3}}{.663 \times 10^{-3}}\right)$$

$$\Delta F = 23.5 \text{ k cal mole}^{-1}$$

This value of ΔF agrees quite well with that found by another method in section 4.3.3 and adds further evidence in support of the rate theory approach.

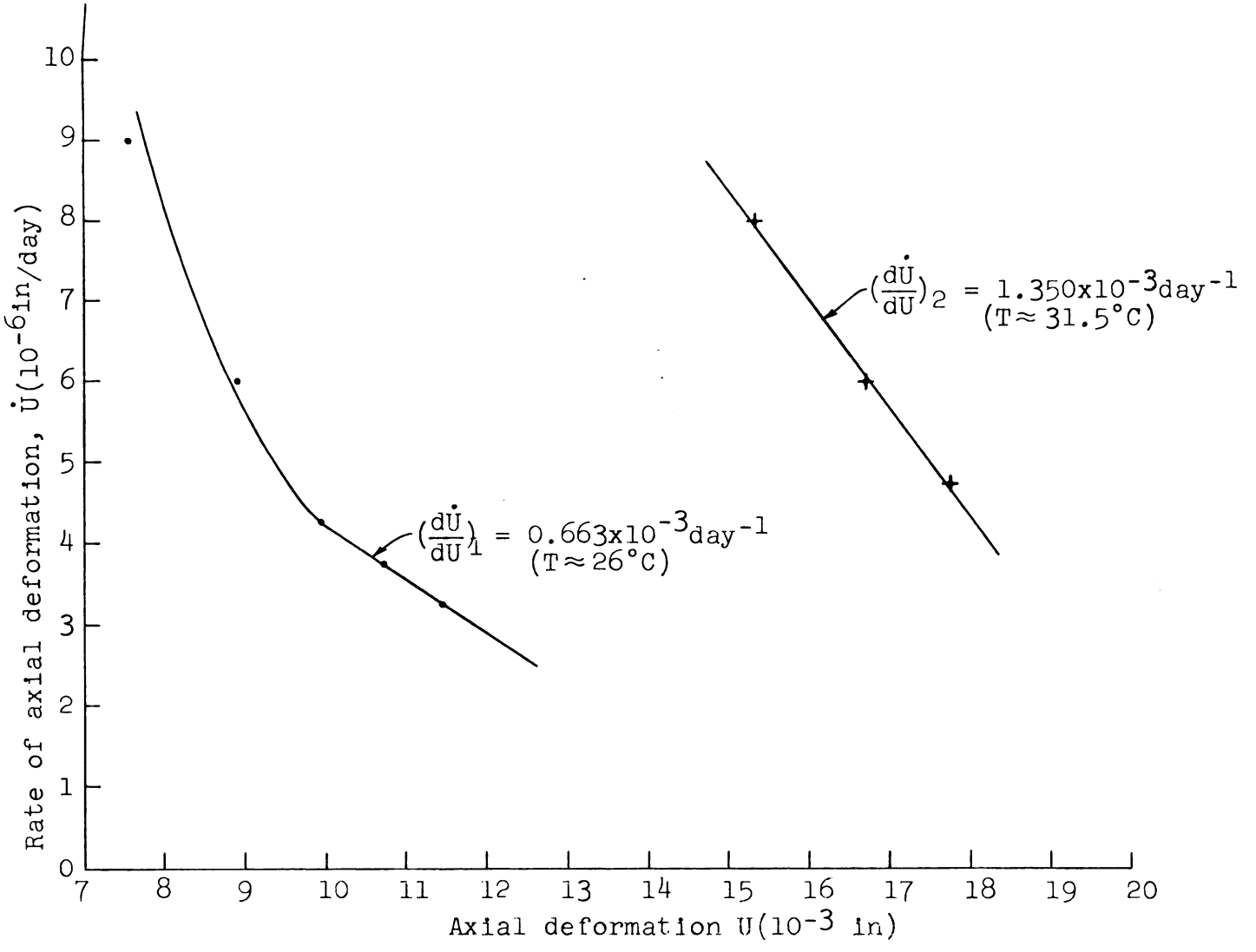

Figure 4.11. Rate of deformation - deformation relationships for two different temperatures in creep test D-C-9-4; D=0.67-0.87 kg/cm^2.

CHAPTER V

CONCLUSION

The deformation of clays is studied from the point-of-view of the particle structure. This consideration leads to the conclusion that processes taking place at the particle level during deformation can be treated by the methods of rate theory. Using the flow relationship derived from the rate theory treatment, the concept of a spectrum of bond yield strengths is developed. According to this concept, some of the bonds in the particle structure flow under a given stress increment while others remain intact by virtue of their greater yield strength. It is shown that the theoretical concepts presented could be simulated by a simple structural model which agrees with the observed deformational properties of clays.

The results of the experimental program show that the behavior of the clays tested agrees well with that predicted by the model for the test conditions employed. The loading conditions are quite varied with specimens being tested under single creep loads, incremental creep loads, cyclic creep loading and stress relaxation. In nearly every case, good agreement is found between the theoretical and experimental results. The quality of agreement achieved tends to substantiate the validity of the rate process approach to

deformations at the particle level. For further investigations along these lines, other loading conditions should be employed; e.g., constant strain rate tests at different rates of strain would be useful, as would experiments with controlled temperature variations.

The creep test performed on a dry powdered clay sample shows that the behavior of the dry clay, in creep, is essentially the same as the saturated clays. This result lends support to the suggestion by Tan (1959) and others (Leonards and Girault, 1961; and Norton, 1952) that the adsorbed water films on the particles are not the prime cause of viscous flow in clays. Additional tests on dry clays under various loading conditions are needed; such tests could provide valuable information on the nature of the interparticle bonds.

The calculated values of the model parameters show considerable variation. In Figures 4.6, 4.8, and 4.9, attention is focused on the variation of these parameters through two complete loading-unloading cycles. From the trends observed in the quantity $\frac{k_1}{k_1 + k_2}$, it is possible to sketch, qualitatively, the distribution of bond yield strengths for the various stages of loading. The variations in α and β agree well with the distribution curves shown in Figure 4.7 with the exception of β during the first loading stage.

During the first loading, it is believed that the yield strength distribution is affected by the breakdown of the

original particle network as the particles become aligned along potential failure surfaces. The increased alignment along the slip plane is known to be accompanied by a tendency toward volume reduction in the potential failure zones. The calculated variation in the model parameters corroborates this view and agrees with the experimental findings of other workers (Wu, Douglas, and Goughnour, 1962; and Whitman, 1960). The increase in the parameter β during first loading also indicates that the interparticle bonds become weaker as deformation proceeds. This phenomenon is explained in terms of the changing particle geometry from a random arrangement toward parallelism. It is noted that the bonds should become weaker due to the build-up of Coulomb repulsive forces, as the flat particle surfaces come closer together.

Subsequent loading cycles show less structural change than first loading as would be expected. The problem of structural changes accompanying deformation needs further investigation. With the recent development of the electron microscope, such studies are now feasible and would contribute much to the understanding of clay deformations at the particle level.

The measured parameter α provides a means to check the values of ν and λ for the clay particle network. The experimental values of α are found to be entirely consistent with the dimensions of the clay particles and particle geometry.

From the measured values of the parameter β, a representative value for the activation energy, ΔF, is calculated. The value is in agreement with ΔF calculated from temperature effects. It is noted that present knowledge of the clay-water system is insufficient to enable ΔF to be interpreted in terms of interparticle forces. The theoretical consideration of the bonding forces between particles provides a promising area for further investigations.

BIBLIOGRAPHY

Anderson, D. M. and Low, P. F. "The Density of Water Adsorbed by Lithium-, Sodium-, and Potassium-Bentonite," Soil Science Society of America Proceedings, vol. 22, 1958, pp. 99-103.

Bowden, F. P. and Tabor, D. Friction and Lubrication of Solids, Clarendon Press, Oxford, 1954.

Burwell, J. T. and Rabinowicz, E. "The Nature of the Coefficient of Friction," Journal of Applied Physics, vol. 24, no. 2, 1953, pp. 136-139.

Casagrande, A. and Wilson, S. D. "Effect of Rate of Loading on the Strength of Clays and Shales at Constant Water Content," Geotechnique, vol. 2, 1950, pp. 251-263.

Christensen, R. W. "Structure and Identification of Clay Soils." Unpublished laboratory report, Soil Science 945, Michigan State University, 1963.

Eyring, H. and Halsey, G. "The Mechanical Properties of Textiles--The Simple Non-Newtonian Model," High Polymer Physics--A Symposium, 1948, pp. 61-116.

Geuze, E. C. W. A. and Tan, T. K. "The Mechanical Behavior of Clays," Proceedings of the Second International Congress on Rheology, 1953, pp. 247-259.

Glasstone, S., Laidler, K. J., and Eyring, H. The Theory of Rate Processes, McGraw-Hill Book Company, Inc., New York, 1941.

Grim, R. E. Clay Mineralogy, McGraw-Hill Book Company, Inc., New York, 1953.

Horn, H. M. and Deere, D. U. "Frictional Characteristics of Minerals," Geotechnique, vol. 12, no. 4, December, 1962, pp. 319-335.

Houwink, R. Elasticity, Plasticity and Structure of Matter, Cambridge University Press, Cambridge, England, 1937.

Hvorslev, M. J. "Physical Components of the Shear Strength of Saturated Clays," American Society of Civil Engineers Research Conference on Shear Strength of Cohesive Soils, June, 1960, pp. 169-273.

Iler, R. K. The Colloid Chemistry of Silica and Silicates, Cornell University Press, Ithaca, New York, 1955.

Lambe, T. W. "A Mechanistic Picture of Shear Strength in Clay," American Society of Civil Engineers Research Conference on Shear Strength of Cohesive Soils, 1960, pp. 555-580.

Leonards, G. A. and Girault, P. "A Study of the One-Dimensional Consolidation Test," Proceedings of the Fifth International Conference on Soil Mechanics and Foundation Engineering, vol. 1, 1961, pp. 213-218.

Lo, K. Y. "Stress-Strain Relationship and Pore Water Pressure Characteristics of a Normally Consolidated Clay," Proceedings of the Fifth International Conference on Soil Mechanics and Foundation Engineering, vol. 1, 1961, pp. 219-224.

Low, P. F. "Viscosity of Water in Clay Systems," Proceedings of the Eighth National Conference on Clays and Clay Minerals, 1960, pp. 170-182.

Martin, R. T. "Water Vapor Sorption on Kaolinite: Entropy of Adsorption," Proceedings of the Eighth National Conference on Clays and Clay Minerals, 1960, pp. 102-114.

Michaels, A. S. "Discussion: Physico-Chemical Properties of Soils: Soil Water Systems," Proceedings of American Society of Civil Engineers, Soil Mechanics and Foundations Division, vol. 85, SM 2, April, 1959, pp. 91-102.

Mitchell, J. K. "The Fabric of Natural Clays and Its Relation to Engineering Properties," Proceedings, Highway Research Board, vol. 35, 1956, pp. 693-713.

Moum, J. and Rosenquist, I. T. The Mechanical Properties of Montmorillonitic and Illitic Clays Related to the Electrolytes of the Pore Water, Norwegian Geotechnical Institute Publication, No. 37, Oslo, 1960.

Murayama, S. and Shibata, T. On the Rheological Characters of Clay, Diaster Prevention Research Institute, Bulletin No. 26, Kyoto, Japan, October, 1958.

Norton, F. H. Elements of Ceramics, Addison-Wesley Press, Inc., Cambridge, Massachusetts, 1952.

Rosenquist, I. T. "Physico-Chemical Properties of Soils: Soil Water Systems," Proceedings of American Society of

Civil Engineers, Soil Mechanics and Foundations Division, April, 1959, pp. 31-53.

Schmertmann, J. H., and Osterberg, J. O. "An Experimental Study of the Development of Cohesion and Friction with Axial Strain in Saturated Cohesive Soils," American Society of Civil Engineers Research Conference on Shear Strength of Cohesive Soils, 1960, pp. 643-694.

Scott, R. F. Principles of Soil Mechanics, Addison-Wesley Publishing Company, Inc., Reading, Massachusetts, 1963.

Tan, T. K. (Discussion), Proceedings of the Third International Conference on Soil Mechanics and Foundation Engineering, vol. 3, 1953, p. 129.

Tan, T. K. "Structure Mechanics of Clays," Scientia Sinica, vol. 8, no. 1, 1959, pp. 83-97.

Terzaghi, K., and Peck, R. B. Soil Mechanics in Engineering Practice, John Wiley and Sons, Inc., New York, 1948.

Tobolsky, A. V. and Andrews, R. D. "Systems Manifesting Superposed Elastic and Viscous Behavior," Journal of Chemical Physics, vol. 13, no. 1, January, 1945, pp. 3-27.

Tobolsky, A. V., Powell, R. E., and Eyring, H. "Elastic-Viscous Properties of Matter," The Chemistry of Large Molecules, 1943, pp. 125-190.

Whitman, R. V. "Some Considerations and Data Regarding the Shear Strength of Clays," American Society of Civil Engineers Research Conference on Shear Strength of Cohesive Soils, June, 1960, pp. 581-614.

Wu, T. H., Douglas, A. G., and Goughnour, R. D. "Friction and Cohesion of Saturated Clays," Proceedings of the American Society of Civil Engineers, Soil Mechanics and Foundations Division, June, 1962, pp. 1-32.

APPENDIX

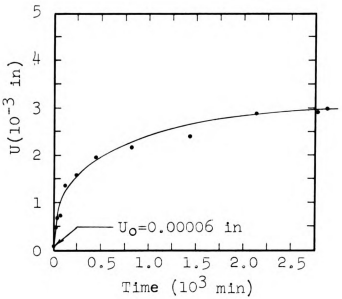

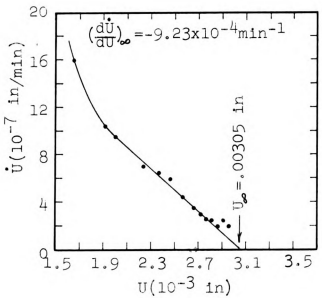

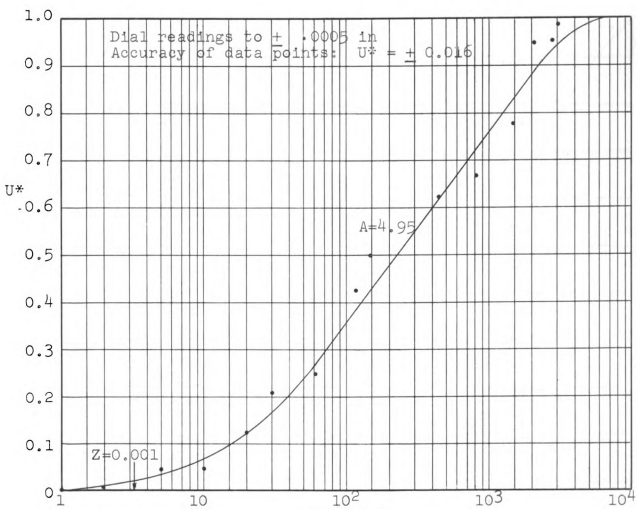

Figure A.1. Creep Curves for C-C-1-1; D=0-0.500$^{kg}/_{cm^2}$

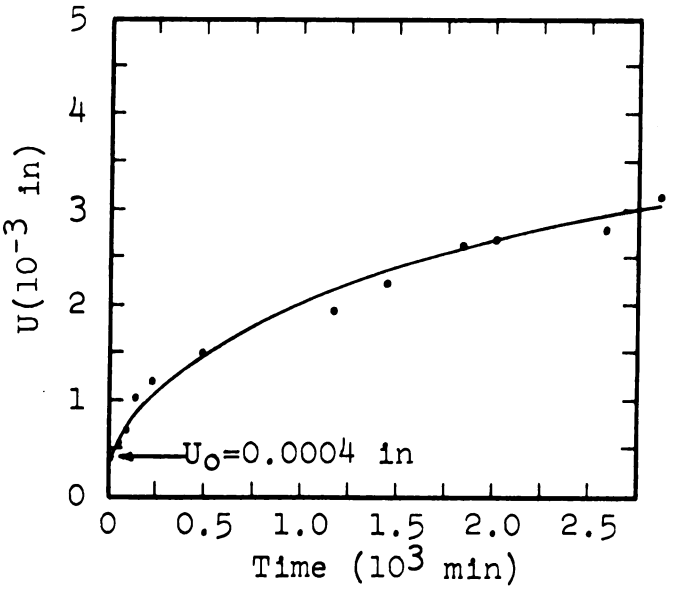

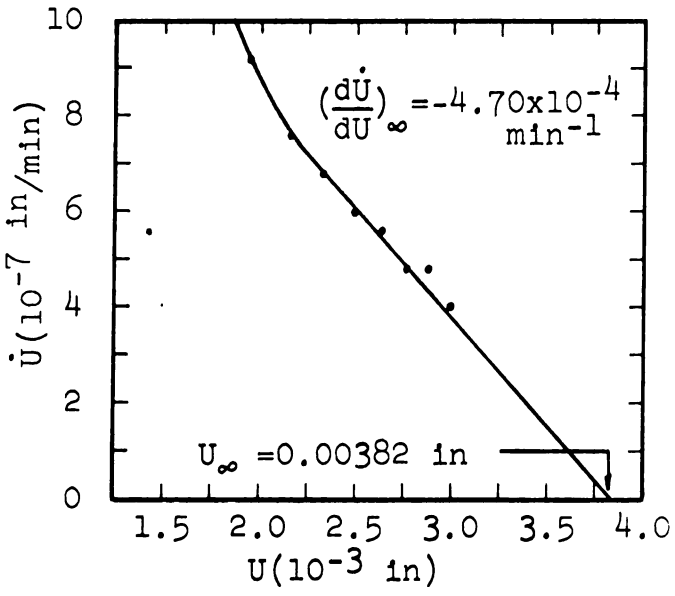

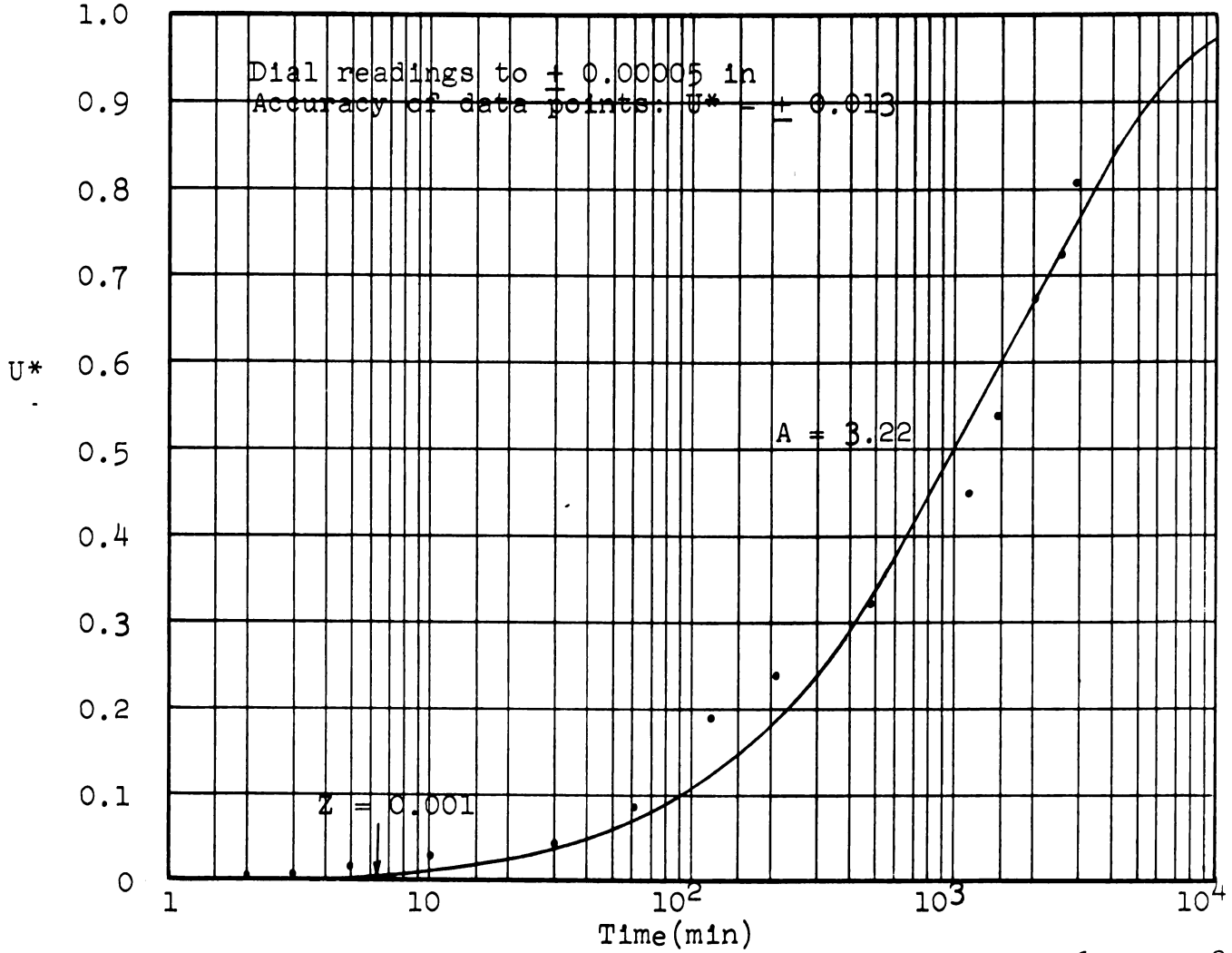

Figure A.2. Creep Curves for C-C-1-2; D = 0.500-0.765 kg/cm^2

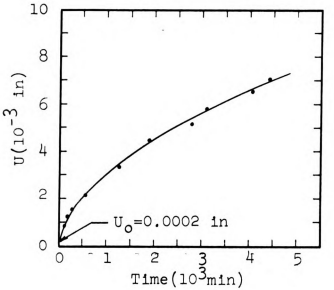

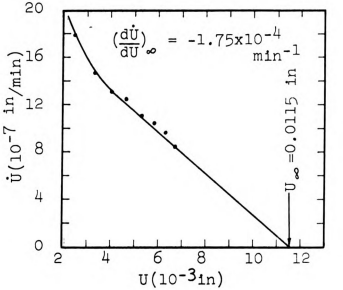

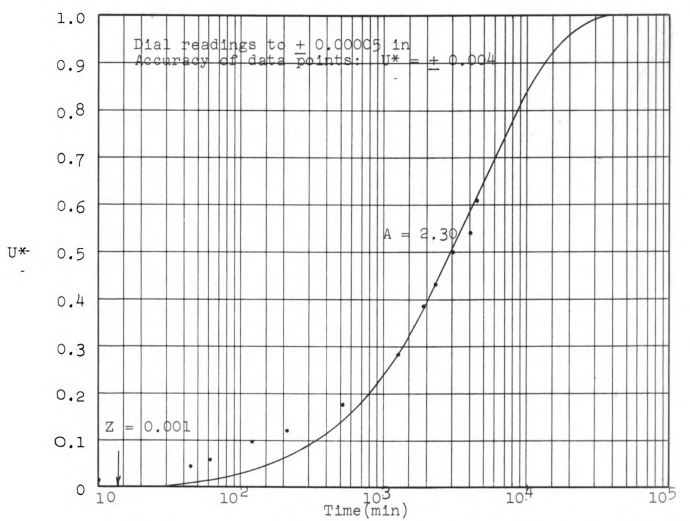

Figure A.3. Creep Curves for C-C-1-3; D = 0.765-0.999 kg/cm^2

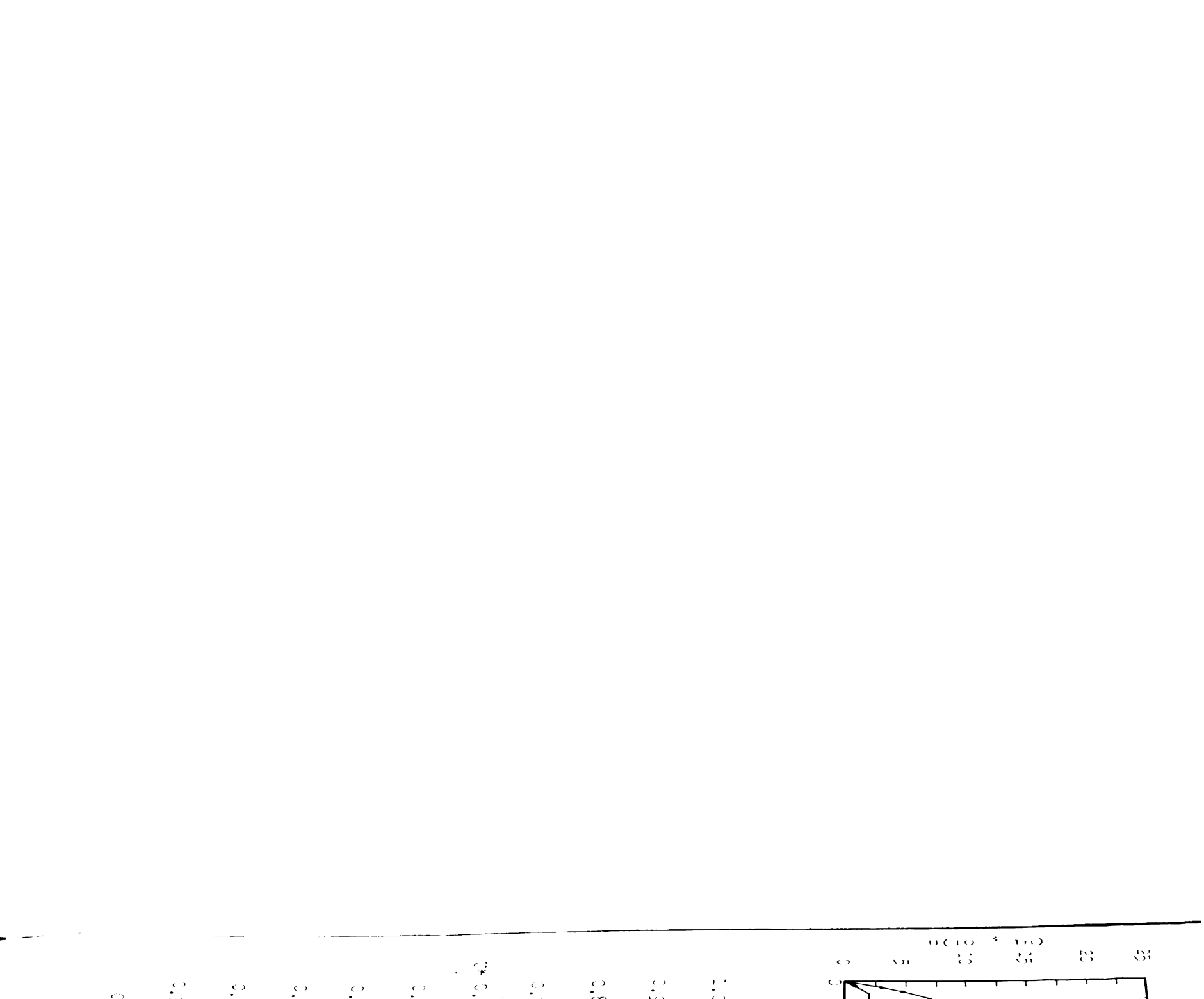

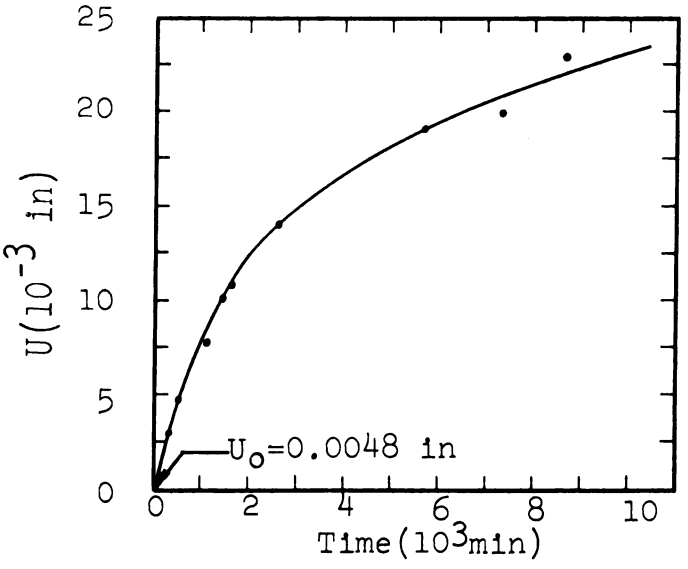

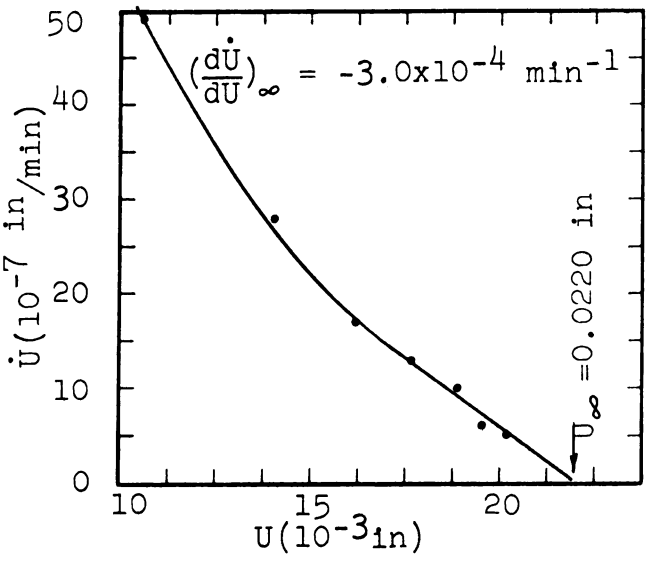

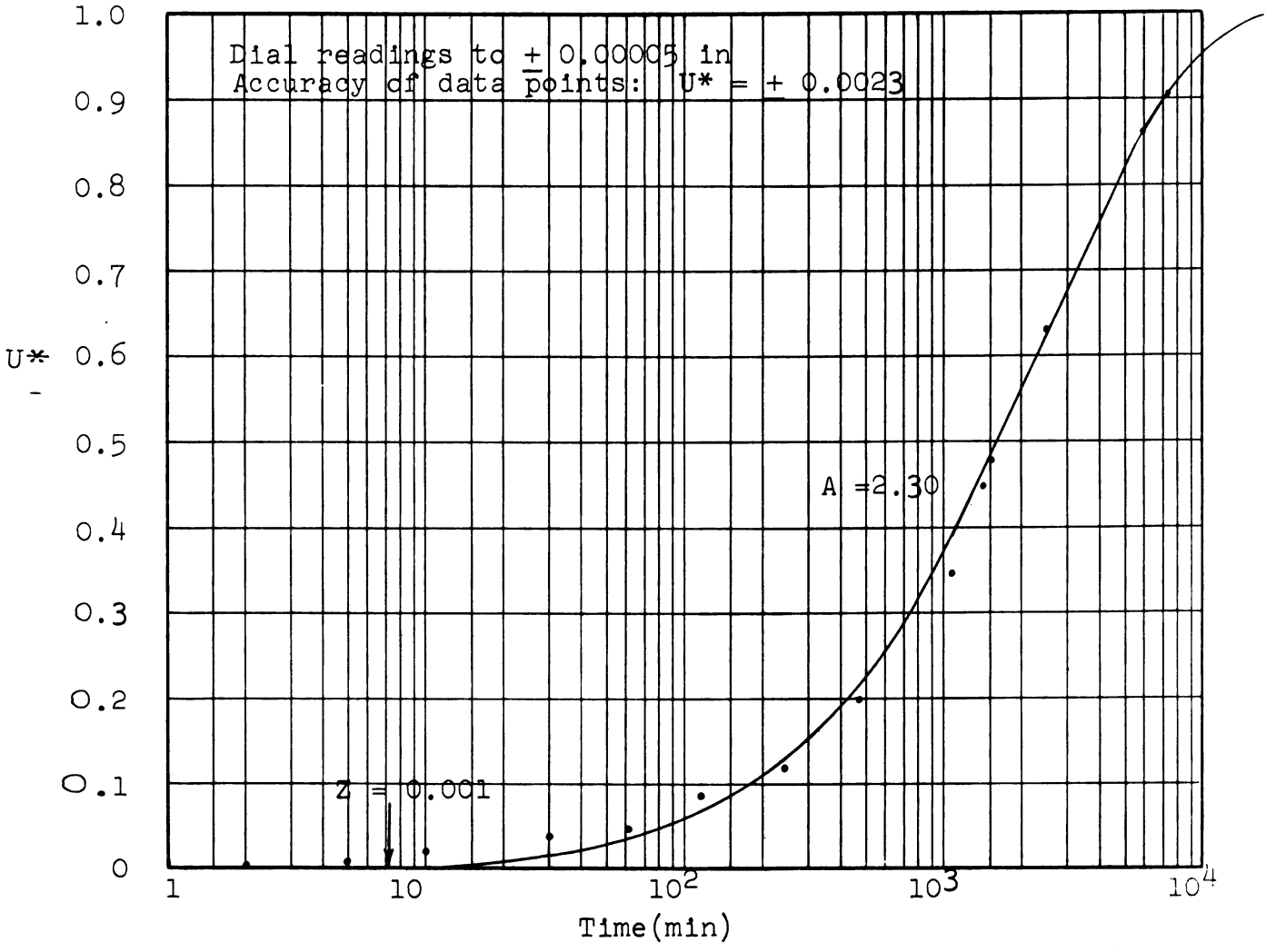

Figure A.4. Creep Curves for C-C-1-4; D = 0.999-1.240 $^{kg}/_{cm^2}$

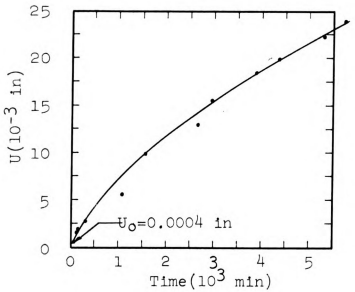

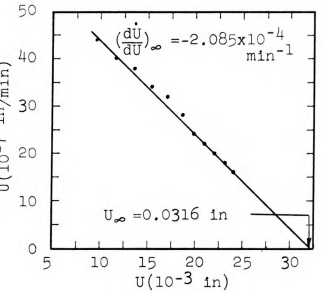

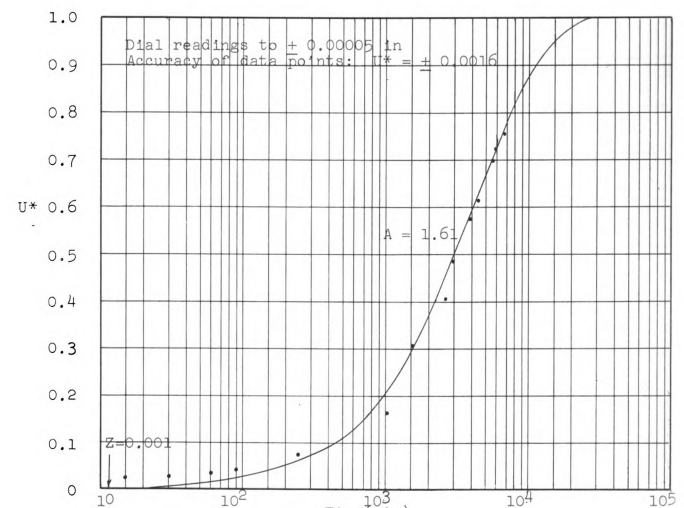

Figure A.5. Creep Curves for C-C-1-5; D=1.240-1.490 kg/cm^2

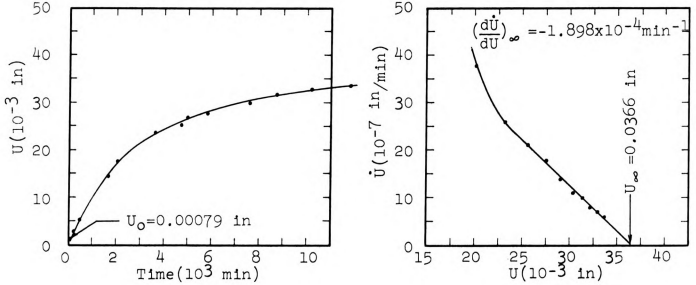

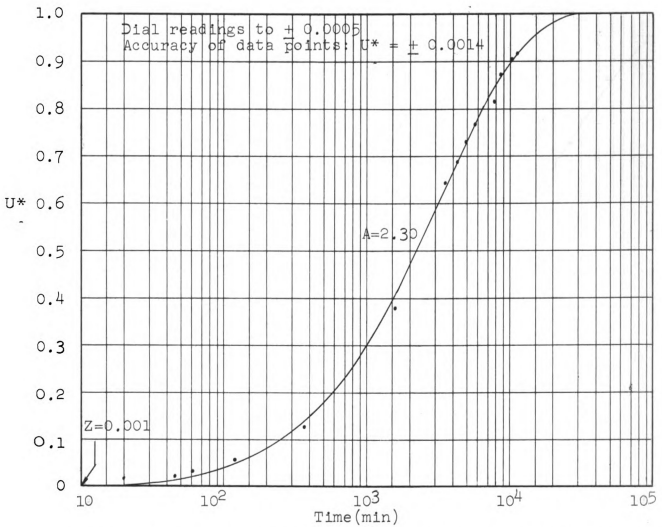

Figure A.6. Creep Curves for C-C-1-6; D = 1.490-1.708 kg/cm^2

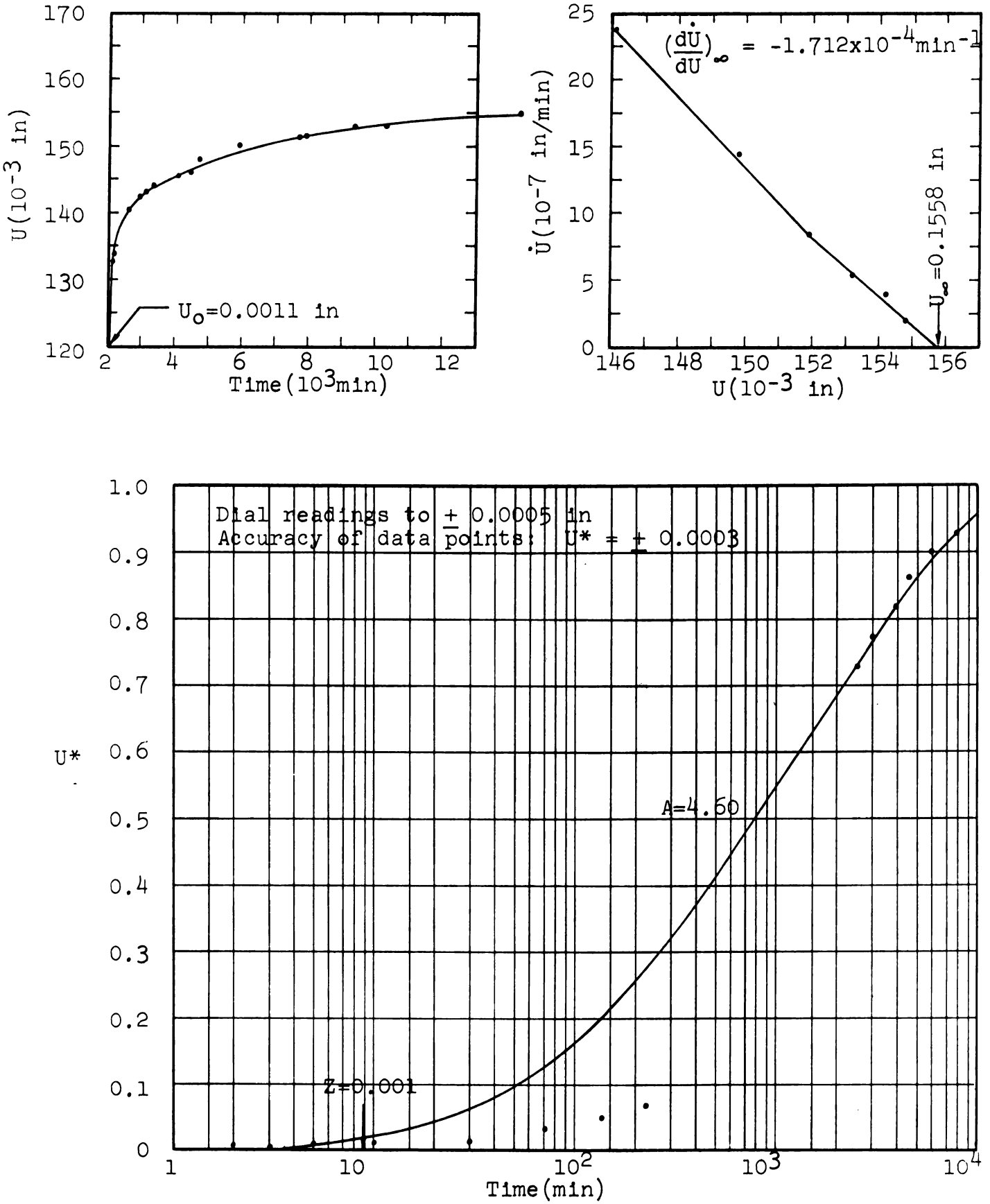

Figure A.7. Creep Curves for C-C-1-7; D = 1.708-1.890 kg/cm^2

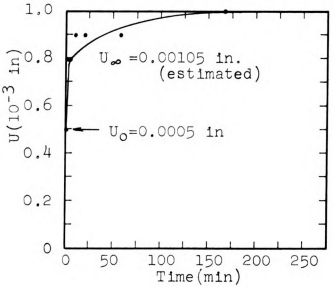

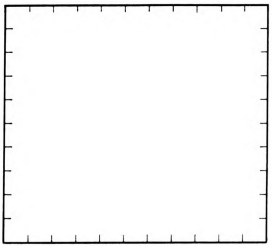

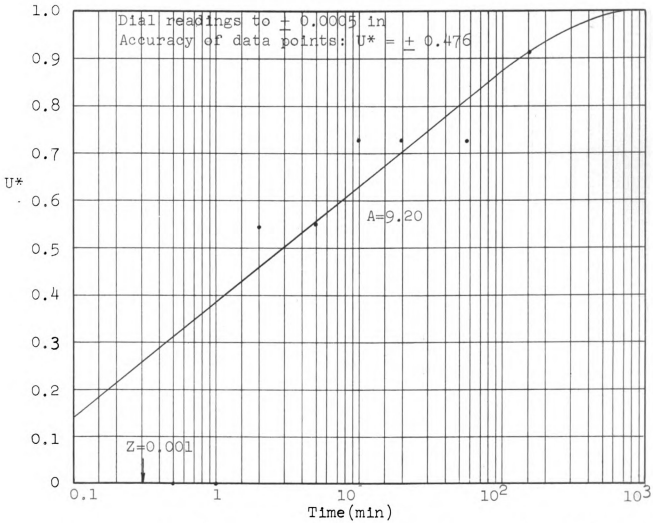

Figure A.8. Creep Curves for C-C-1-9; D = 1.523-1.112 kg/cm^2

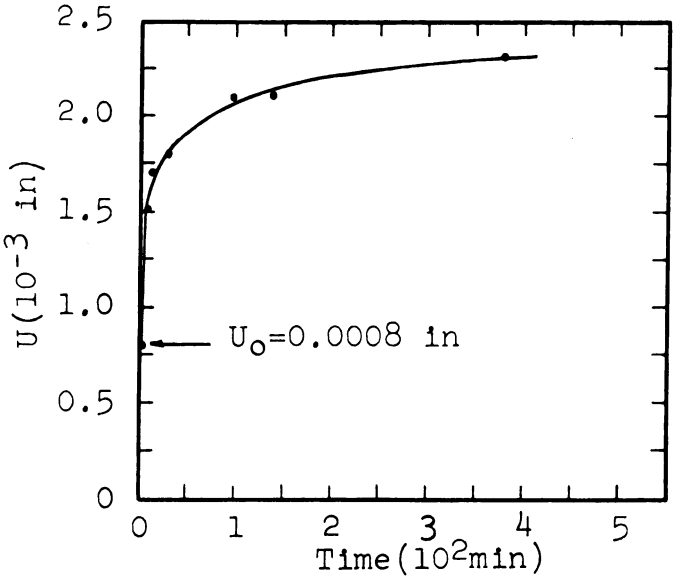

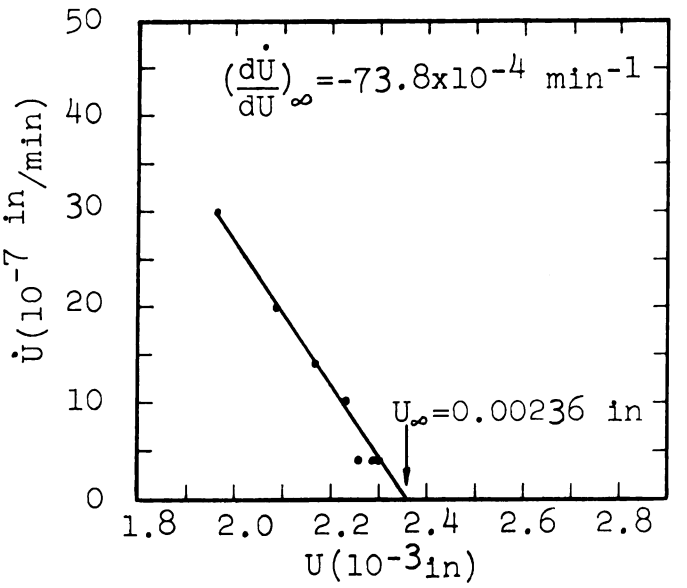

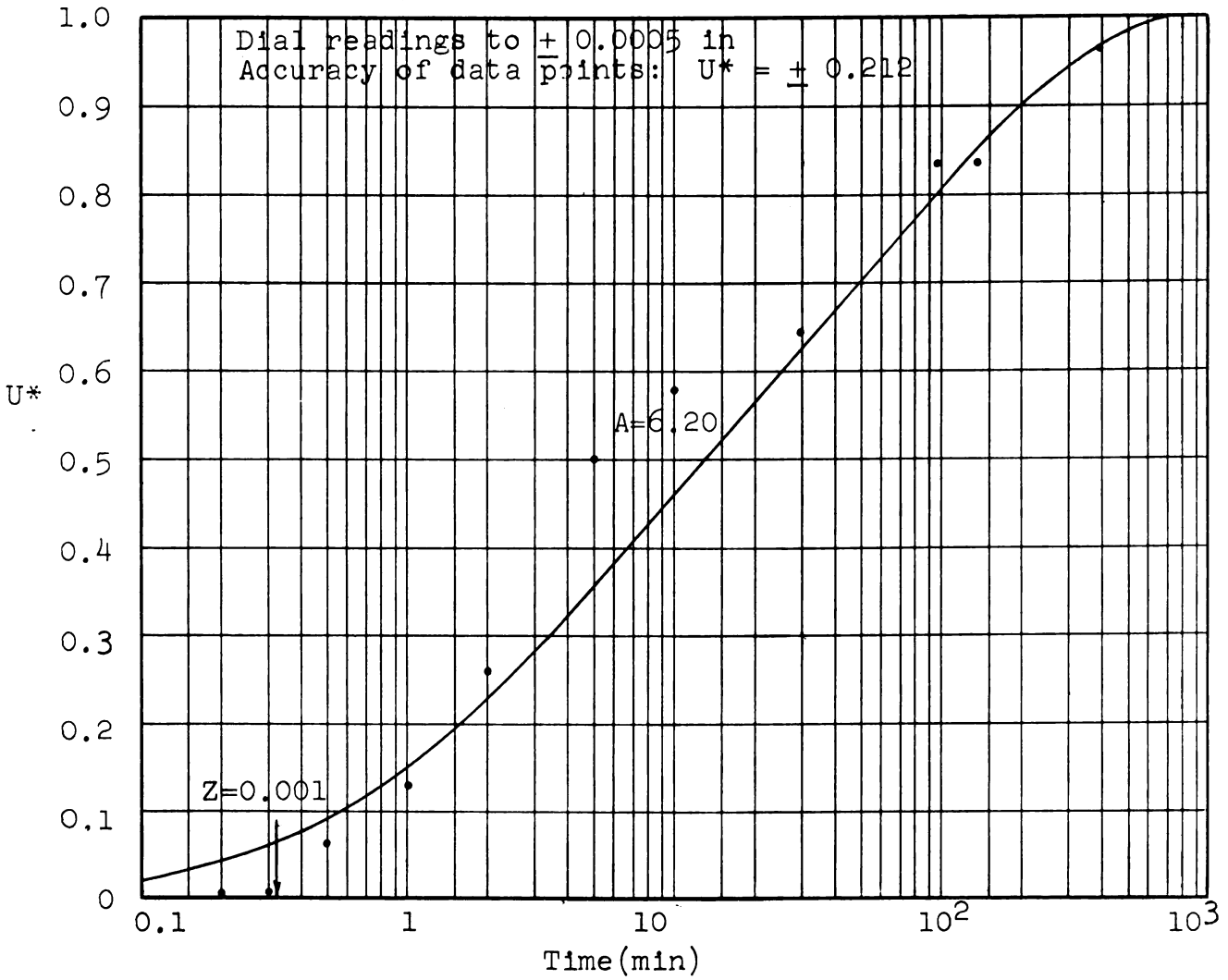

Figure A.9. Creep Curves for C-C-1-10; D = 1.112-0.700 kg/cm^2

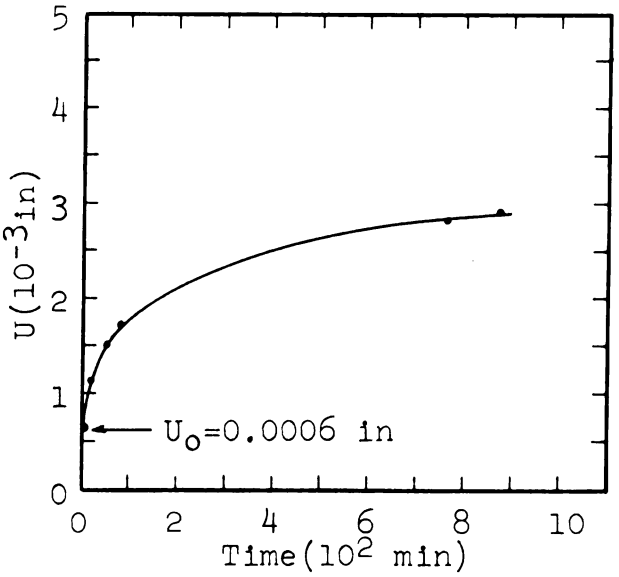

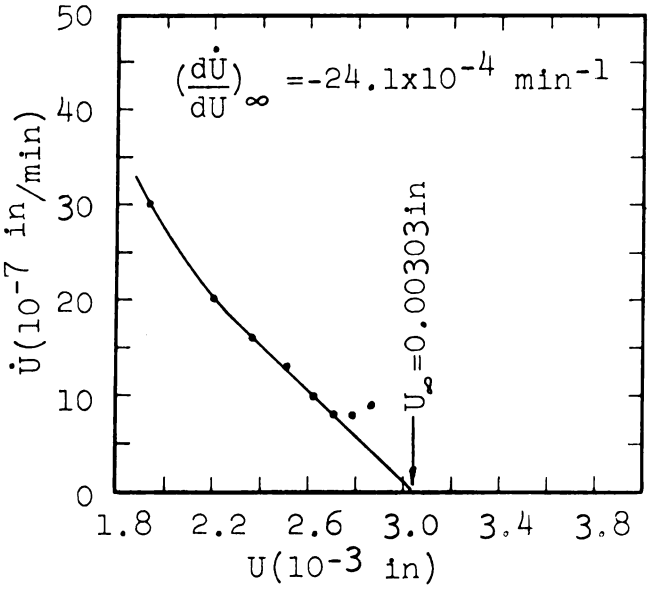

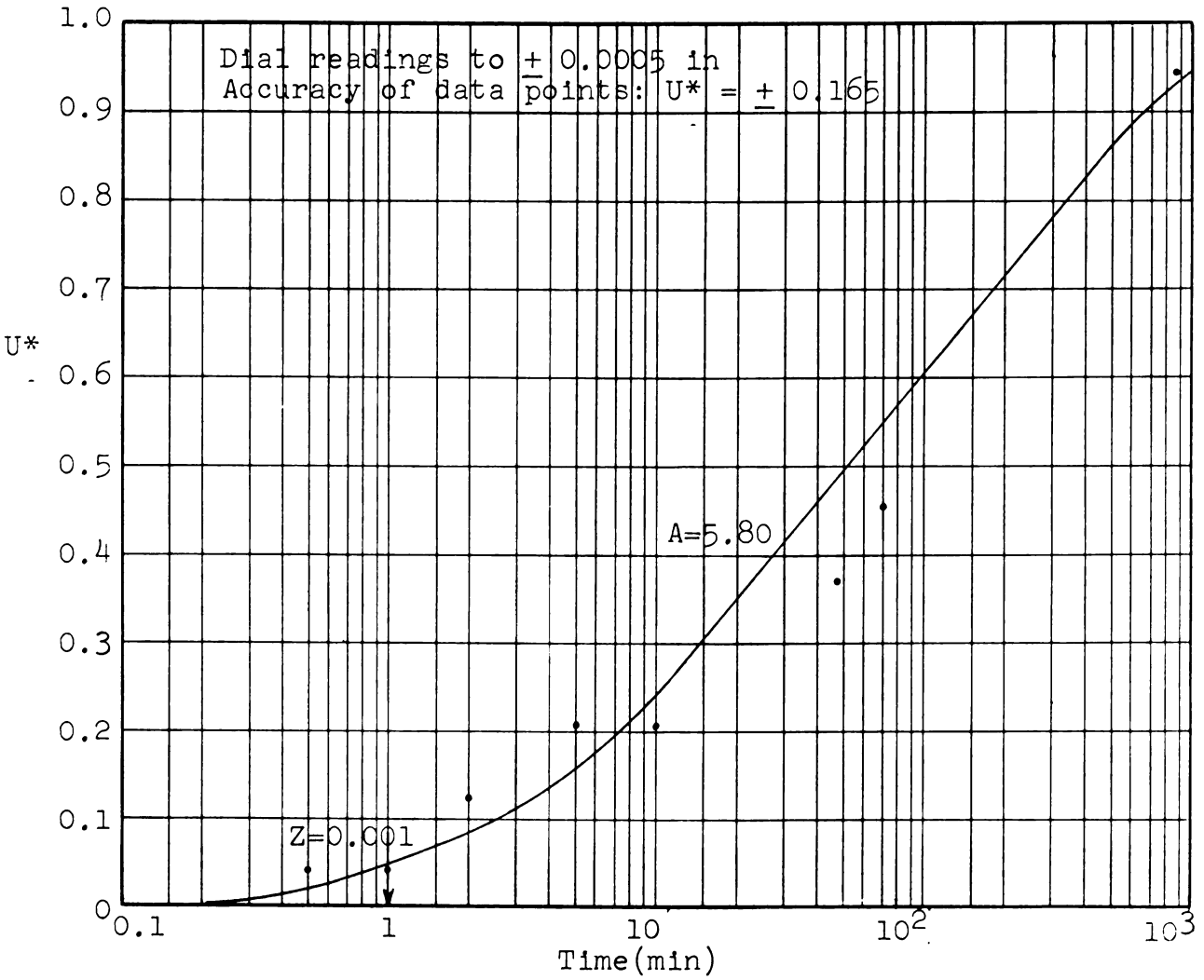

Figure A.10. Creep Curves for C-C-1-11; D = 0.700-0.457 $^{kg}/_{cm^2}$

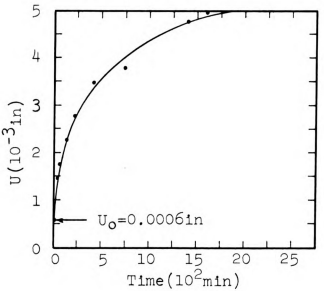

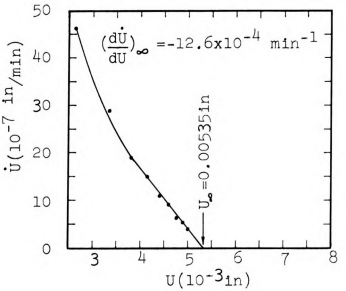

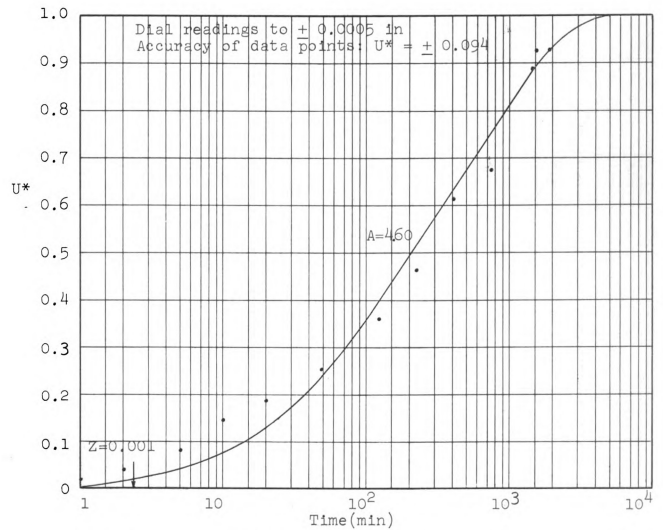

Figure A.11. Creep Curves for C-C-1-12; D=0.457-0.219 kg/cm^2

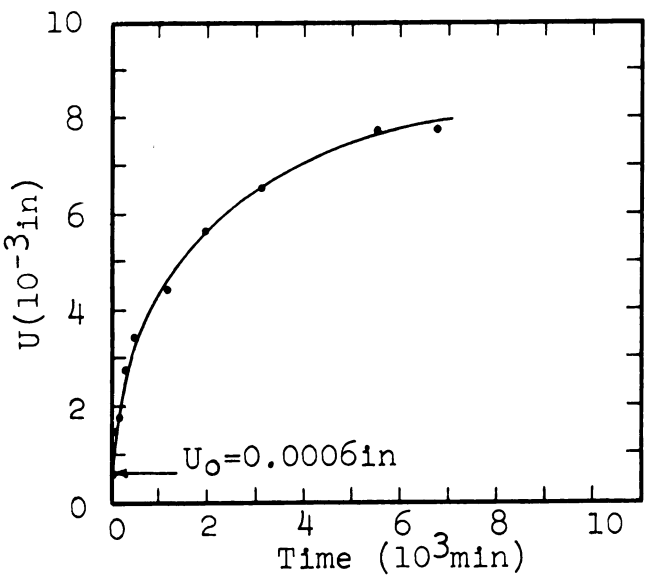

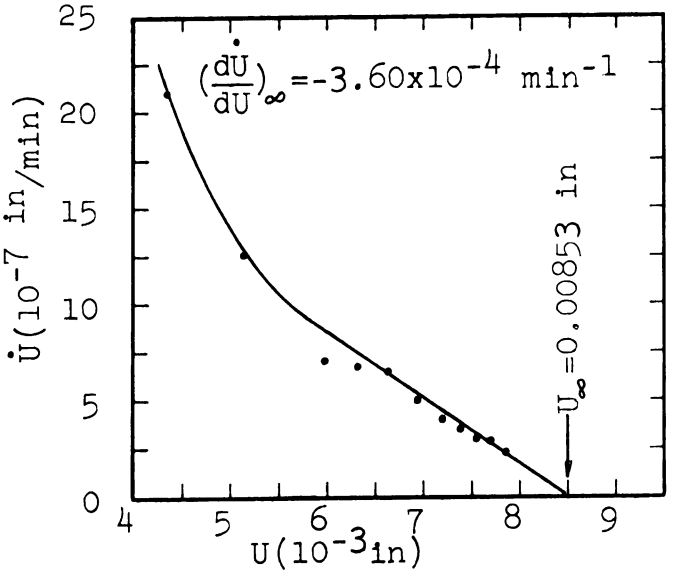

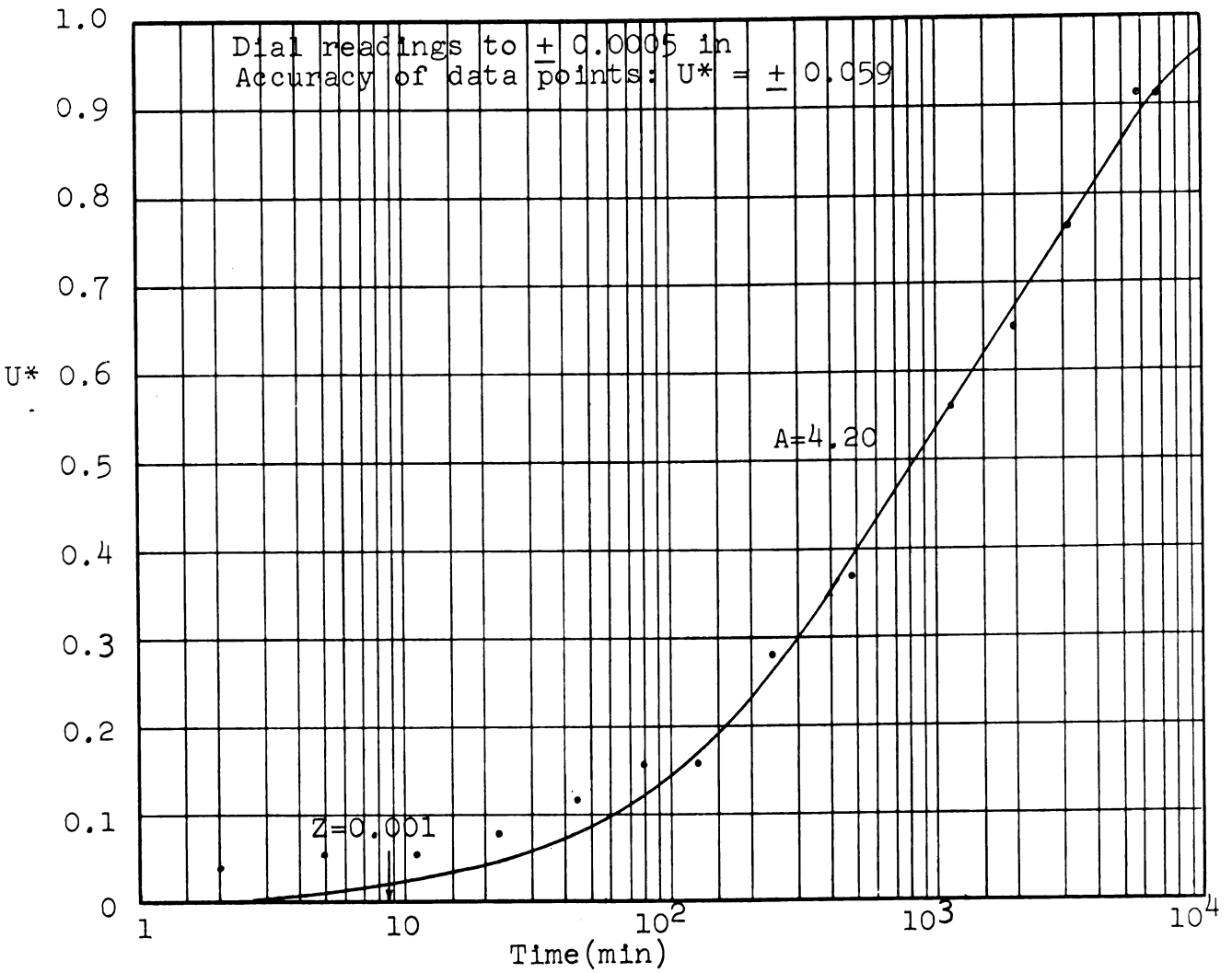

Figure A.12. Creep Curves for C-C-1-13; D=0.219-0 kg/cm^2

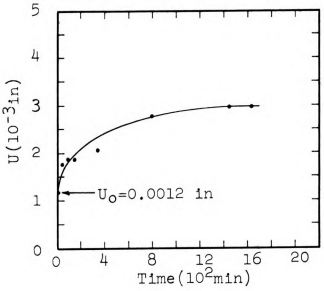

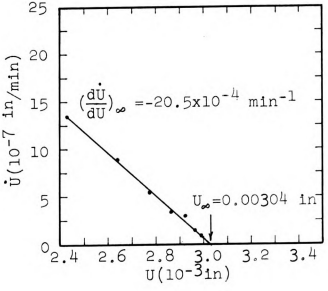

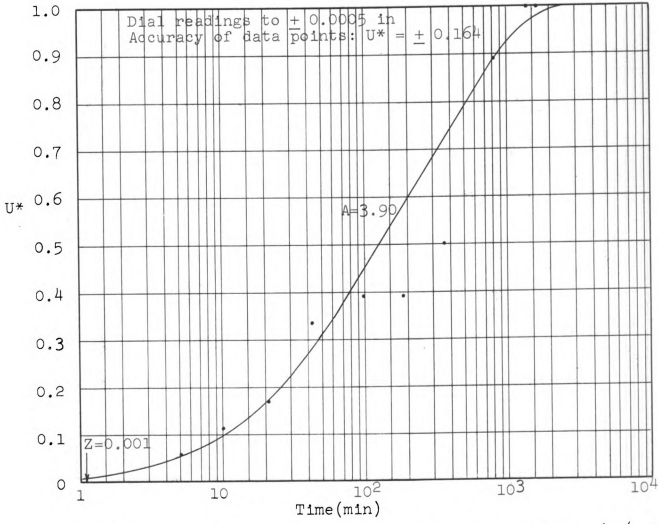

Figure A.13. Creep Curves for C-C-1-15; D=0.316-0.727 kg/cm^2

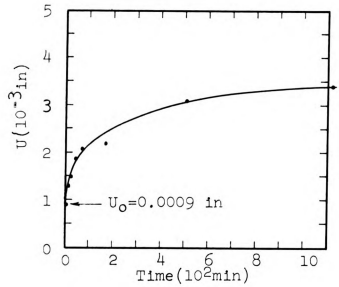

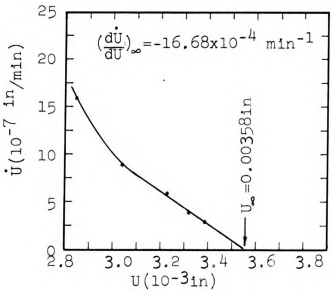

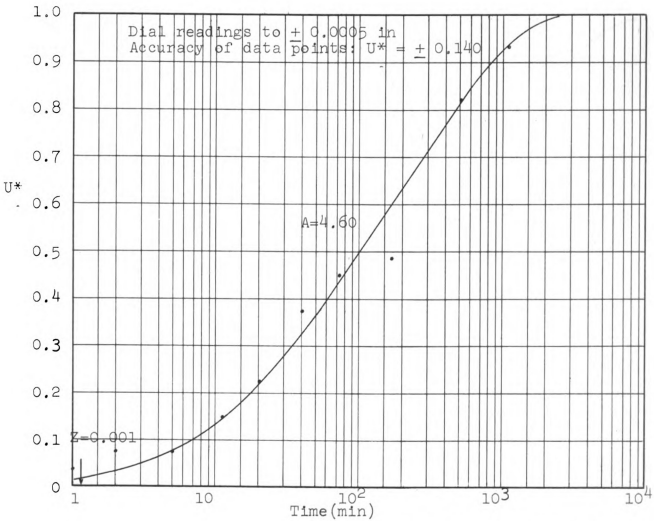

Figure A.14. Creep Curves for C-C-1-16; D=0.727-1.142 kg/cm^2

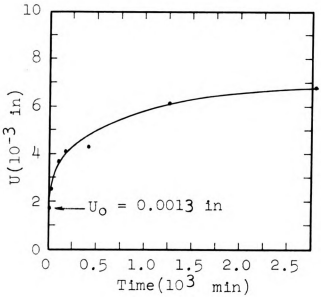

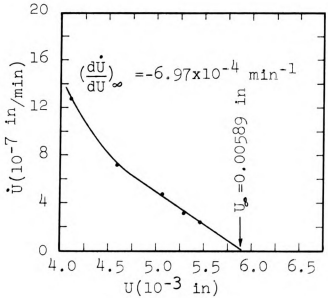

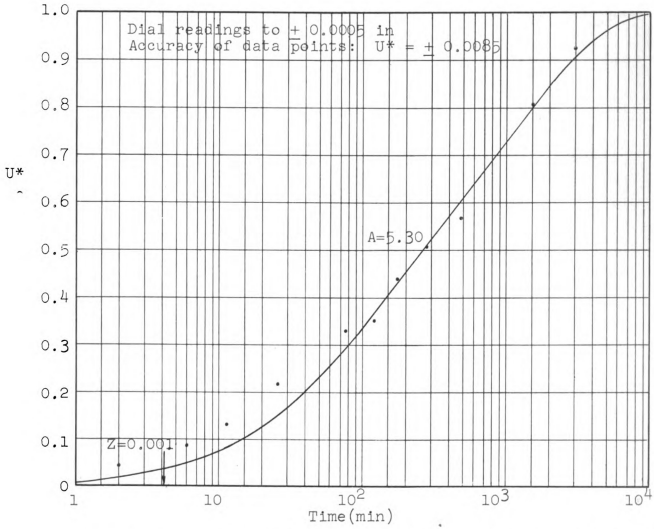

Figure A.15. Creep Curves for C-C-1-17; D=1.142-1.552 kg/cm^2

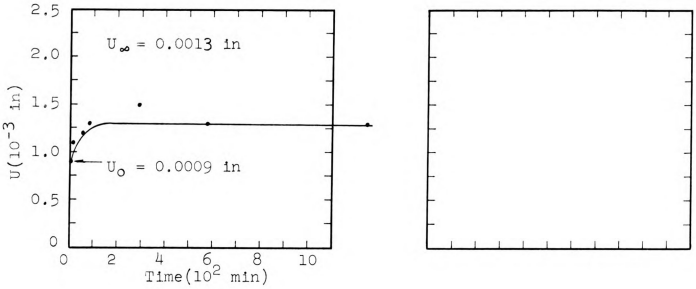

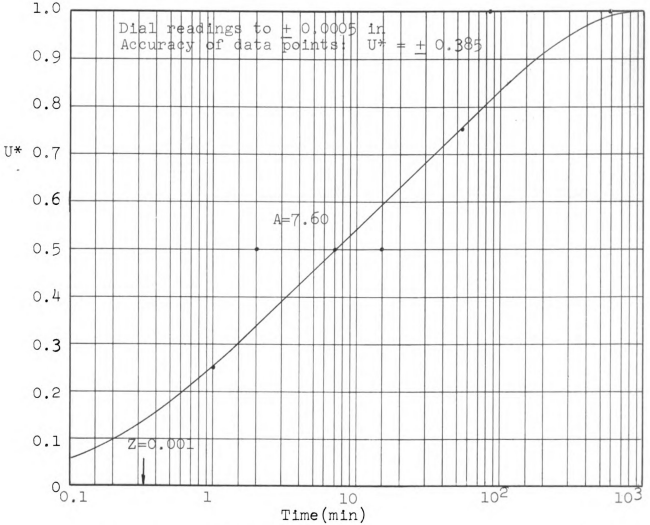

Figure A.16. Creep Curves for C-C-1-19; D=1.40-0.726 kg/cm^2

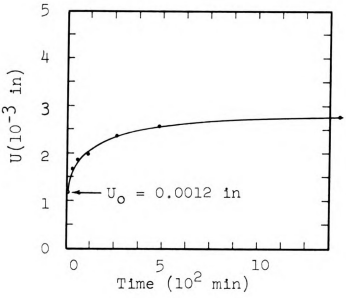

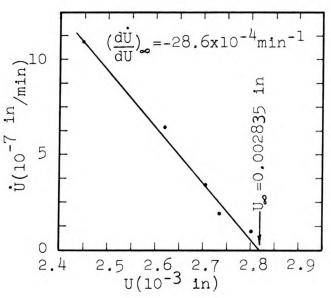

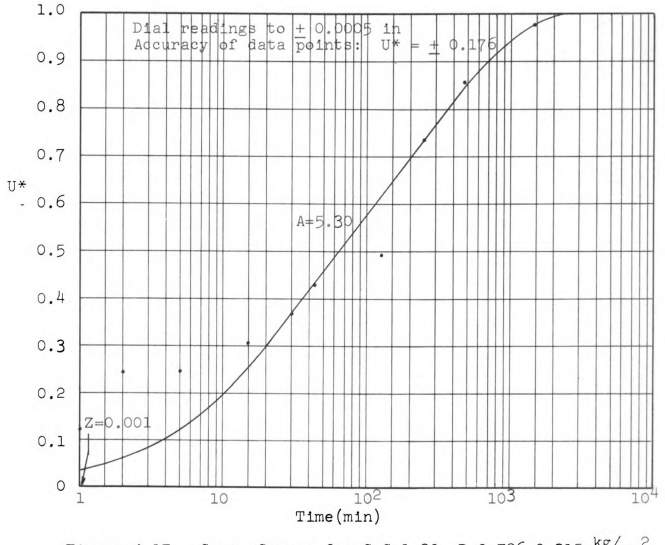

Figure A.17. Creep Curves for C-C-1-20; D=0.726-0.315 kg/cm^2

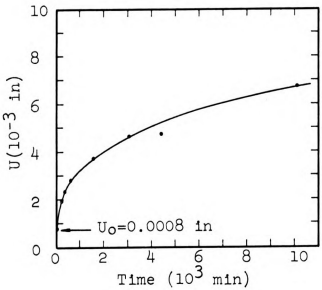

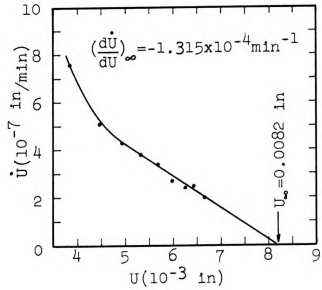

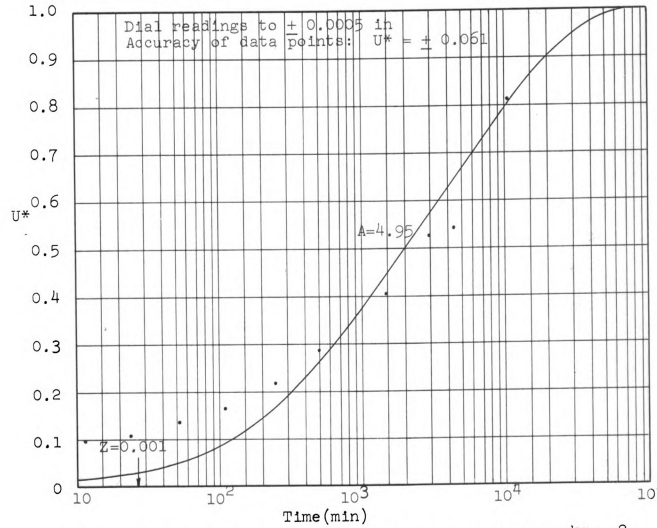

Figure A.18. Creep Curves for C-C-1-21; D=0.315-0 kg/cm^2

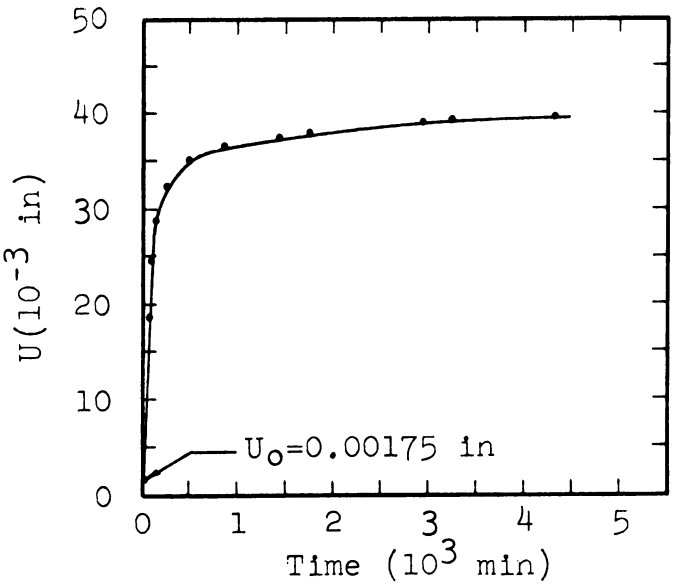

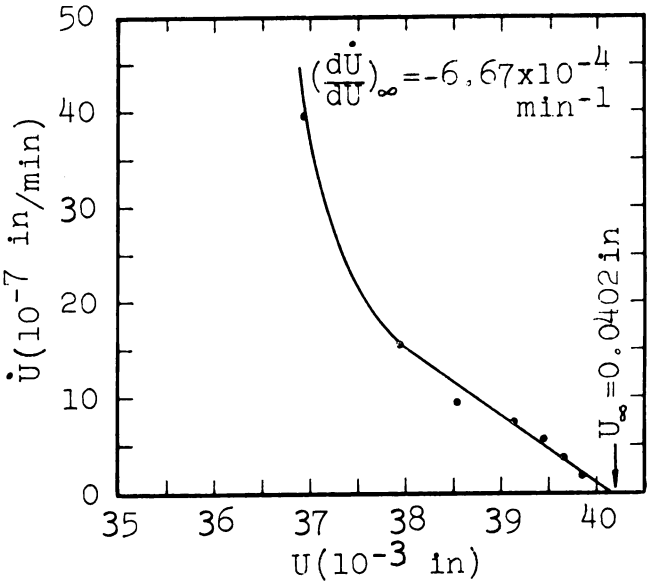

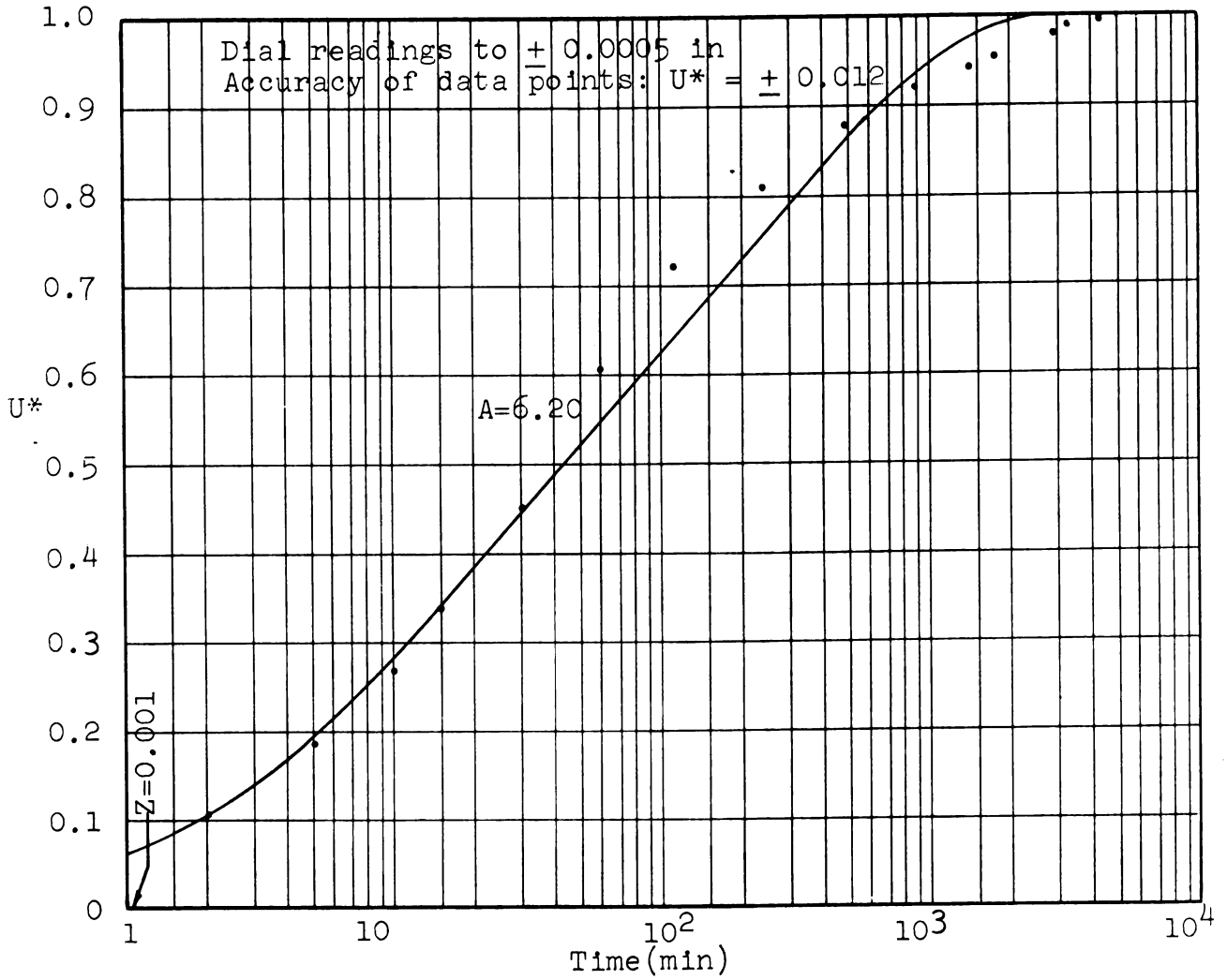

Figure A.19. Creep Curves for C-C-7-1; D = 0-0.987 kg/cm^2

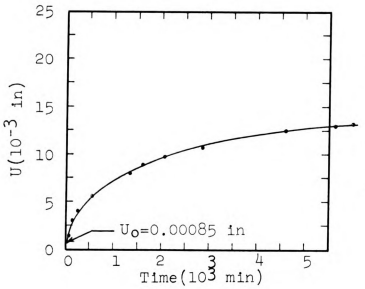

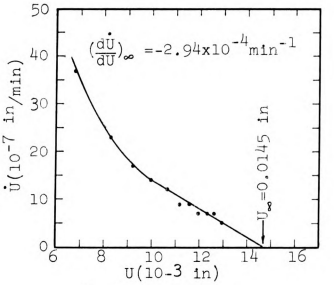

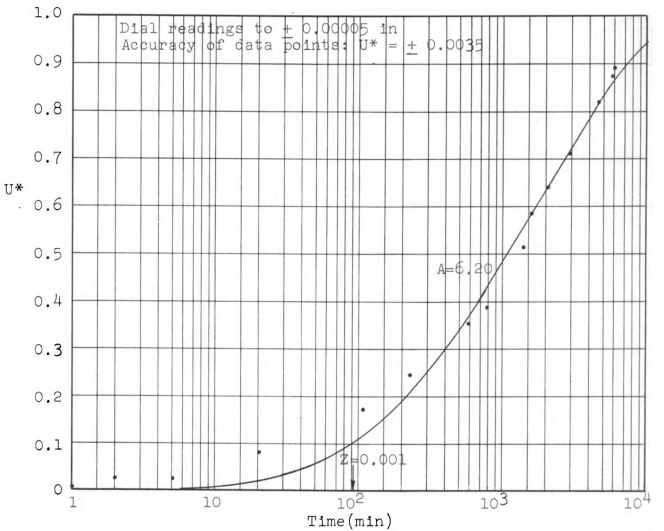

Figure A.20. Creep Curves for F-C-1-3; D=0.749-0.994 kg/cm²

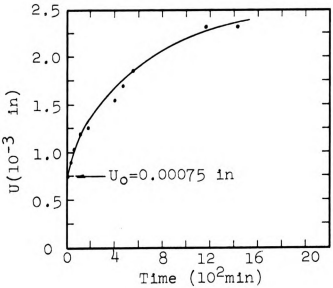

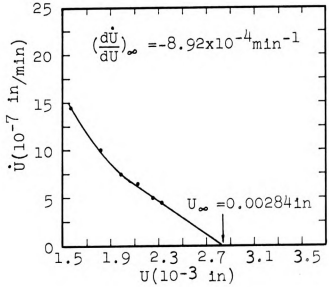

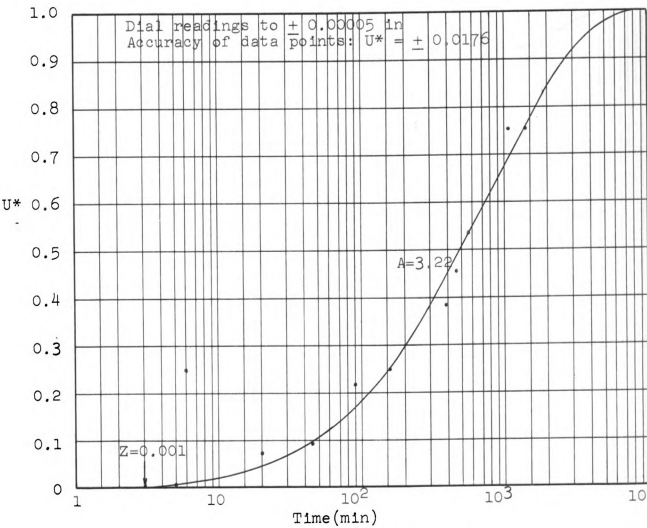

Figure A.21. Creep Curves for F-C-2-2; D=0.250-0.500 kg/cm^2

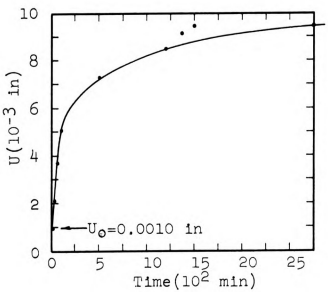

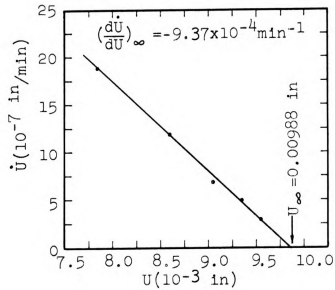

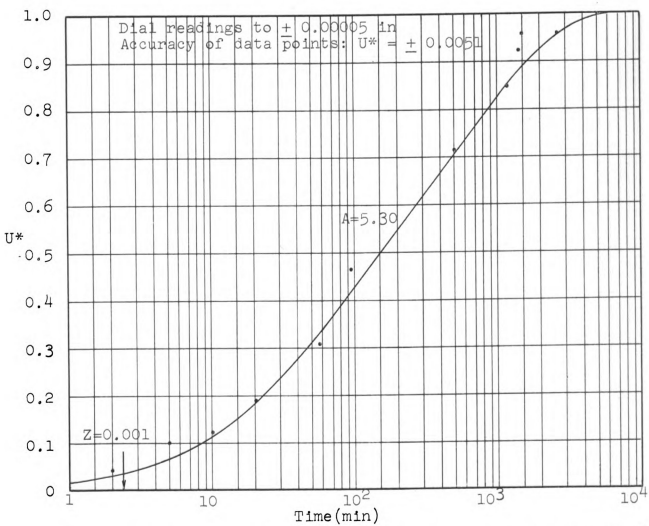

Figure A.22. Creep Curves for F-C-2-3; D=0.500-0.747 kg/cm^2

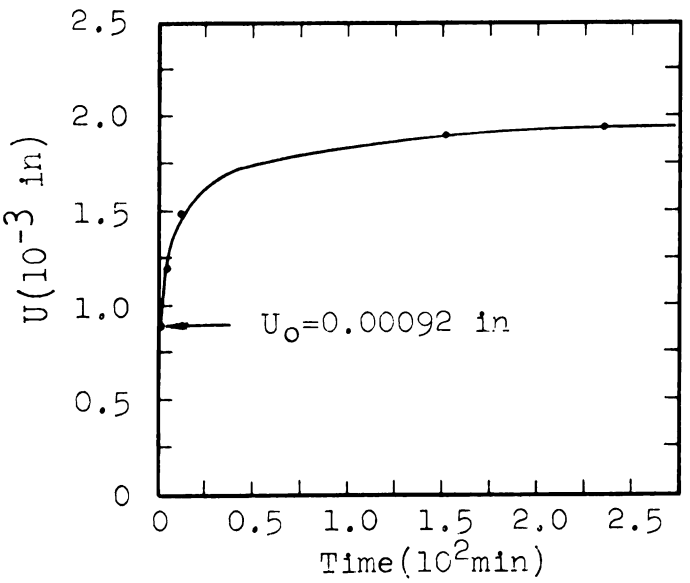

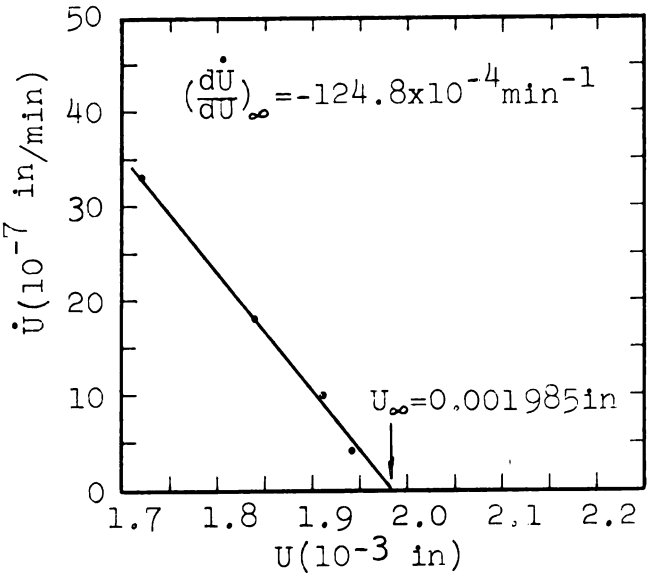

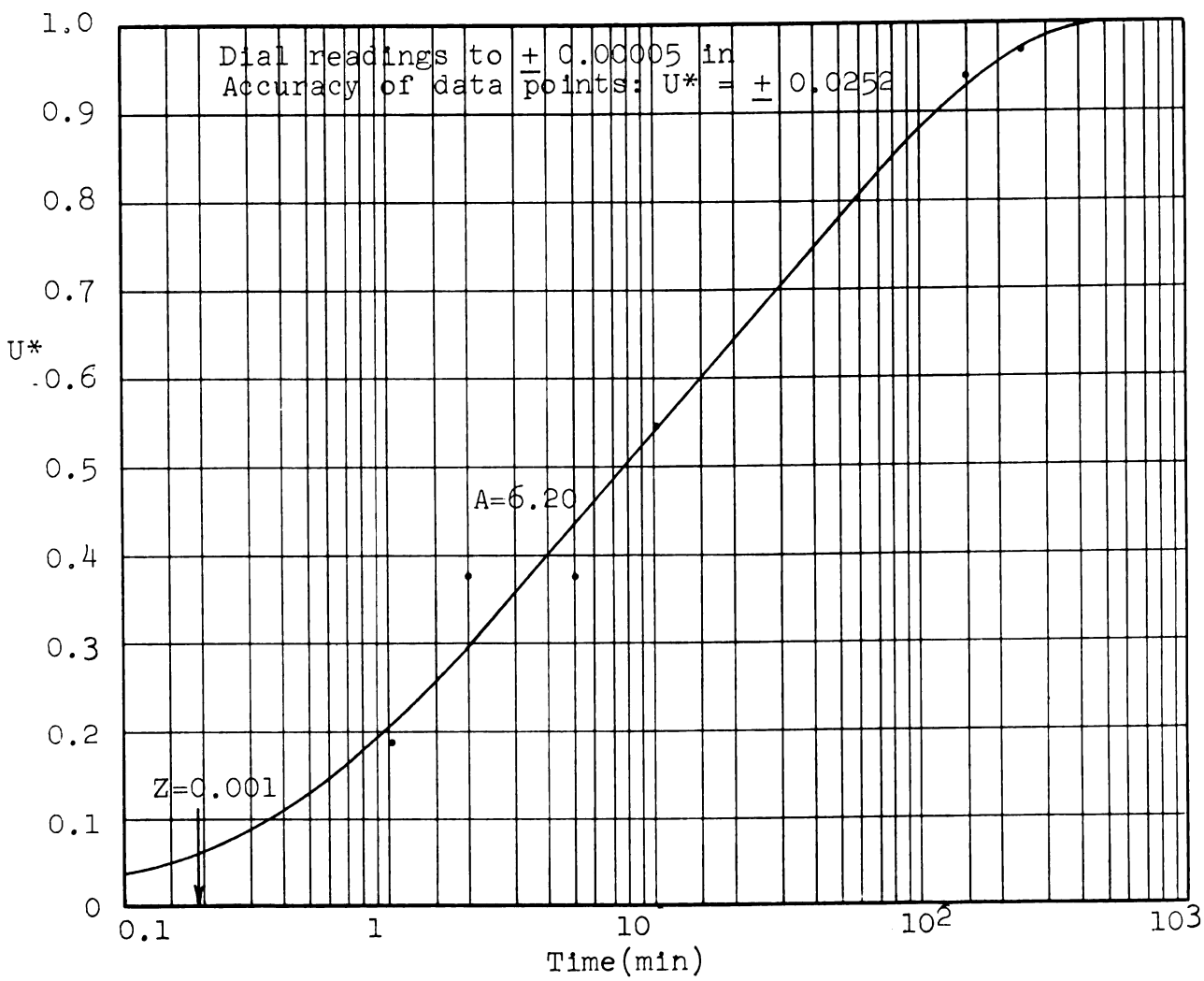

Figure A.23. Creep Curves for F-C-2-7; D = 0-0.250 $^{kg}/_{cm^2}$

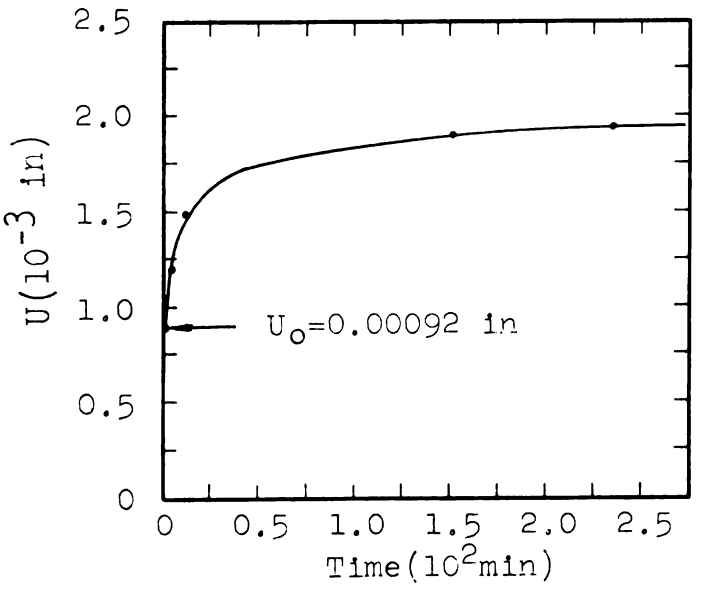

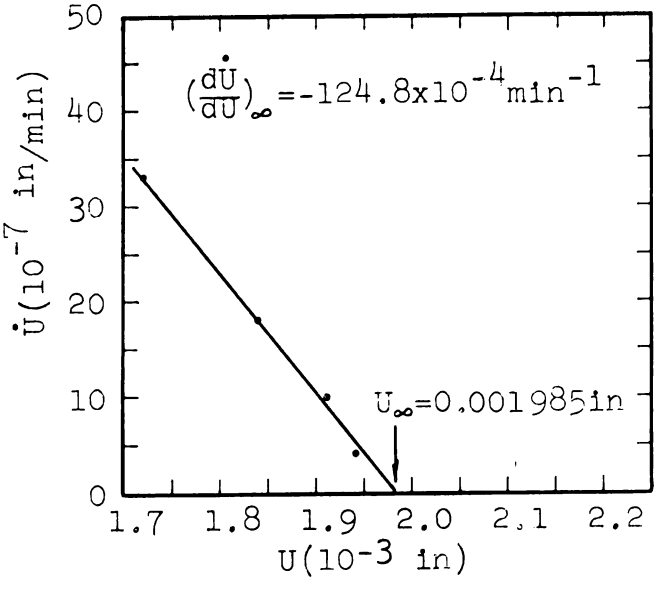

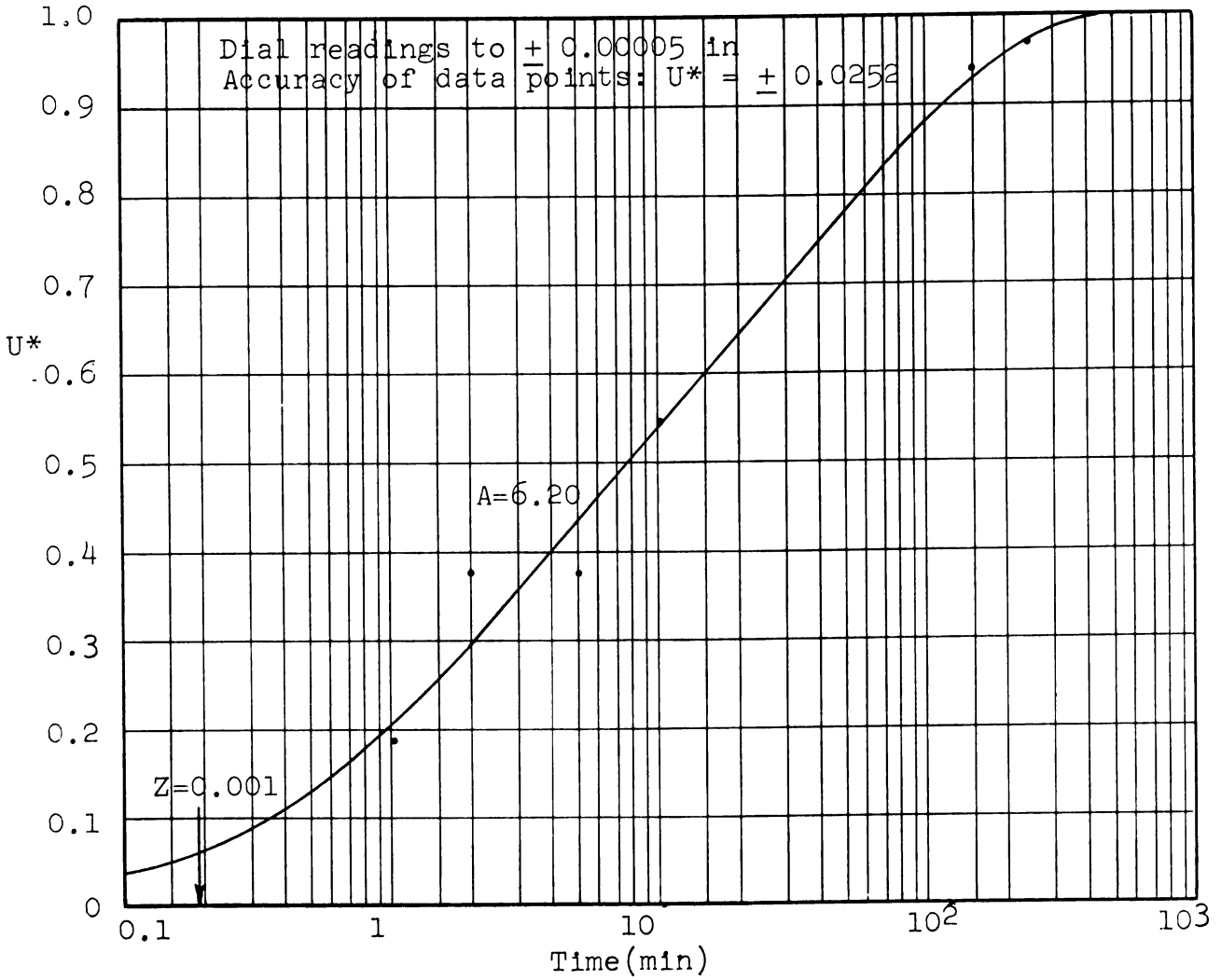

Figure A.23. Creep Curves for F-C-2-7; D = 0-0.250 $^{kg}/_{cm^2}$

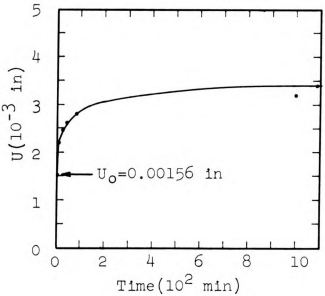

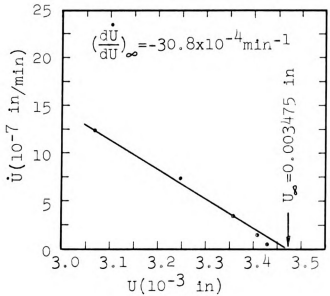

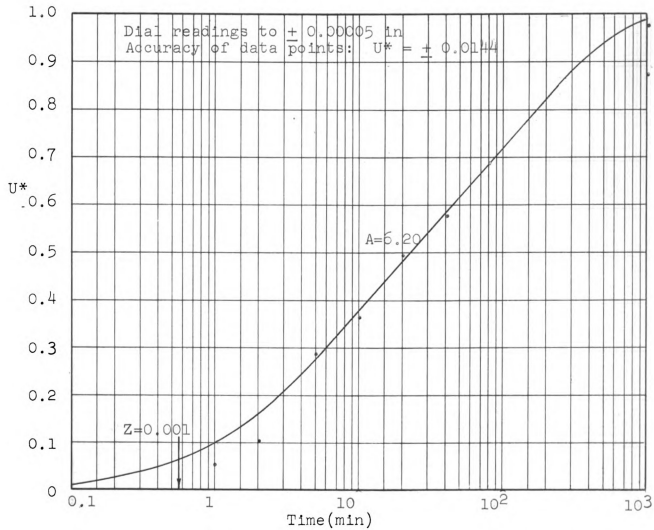

Figure A.24. Creep Curves for F-C-2-8; D = 0.250-0.499 kg/cm^2

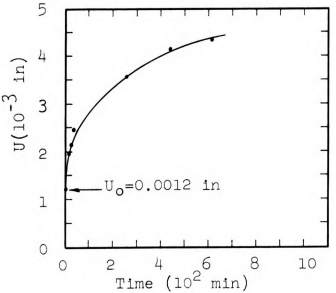

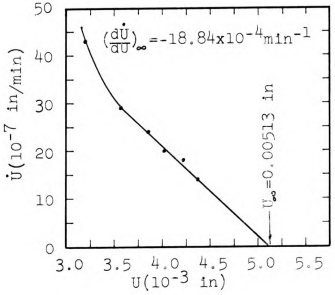

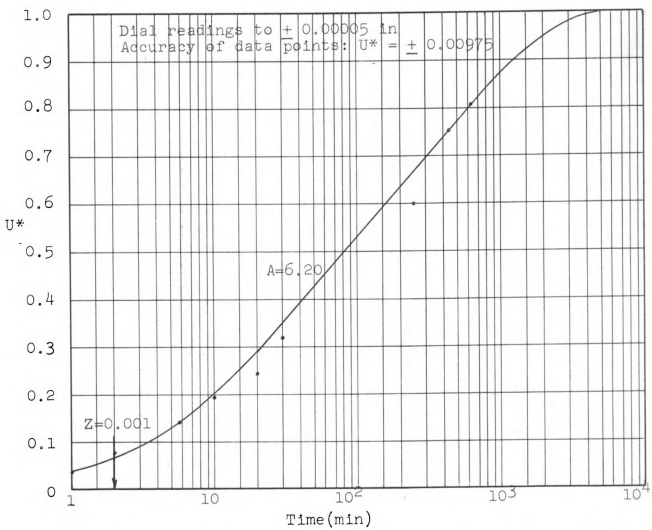

Figure A.25. Creep Curves for F-C-2-9; D = 0.498-0.746 kg/cm^2

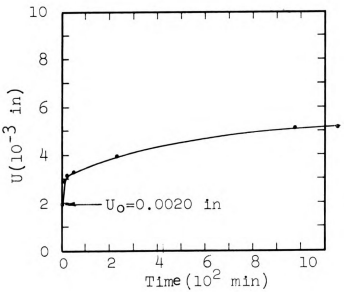

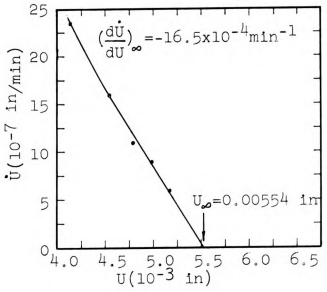

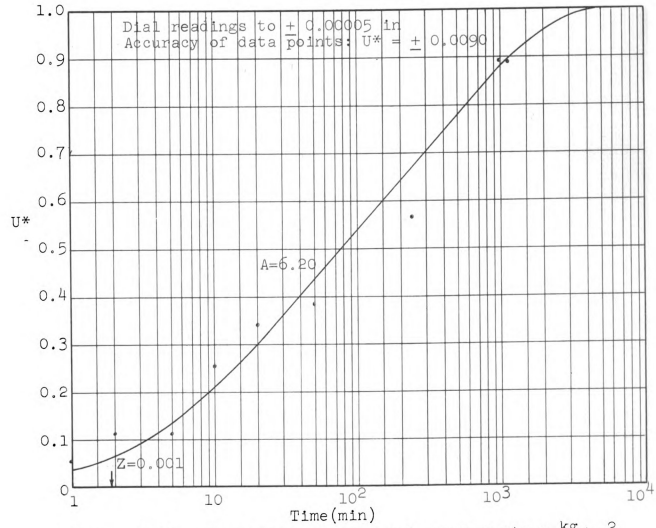

Figure A.26. Creep Curves for F-C-2-12; D=0.249-0 kg/cm^2

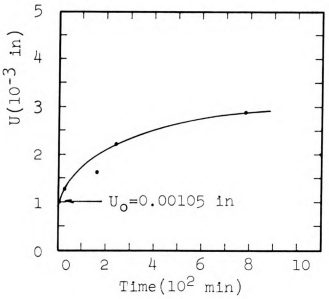

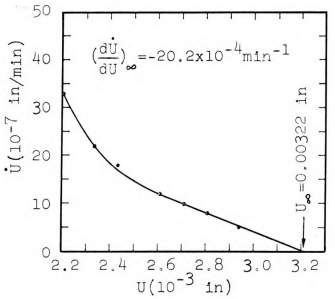

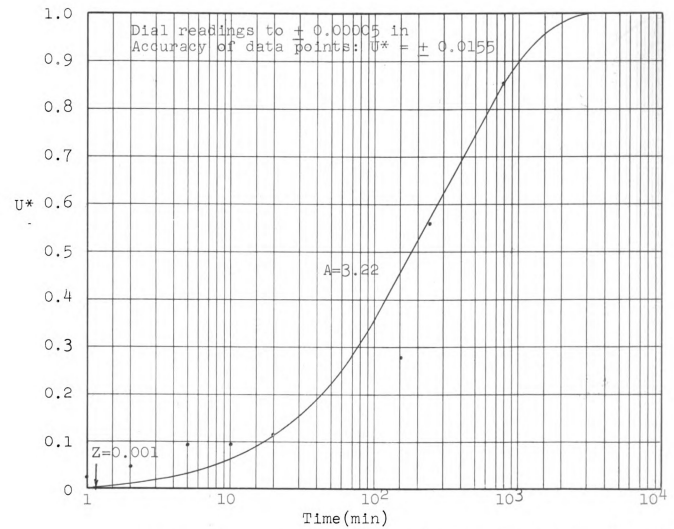

Figure A.27. Creep Curves for F-C-2-14; D=0.249-0.498 kg/cm^2

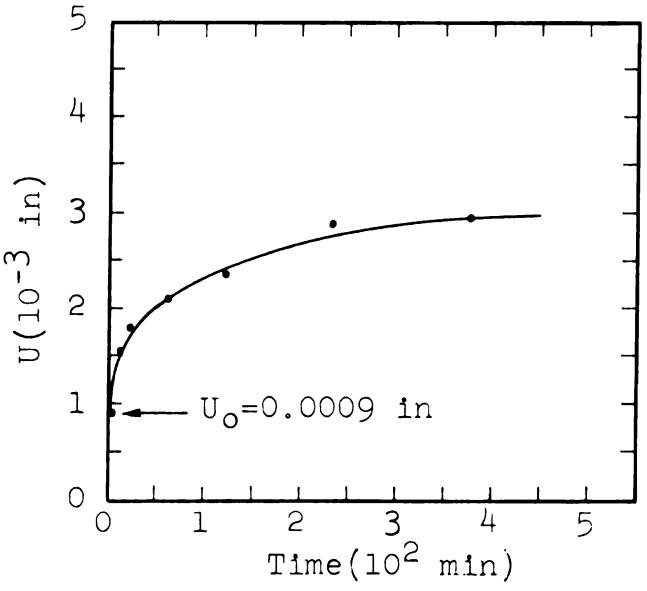

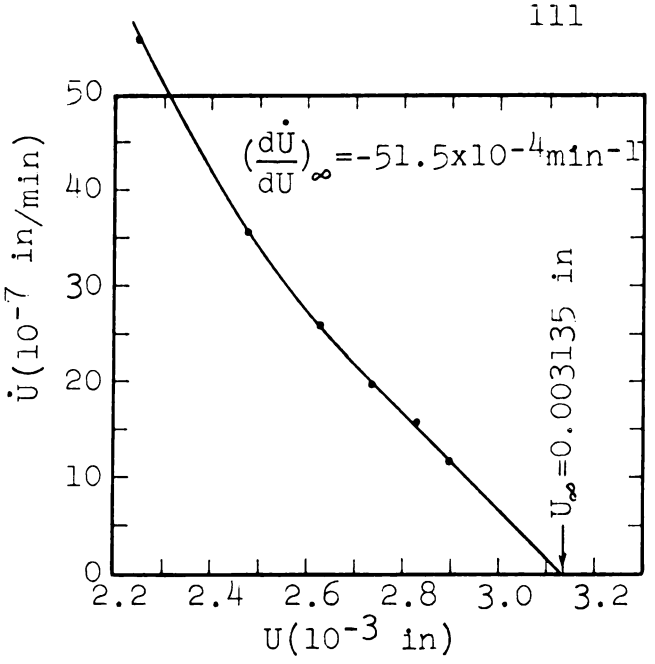

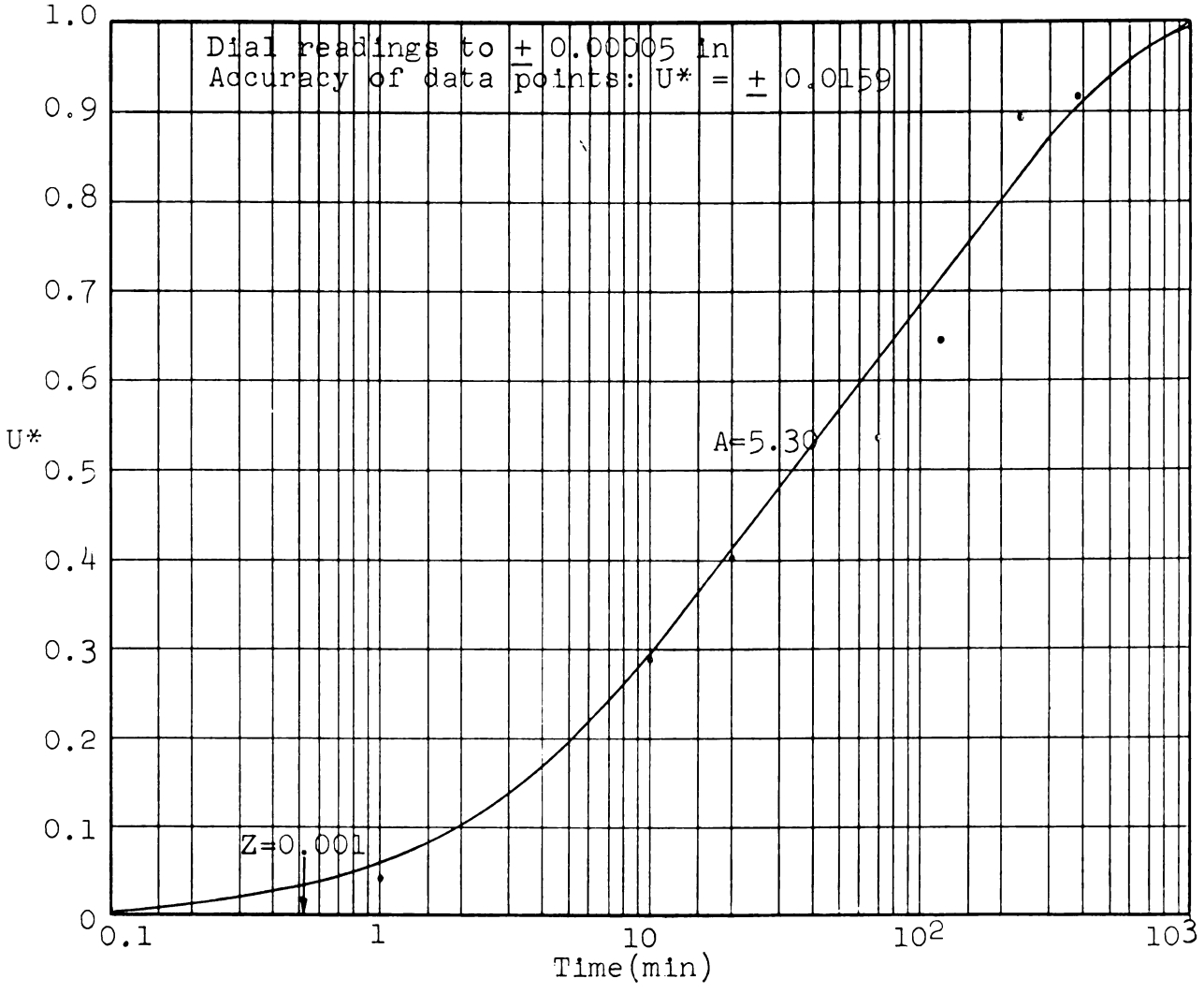

Figure A.28. Creep Curves for F-C-2-15; D=0.498-0.746 kg/cm^2

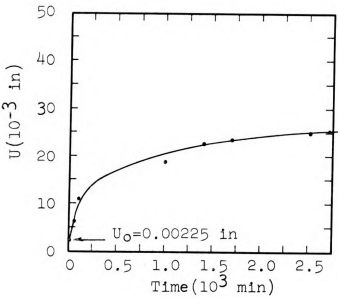

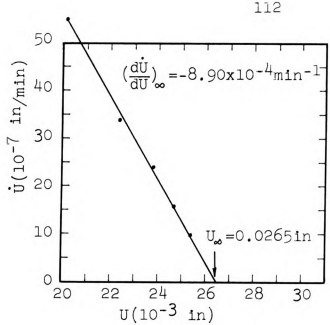

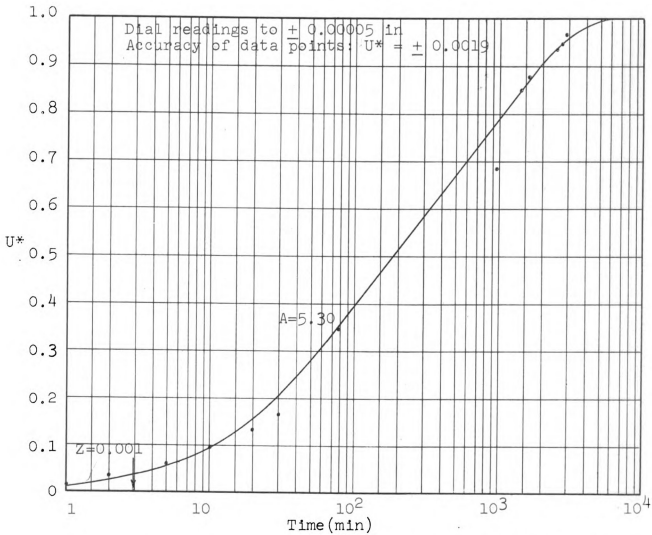

Figure A.29. Creep Curves for F-C-2-16; D=0.746-0.990 kg/cm^2

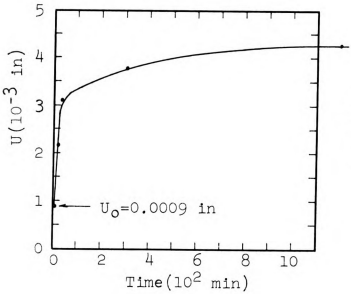

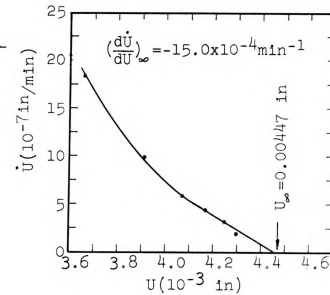

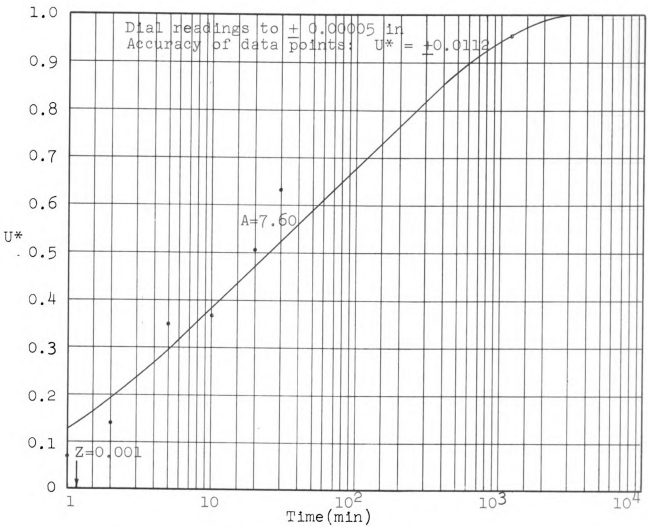

Figure A.30. Creep Curves for F-C-2-19; D=0.492-0.247 kg/cm^2

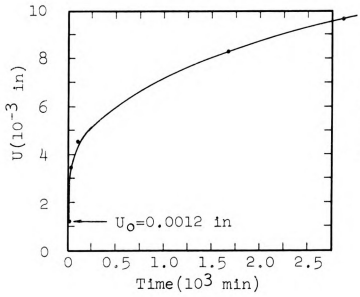

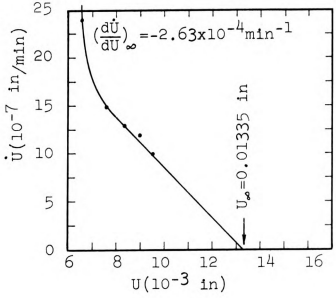

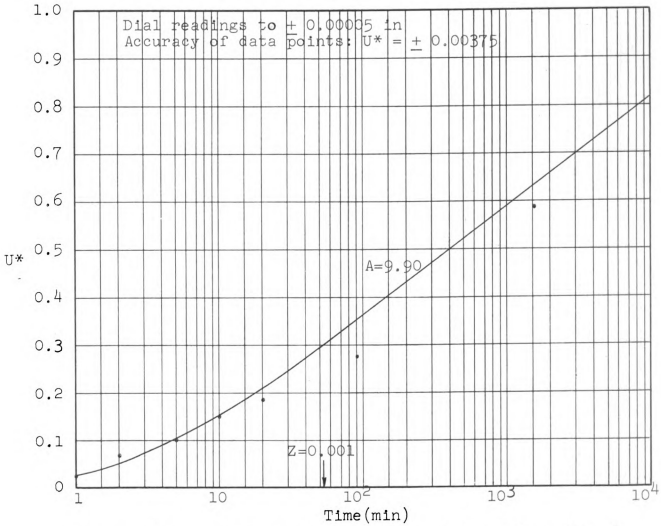

Figure A.31. Creep Curves for F-C-2-20; D=0.247-0 kg/cm^2

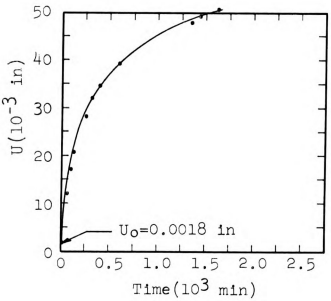

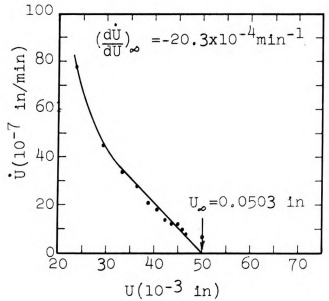

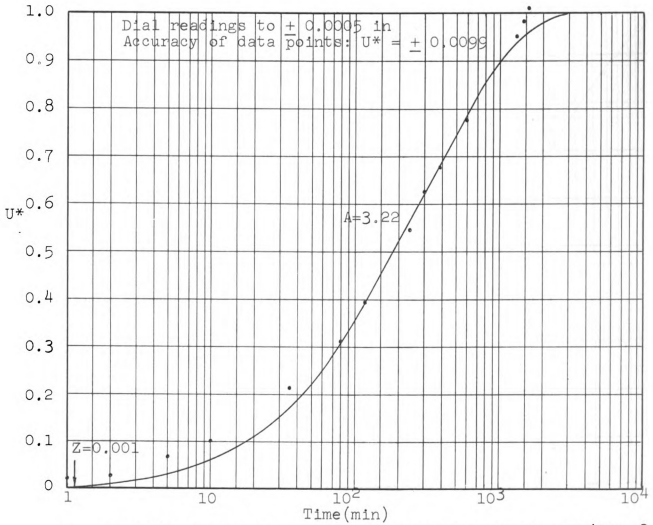

Figure A.32. Creep Curves for F-C-2-33: D=0.952-1.152 kg/cm²

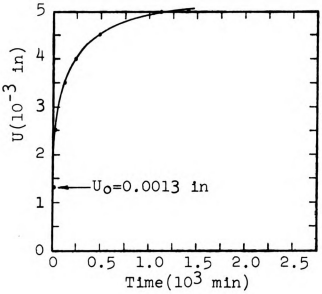

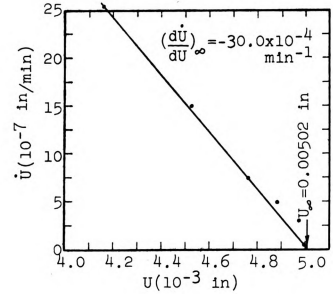

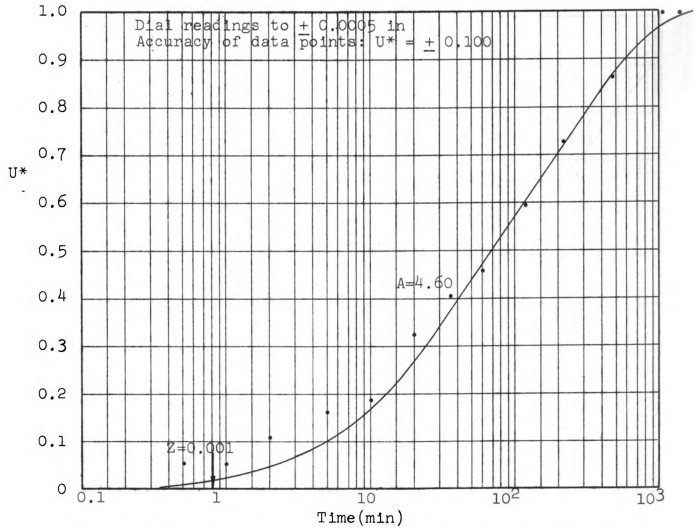

Figure A.33. Creep Curves for F-C-8-1; D=0-0.499 kg/cm^2

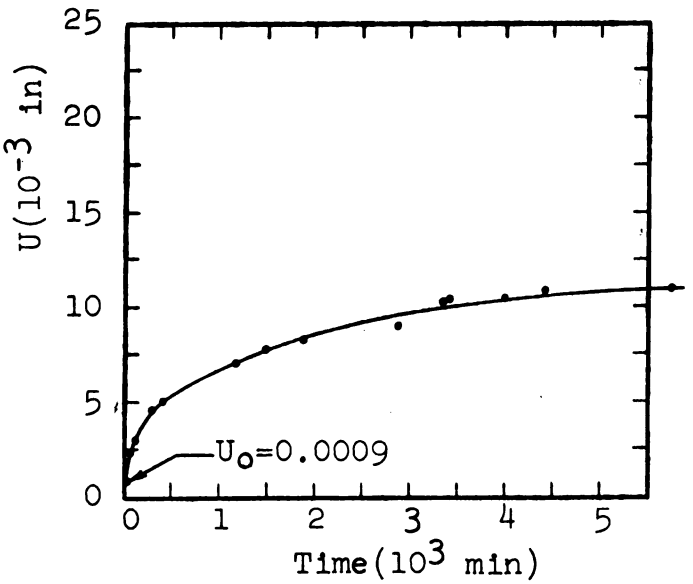

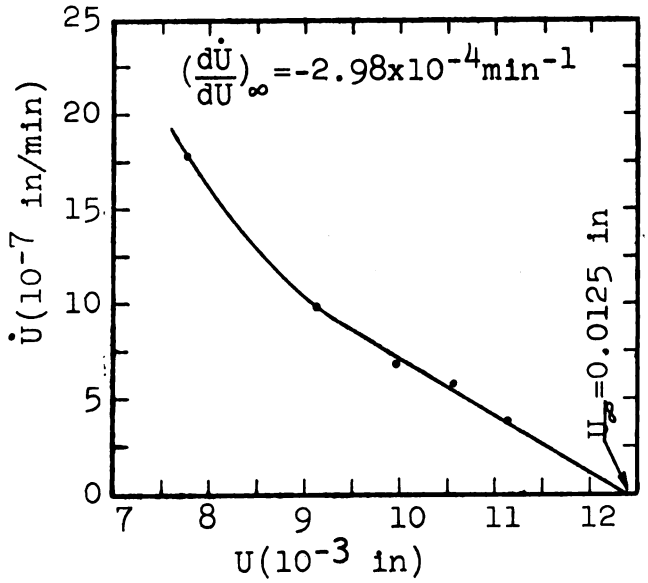

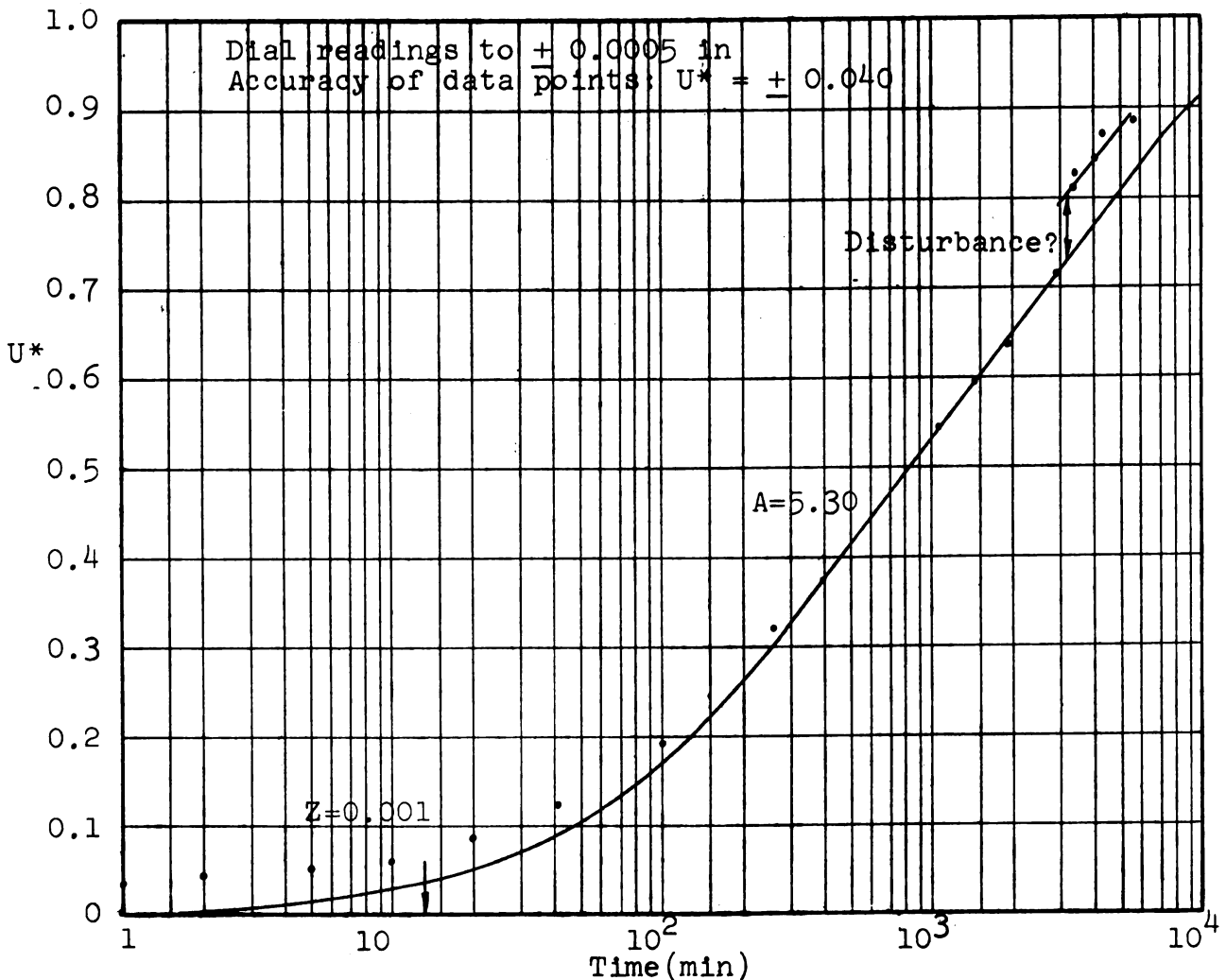

Figure A.34. Creep Curves for F-C-8-2; D=0.499-0.755 kg/cm^2

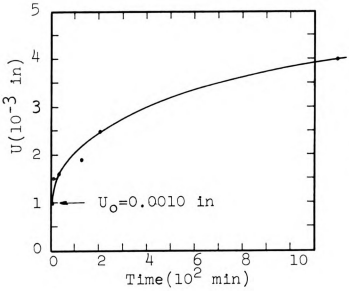

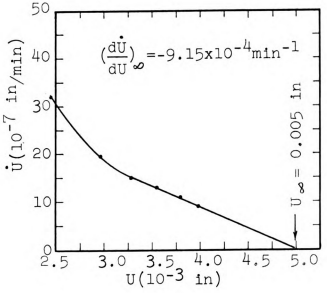

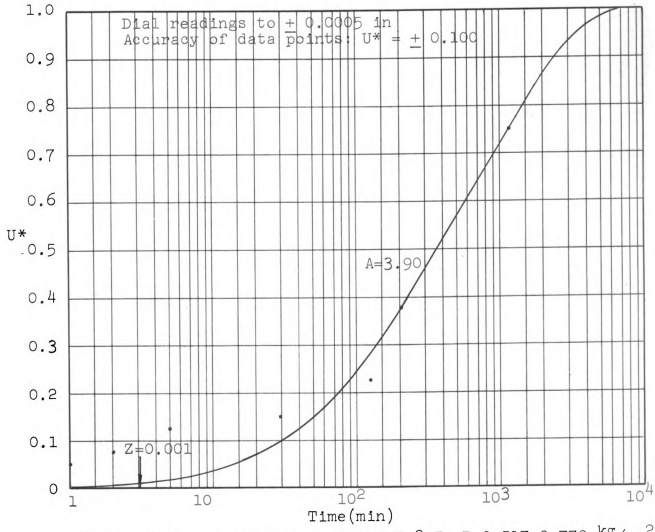

Figure A.35. Creep Curves for F-C-8-7; D=0.517-0.770 kg/cm²

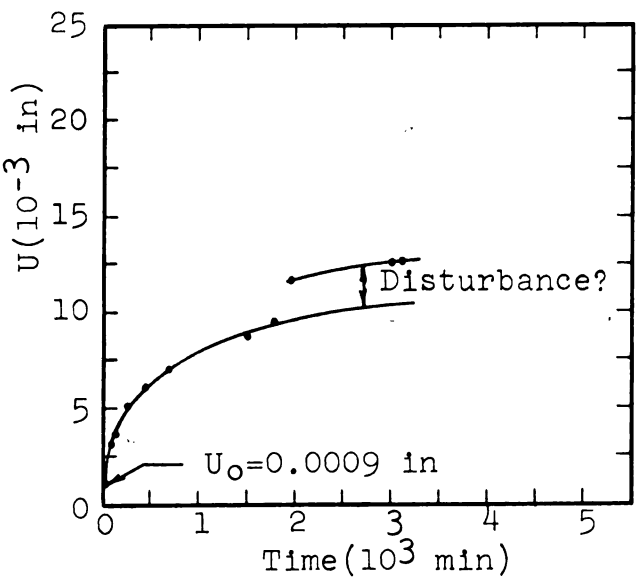

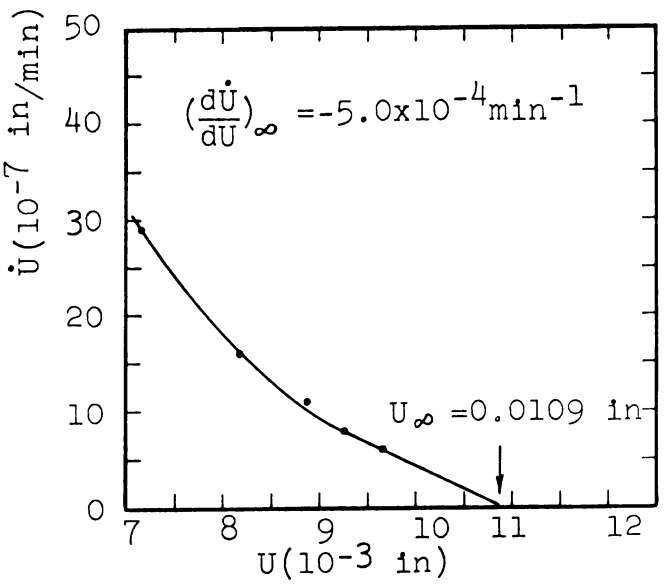

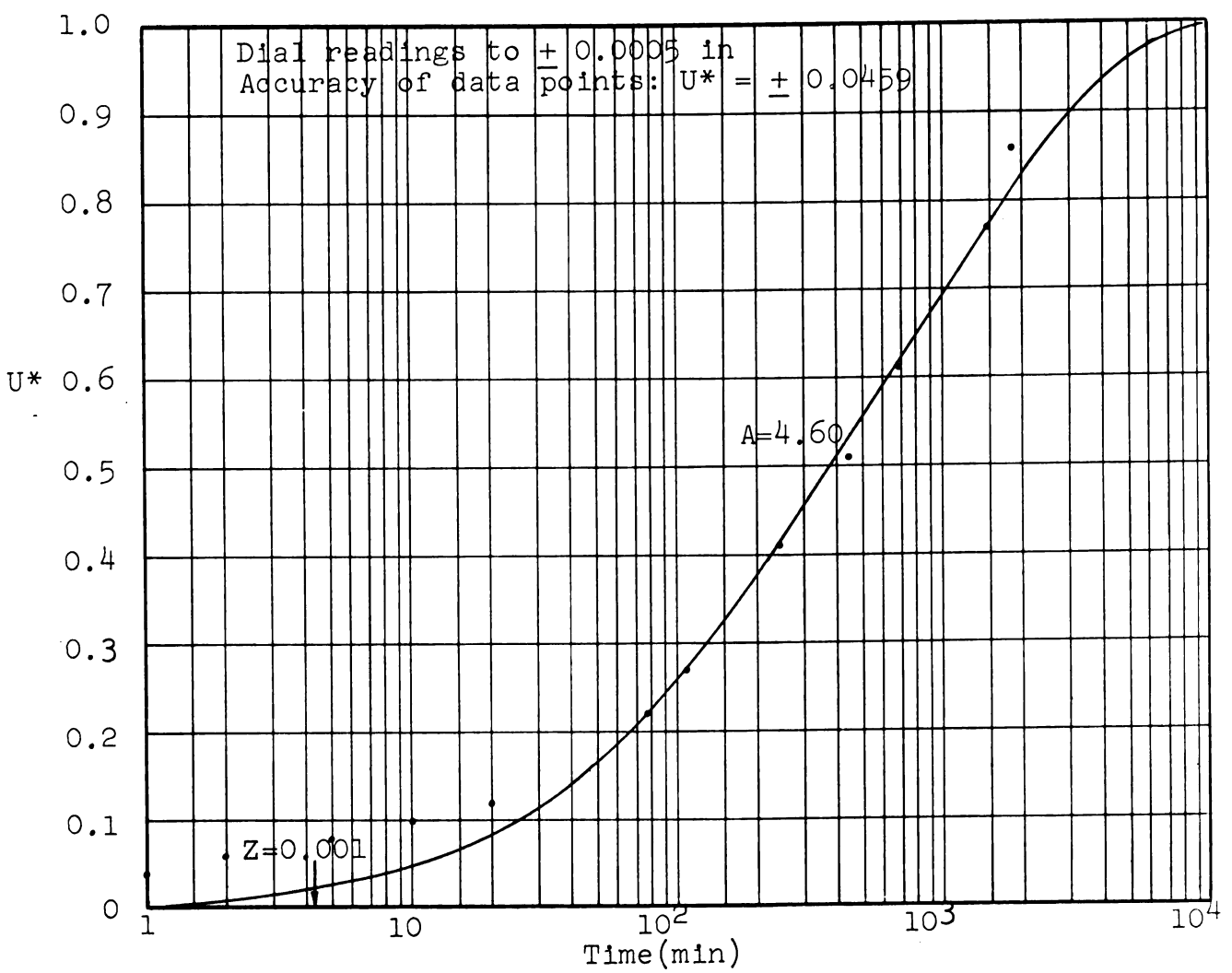

Figure A.36. Creep Curves for F-C-8-8; D=0.770-1.025 kg/cm^2

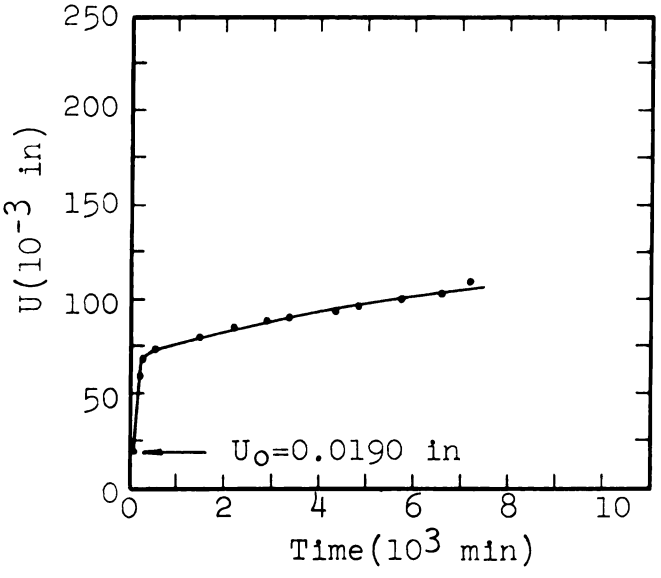

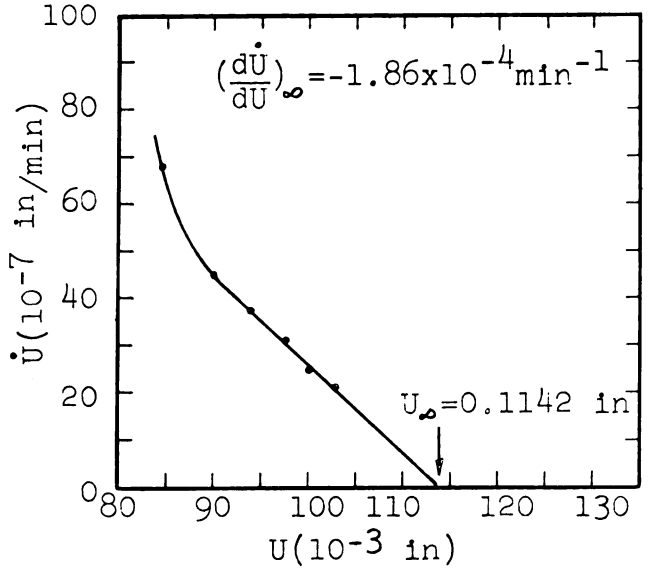

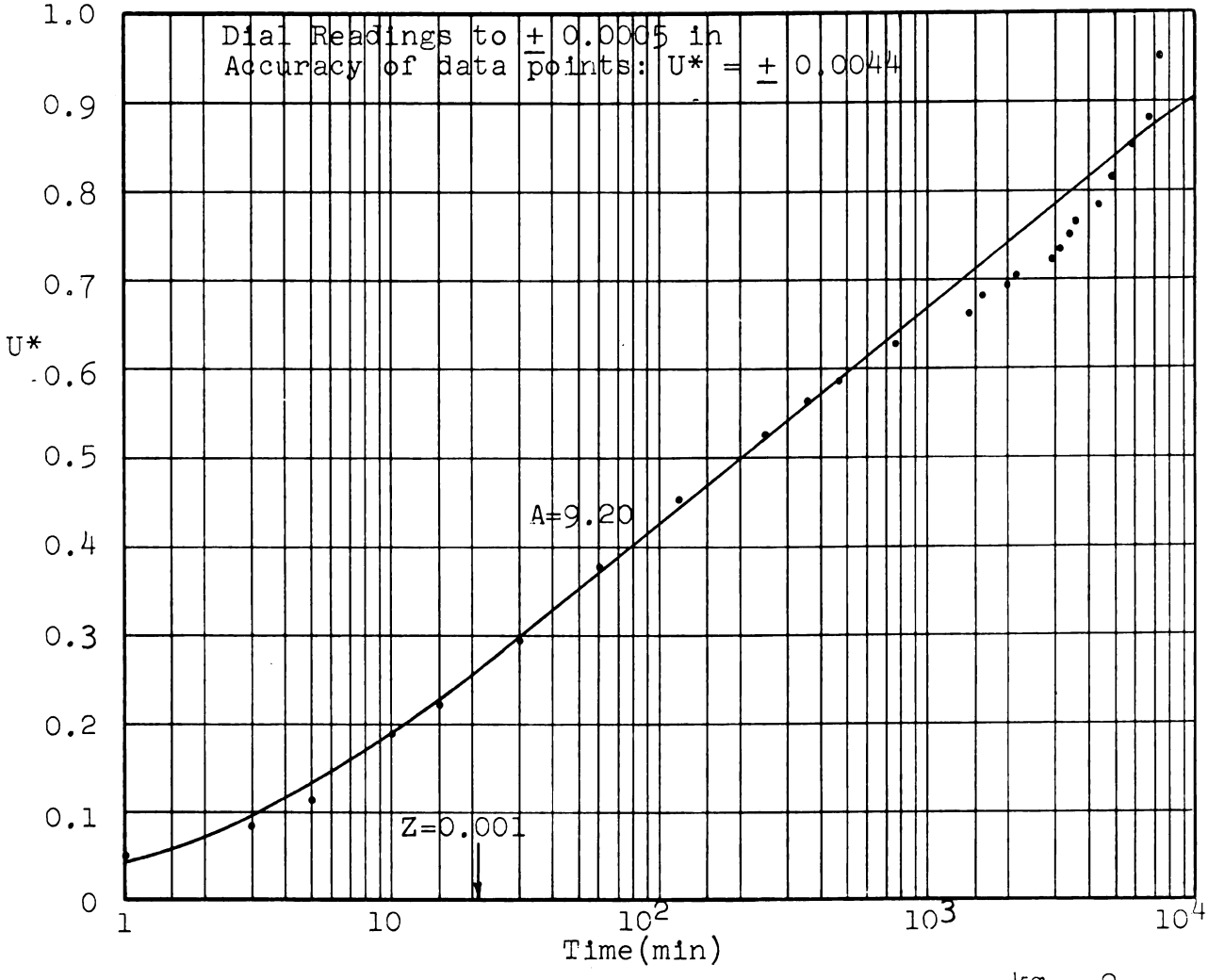

Figure A.37. Creep Curves for F-C-9-1; D=0-1.103 kg/cm^2

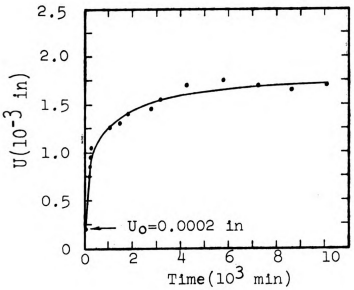

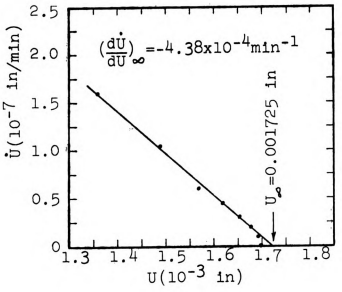

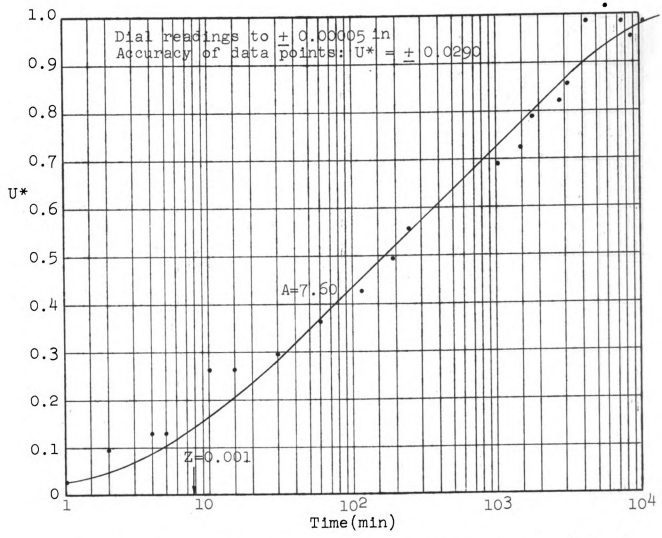

Figure A.38. Creep Curves for D-C-9-2; D=0.27-0.47 kg/cm^2

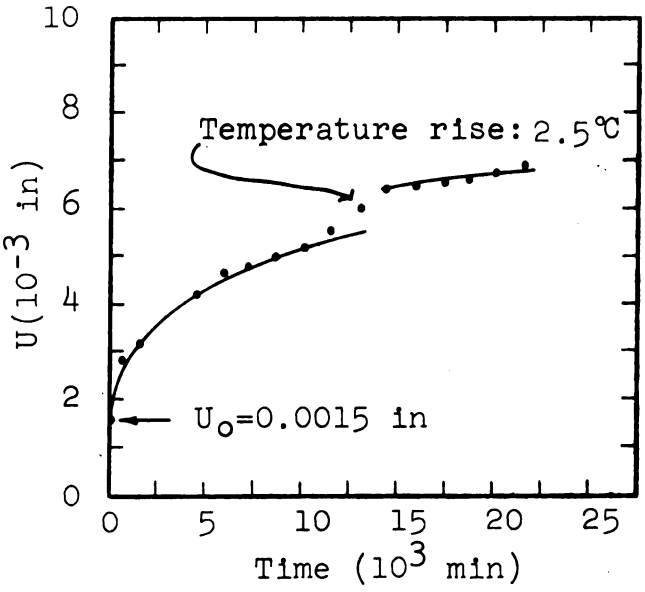

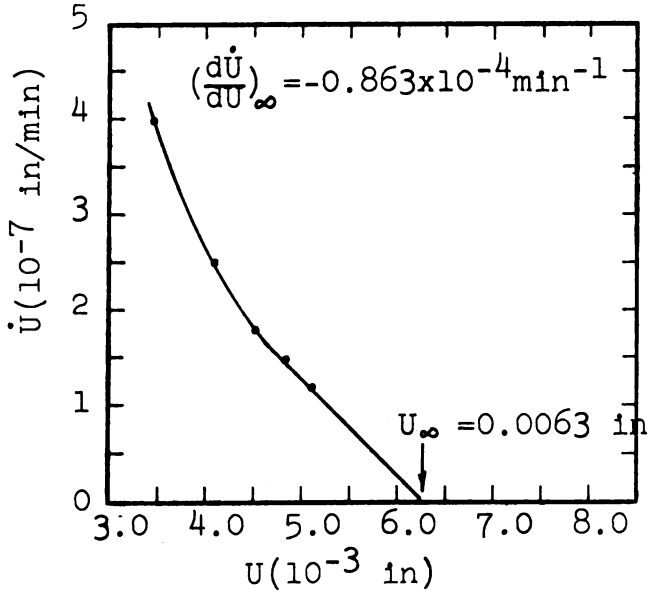

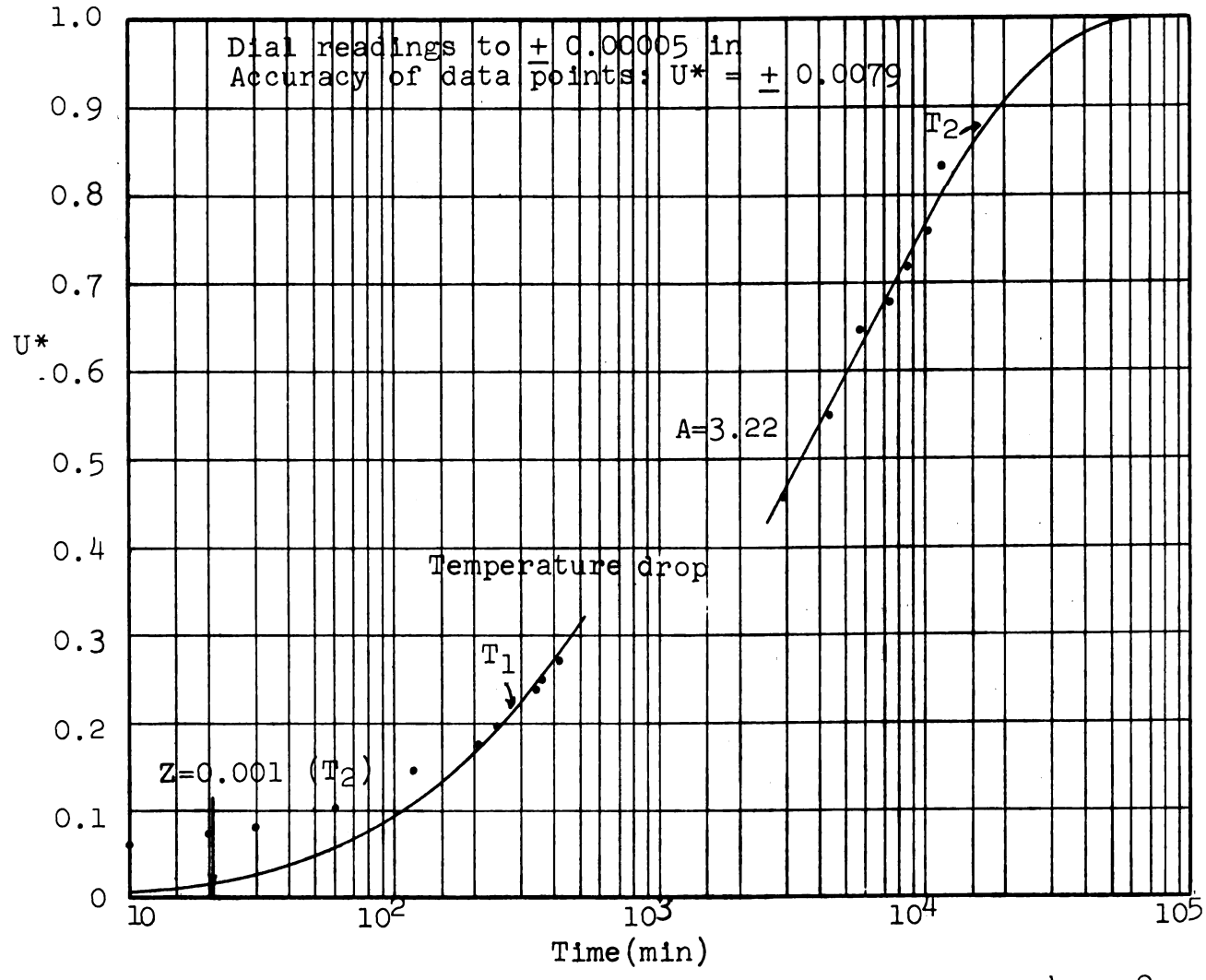

Figure A.39. Creep Curves for D-C-9-3; D=0.47-0.67 kg/cm^2

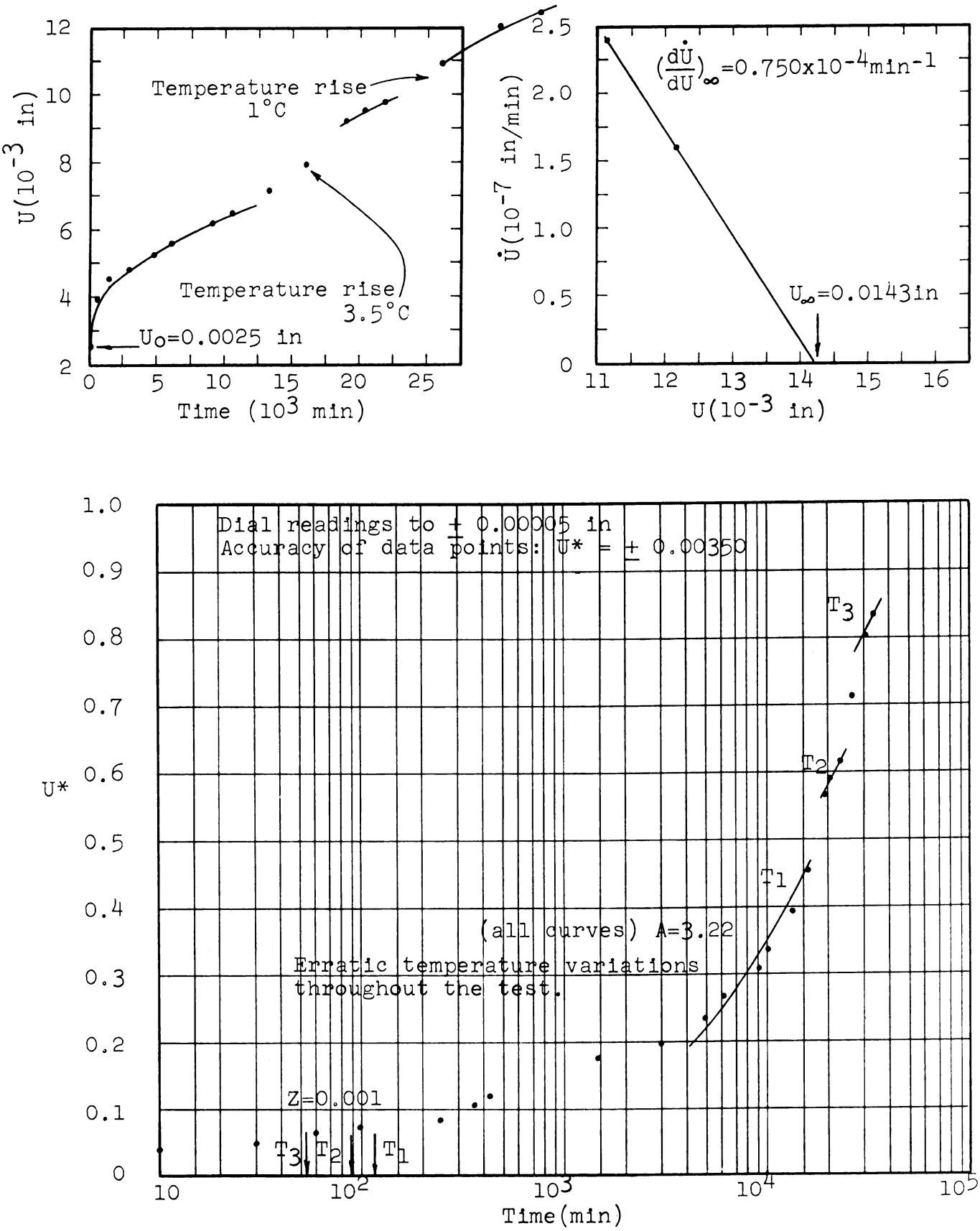

Figure A.40. Creep Curves for D-C-9-5; D=0.87-1.07 kg/cm^2

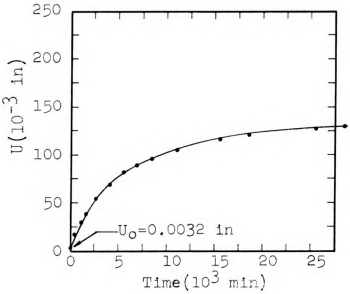

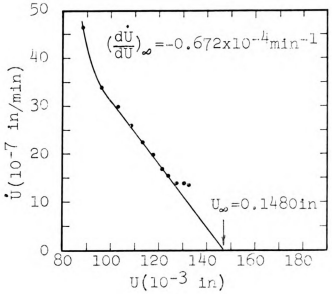

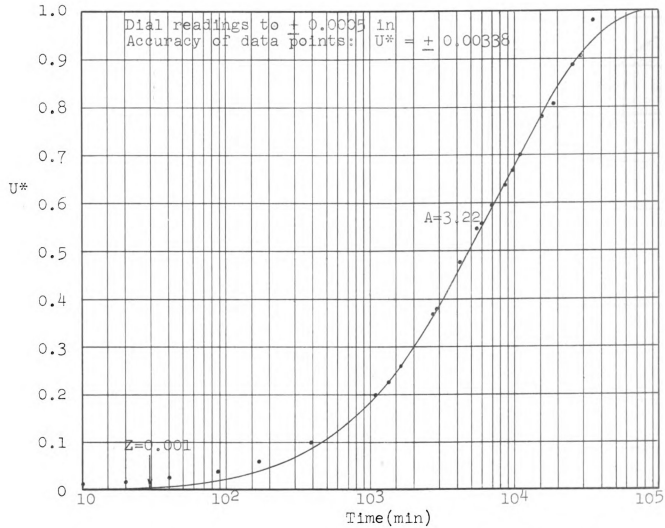

Figure A.41. Creep Curves for DP-C-1; D=0-0.0838 kg/cm^2

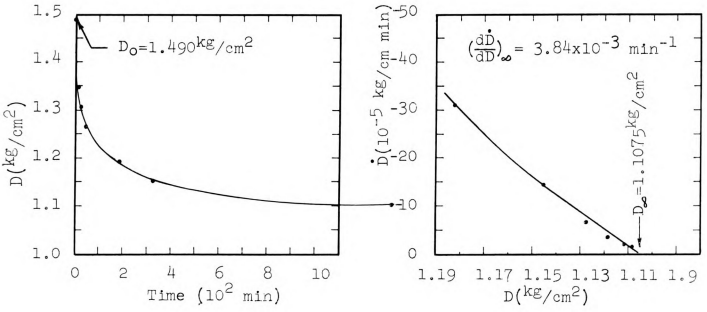

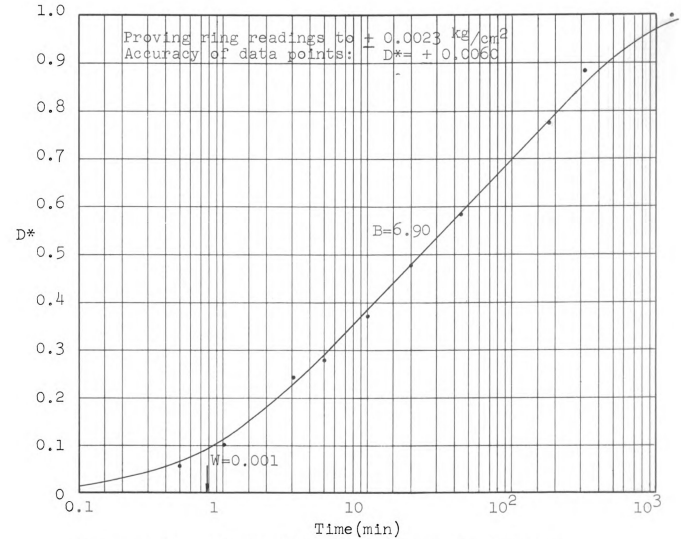

Figure A.42. Stress Relaxation Curves for F-R-5-1;
D = 1.490-1.1075 kg/cm²

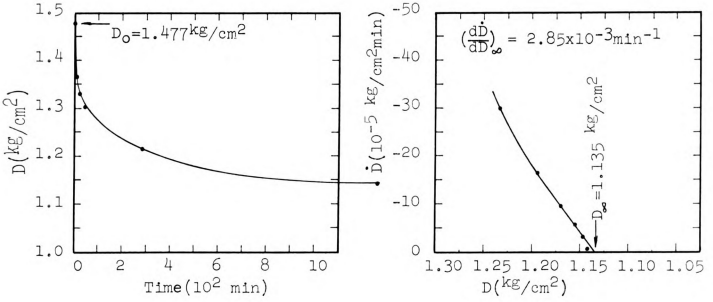

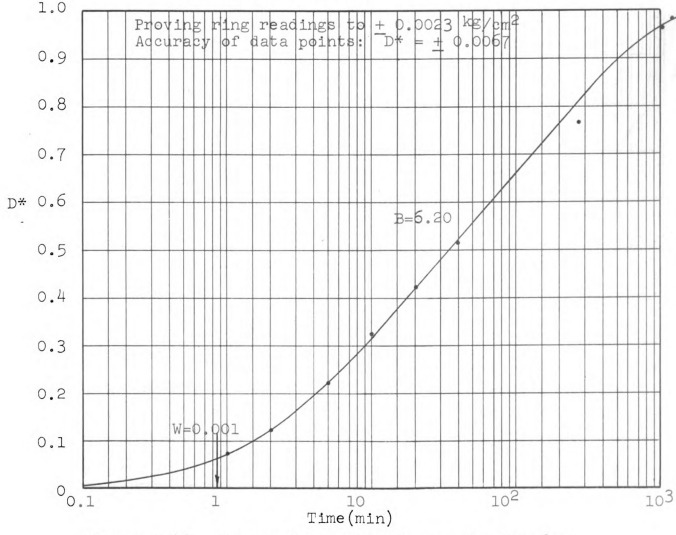

Figure A.43. Stress Relaxation Curves for F-R-6-1; D=1.477-1.135 kg/cm²

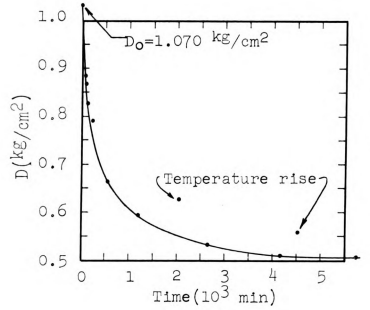

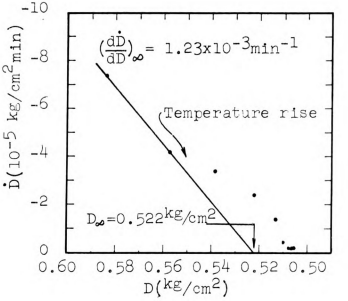

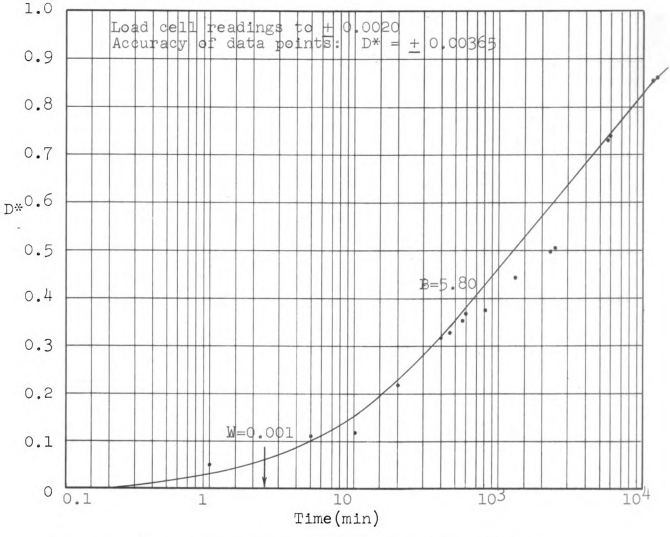

Figure A.44. Stress Relaxation Curves for F-R-8-1; D=1.070-0.522 kg/cm²

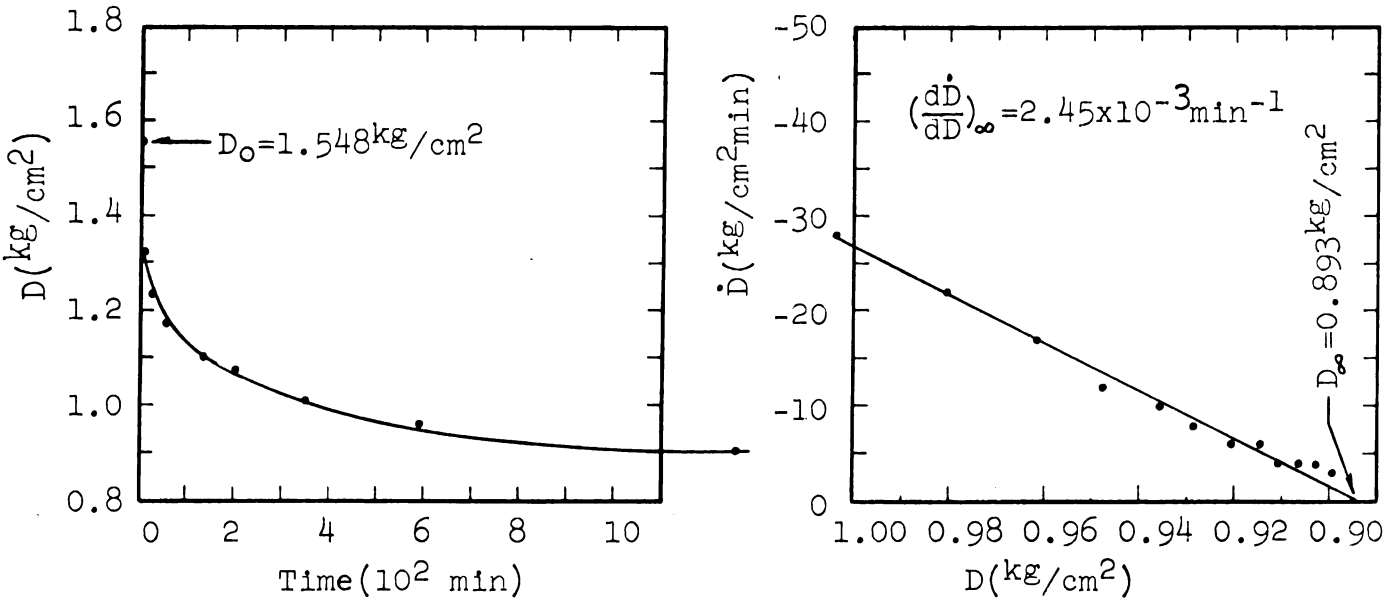

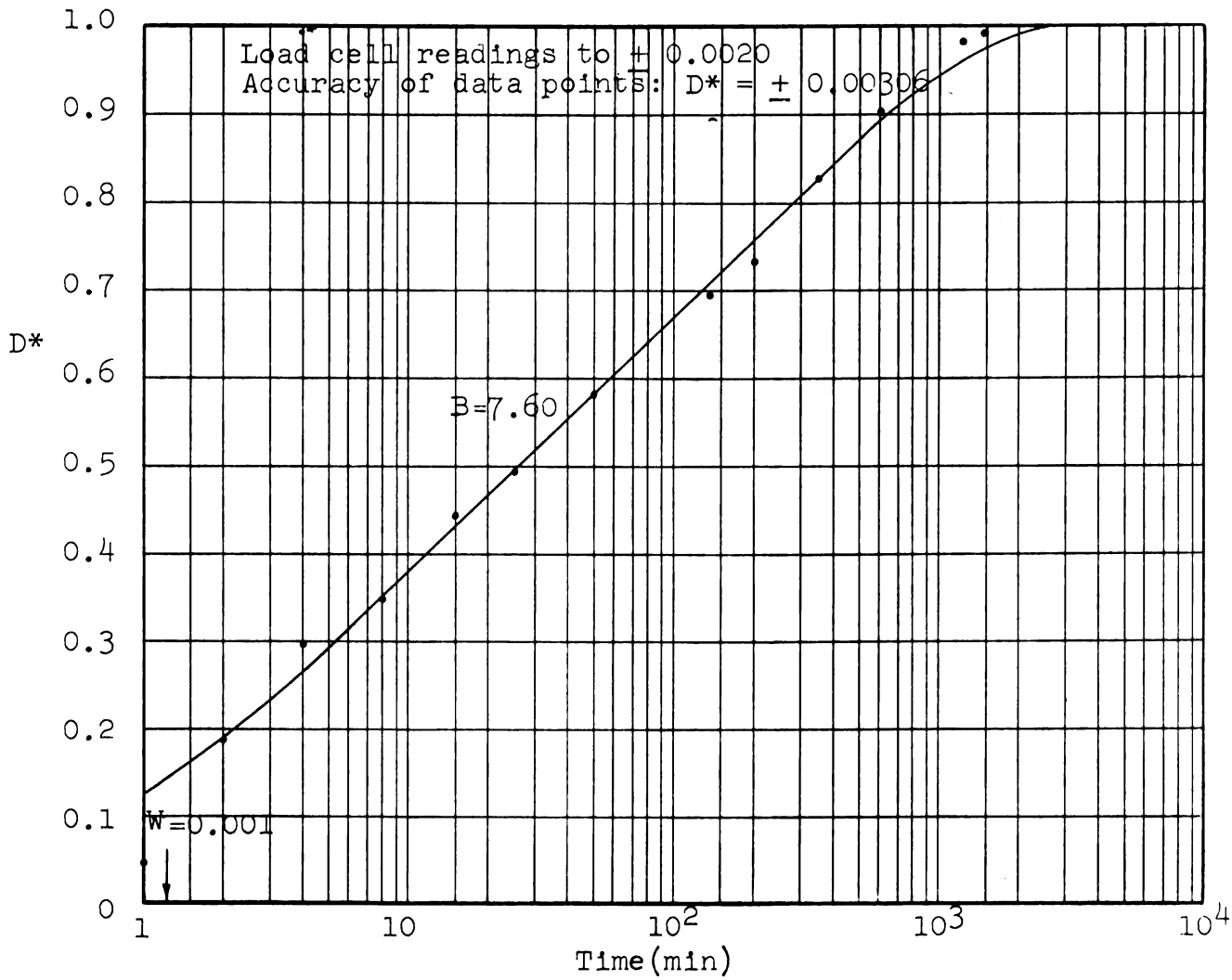

Figure A.45. Stress Relaxation Curves for F-R-8-2; D=1.548-0.893 kg/cm²

ROOM USE ONLY